UNIVERSITAT POLITÈCNICA DE CATALUNYA
BARCELONATECH
Escola d'Enginyeria de Telecomunicació
i Aeroespacial de Castelldefels

TREBALL DE FI DE GRAU

TFG TITLE: Specification, design and development of a solid rocket engine for suborbital sounding missions

DEGREE: Grau en Enginyeria de Sistemes Aeroespacials

AUTHOR: Aleix Coma Busquets

ADVISORS: Jordi Gutiérrez Cabello

DATE: December 6, 2020

Títol: Especificació, disseny i desenvolupament d'un motor de coet de combustible sòlid per a missions espacials suborbitals
Autor: Aleix Coma Busquets

Directors: Jordi Gutiérrez Cabello

Data: 6 de desembre de 2020

Resum

Aquest projecte consisteix en definir els requisits tècnics, dissenyar i desenvolupar un motor de coet de combustible sòlid. Aquest motor de coet és ideat per tal de fer una funció molt concreta: propulsar una càrrega útil de 0,3 kg de massa fins a una alçada de 100 km, en una trajectòria parabòlica tot fent un vol suborbital. Aquesta càrrega útil podria aprofitar les condicions úniques que ofereix un vol suborbital; especialment, un cert període de temps en microgravetat. El coet s'enlairaria des d'una plataforma situada a 30 km d'alçada, mitjançant un globus aerostàtic.

El motor hauria de complir 3 propietats principals: seguretat, cost i robustesa. Seguretat per a les persones encarregades dels processos de posada en marxa del motor: la construcció de l'estructura mecànica, el processament del propel·lent, la integració de totes les peces, el transport, etc. El cost de tots aquests processos ha de ser el més baix possible, per tal que sigui viable fer servir aquest sistema de llançament per part d'estudiants, universitats i centres de recerca que disposin de pocs recursos econòmics. A més a més, aquest motor ha de ser robust; és a dir, ha de funcionar correctament tant en condicions nominals com en condicions que siguin, fins a cert punt, desfavorables.

Com ja s'ha esmentat, el projecte està dividit en 3 parts: definició, disseny i desenvolupament. Els requisits tècnics es defineixen mitjançant un procés de recerca que té l'objectiu d'entendre el funcionament dels motors de coet de combustible sòlid. La part de disseny consisteix en trobar solucions tecnològiques als requisits, tot complint les 3 propietats que ja s'han mencionat. Finalment, a la part de desenvolupament, es posen a prova alguns elements crítics del motor, per tal de validar, o bé invalidar i millorar, el disseny que s'ha fet.

Title: Specification, design and development of a solid rocket engine for suborbital sounding missions

Author: Aleix Coma Busquets

Advisors: Jordi Gutiérrez Cabello

Date: December 6, 2020

Overview

This project consists in the definition of the technical requirements, the design and the development of a solid rocket engine. This rocket engine must fulfil a specific mission: to propel a 0.3 kg heavy payload to a height of 100 km, while following a parabolic trajectory, in a suborbital flight. The payload could make use of the very unique conditions experienced in a suborbital flight; namely, the microgravity conditions for a certain amount of time. The rocket would take-off from a launch platform lifted up to a height of 30 km, by means of an aerostatic balloon.

The engine must fulfil 3 main properties: safety, cost and robustness. It shall be safe, for anyone working on any of its associated processes: the manufacturing of its structure, the processing of the propellant, the integration of all elements, the transportation, etc. The cost of the engine shall be as low as possible, in order to pave the way for students, universities or research centres with low funds to use this launch system. Besides, the engine must be robust enough; that is, it must be able to work as expected at nominal conditions but also at slightly adverse conditions.

As has already been pointed out, the project is structured in 3 phases: definition, design and development. The first phase is based on research, and it must allow detailed acknowledgement on how a solid rocket engine works, thus allowing to define the technical requirements. The design phase consists on establishing technological solutions for the requirements, while fulfilling the 3 properties of the rocket engine that have already been mentioned. Finally, the development phase is about testing some critical elements of the engine, in order to validate, or either invalidate and thus improve, the design.

This work is dedicated to the memory of Ramon Casanova i Danés.
As well, to my former teachers at *Escola Casa Nostra* and *IES Pere Alsius i Torrent*.
Likewise, to my former partners at AEiG Pla de l'Estany for helping me grow in character.
Also to my parents, for conveying me the value of hard work and passion for knowledge.

Finally, to everyone today being politically prosecuted, jailed and exiled.
For defending political ideals and projects. For expressing ideas.
For thinking, speaking, writing and working for a different, perhaps better, state of things.

CONTENTS

Acknowledgements 1

CHAPTER 1. Introduction 1

1.1. Context 1

1.2. Thesis Structure 3

CHAPTER 2. Engine concept definition 4

2.1. Basic form factors 4

2.2. Solid propellants 4

2.2.1. Requirements 5

2.2.2. Potassium Nitrate based propellants 6

2.2.3. Ammonium Nitrate and Ammonium Perchlorate based propellants . . 8

2.2.4. Assessment 8

2.3. Model for the trajectory 8

2.4. Atmospheric model 10

2.5. Computing 12

2.6. Further engine definition 13

CHAPTER 3. Functional design 15

3.1. Engine model 15

3.1.1. Initial assumptions 15

3.1.2. Correction factors 15

3.1.3. Algorithm 16

3.2. Integrated model engine-trajectory 19

3.3. Functional requirements and design parameters 19

3.3.1. Defining functional requirements 20

3.3.2. Functional design parameters 21

3.4. Engine functional design 22

3.4.1. Basic grain functional configurations 22

3.4.2. Grain configuration constraints 25

3.4.3. Method . . . 25
3.4.4. Simulations . . . 27

CHAPTER 4. Thermo-structural design . . . 31

4.1. Structural model . . . 31
4.1.1. Assumptions . . . 31
4.1.2. In-flight loads . . . 32
4.1.3. Structural requirements . . . 32

4.2. Model of transient heat transfer . . . 33
4.2.1. Assumptions . . . 33
4.2.2. Initial conditions . . . 33
4.2.3. Mathematical model . . . 34
4.2.4. Discretization . . . 35

4.3. Case configurations . . . 35
4.3.1. Structural materials . . . 36
4.3.2. Thermal protection materials . . . 37

4.4. Coupled thermo-structural model . . . 38
4.4.1. Design parameters . . . 39
4.4.2. Algorithm . . . 39

4.5. Case design . . . 40
4.5.1. Method . . . 40
4.5.2. Simulations and results . . . 40

4.6. Considerations for the nozzle design . . . 43

4.7. Combined design and rocket performance . . . 44

CHAPTER 5. Experiment . . . 46

5.1. Introduction . . . 46
5.1.1. Context . . . 46
5.1.2. Objectives . . . 46

5.2. Experiment design . . . 46
5.2.1. Concept . . . 46
5.2.2. Components and requirements . . . 47
5.2.3. Assembly design . . . 48
5.2.4. Procedure . . . 48
5.2.5. Data analysis concept . . . 49

5.3. Preparation **49**
5.3.1. Assembly manufacturing 49
5.3.2. Specimens preparation 50

5.4. Results **51**
5.4.1. Execution 51
5.4.2. Data arrangement and preliminary analysis 51
5.4.3. Estimating the film coefficient 53
5.4.4. Analysing the results 53

CHAPTER 6. Mechanical prototype **55**

6.1. Mechanical design **55**
6.1.1. Fastening and sealing 55
6.1.2. Component tolerances 55

6.2. Manufacturing the components **56**

6.3. Assembling the pieces **56**

CHAPTER 7. Conclusions **59**

Bibliography **61**

APPENDIX A. Code **66**

A.1. Chapter 3: Ideal Rocket Trajectory.m **66**

A.2. Chapter 4: Thermo structural algorithm 1 layer.m **77**

APPENDIX B. Technical drawings **83**

B.1. Chapter 5: Experiment assembly **83**

B.2. Chapter 6: Mechanical prototype **88**

APPENDIX C. Manual of the experiment, plots and images **91**

LIST OF FIGURES

1.1 Schematic of both the aerostatic balloon (left) and the rocket (right). The rocket fairing is depicted in grey, while the engine is shown in light blue. The rocket would need to be attached to the balloon and supported by a launch platform, which is not depicted here. 2

2.1 Temperature profile up to a geometric height of 90 km, according to different models that rely on experimental and statistical data. Source: reference (11). 11
2.2 Pressure and density profile up to a geometric height of 1000 km, according to the model U.S. Standard Atmosphere, 1976. Source: reference (11). 12
2.3 Simulated flight profile (height vs time) with our algorithm for a $DeltaV = 1341 m/s$. It takes 118 s to achieve the apogee at 100 km. It takes 311 s to complete the trajectory and hit the ground. 13

3.1 Schematic drawing of the grain configuration that we have called *Option 1*. Its inhibited surfaces are depicted in red; its exposed surfaces are depicted in scrapped grey. 23
3.2 Schematic drawing of the grain configuration that we have called *Option 2*. . . . 23
3.3 Schematic drawing of the grain configuration that we have called *Option 3*. In red, the inhibited surfaces. In scrapped grey, the burning surfaces. Just 2 propellant segments are depicted here; however, any number of segments is possible as a design parameter within this configuration. 24
3.4 Schematic drawing of the grain configuration that we have called *Option 4*. . . . 24
3.5 Schematic drawing of the grain configuration that we have called *Option 5*. In red, the inhibited surfaces. In scrapped grey, the exposed surfaces. Any number of segments would be theoretically possible. 24
3.6 Schematic drawing of the grain configuration that we call *Option 6*. 24

4.1 Schematic of a thin cylinder under an internal stress, such is the case with our combustion chamber, and the subsequent stresses that it holds. Source: reference (24). . . . 31
4.2 Generic graphical representation of how a problem like transient heat transfer is approached with a numerical method of *Finite Differences*. Both time and a single space dimensional are converted into a mesh. A certain function (coloured surface) is then iteratively evaluated at each point of the mesh. Source: reference (31). 34
4.3 Decrease in the yield strength of AISI 1018 as a function of temperature. Plotted from a linear interpolation of the data presented in reference (27). 37
4.4 Decrease in the yield strength of Aluminium 6061-T6 as a function of temperature. Plotted from a linear interpolation of the data presented in reference (28). 38
4.5 Performance results for *Option 1*. At the right of the vertical, red, dashed line, there are the feasible structural configurations. The red, solid curves correspond to a burn time equal to 28 s, whilst the green, dashed curves correspond to a burn time of 17 s. Each one of the red, solid curves is associated with a case thickness equal to 1 mm, 1.5 mm and 2 mm, respectively, and the same for the green, dashed curves. 41
4.6 Performance results for *Option 2*. 41
4.7 Performance results for *Option 3*. 42

4.8 Performance results for *Option 4*. 42
4.9 Trajectory of the rocket for the previous engine design parameters. A dry mass equal to 1.5 kg has been assumed. 45

5.1 Draft of the experiment assembly. It includes both the torch, the specimen, the thermocouple and the vice for easier understanding. 48
5.2 Finished experiment assembly. All of the pieces and components, including the torch and the thermocouple, can be appreciated. 50
5.3 Temperature-time plots of specimen configuration number 1 obtained from the raw data; the *step data points* can be appreciated. 52
5.4 Dependency of the ablator thickness on the final temperature achieved by the plate. 54

6.1 Standardized types of fits and associated tolerances. Source: reference (47 . . 56
6.2 The three main engine components just before the assembly. The O-Rings and screws can be appreciated. 57
6.3 The nozzle in the lathe chuck, prior to adjusting its diameter. 57
6.4 Final look of the rocket engine *Casanova* prototype. 58
6.5 SolidWorks model of the completed *Casanova* rocket. Source of the background: NASA. 58

C.1 Results for the testing of the five specimens of configuration n^{o}1. In the vertical axis, temperature at the rear of the plate in $^\circ$C. In the horizontal axis, the n^o of data point, separated one second from each other. 92
C.2 Results for the testing of the five specimens of configuration n^{o}2. 92
C.3 Results for the testing of the five specimens of configuration n^{o}3. 93
C.4 Results for the testing of the five specimens of configuration n^{o}4. 93
C.5 Preparation of the specimens. 94
C.6 Highest temperature registered by the thermographic camera, with the last specimen of configuration 4. 94
C.7 Succession of three images of the thermographic camera for the same specimen, showing the rise in temperature. 95

LIST OF TABLES

3.1 List of the preliminary engine functional configurations based on *Option 5*, named with their correspondent notation. L_c, d_c, d_t, d_o, L_g, d_{eg} and d_{pg} are the casing inner length, casing inner diameter, grain segment length, grain segment external diameter, grain segment port diameter, nozzle throat diameter and nozzle outlet diameter, respectively. 26
3.2 List of the preliminary engine functional configurations based on *Option 6*. . . . 26
3.3 Performance results of Step 0.1 for the preliminary engine functional configurations based on *Option 5*. 27
3.4 Results of step 0.1 for the preliminary engine functional configurations based on *Option 6*. 27
3.5 Results of Step 1.1 for the engine functional configurations based on *Option 5*. . 28
3.6 Results of Step 1.1 for the preliminary engine functional configurations based on *Option 6*. 28
3.7 Results of Step 3.1. This time we not only compute the engine performance, but also the rocket trajectory. a_m, h_m, I_t and I_{sp} stand for the maximum acceleration, height, total impulse and specific impulse, respectively. 29
3.8 Potential engine functional configurations with a greater number of segments. As we increase this magnitude, the maximum acceleration increases, until being higher than 150 m/s^2. 29
3.9 Final table of all the engine functional configurations that fulfil the functional requirements and, therefore, are feasible. 30

4.1 Mechanical and thermal properties of AISI 1018 steel alloy at room temperature. ρ, E, σ_y, ν and $\%EL$ are the material density, modulus of elasticity, yield strength, Poisson ratio and ductility, expressed in percent elongation, respectively. α and λ_L are the thermal properties; the diffusivity and the coefficient of linear expansion at room temperature. Source: reference (38). 36
4.2 Mechanical and thermal properties of aluminium alloy 6061-T6 at room temperature. Source: reference (28). 37
4.3 Thermal properties of both candidates to ablative coating for our engine. κ, $\bar{c}$, ρ and α are the thermal conductivity, specific heat, density and diffusivity, respectively. Source: reference (42). 38
4.4 t_c is the thickness of the case. t_a^{17} and t_a^{28} are ablator thicknesses for a burn time of 17s and 28s, respectively. ζ_{min}^{17} and ζ_{min}^{28} are the minimum safety margin for a burn time of 17s and 28s, respectively. $T^{17}c_{max}$ and $T^{28}c_{max}$ are the maximum average temperatures achieved by the case for a burn time of 17s and 28s, respectively. 43
4.5 L_c and d_c are the case internal length and diameter, respectively. dt and d_o are the nozzle throat and outer diameters, respectively. L_g, d_{eg} and d_{pg} are, in this order, the propellant grain length, external diameter and port diameter. Finally, t_c and t_a are the thickness of the case and the ablative insulator, respectively. . 44

4.6 F_{av} is the, approximate, mean thrust developed by the engine. P_0 and P_2 are the pressure at the combustion chamber and at outlet of the nozzle, respectively. I_{sp} and It are, in this order, the specific impulse and the total impulse. Finally, ζ_{min} is the minimum structural safety margin. 44

5.1 Final temperature of all the specimens after the test. 53
5.2 Thickness of the ablative material for each of the final specimens. Note that two of the specimens have not been measured. 54

6.1 Measured masses of the prototype pieces. 57

ACKNOWLEDGEMENTS

I wish to express special thanks and gratitude to the professor Ana Lacasta for providing me access into her laboratory and offering me technical and scientific assistance as needed. Without her help, this document would have been significantly shorter in content. I would like to extend my gratitude to my advisor, professor Jordi Gutiérrez, for his guidance, support and encouragement in the different phases of the project and in its completion. As well, I am extremely thankful to Jaume de Palol for his unconditional guidance and dedication despite having a busy schedule at work.

I am very thankful to Carles Planas and the workers at PLACON SRL *as this work would not have been completed without their complicity. As well, I owe my gratitude to the workers at* Inbrooll Industries SL *and* Criver Metàl·liques Industrials SL.

Finally, to my family and colleagues, for their constant supportive attitude and constructive suggestions.

CHAPTER 1. INTRODUCTION

1.1. Context

Rockets are the only practical means that has been devised and developed to get to outer space. Access to space has allowed us to attain huge scientific discoveries that enables us to better know the cosmos, that is, understanding this world in its broadest sense: as the sum of not only what lies in outer space, but also the Earth, its living beings and ourselves, humans.

Interplanetary and orbital space missions have brought the greater part of those discoveries, which could have never been done from the Earth's surface. However, sub-orbital spaceflight has also enabled to do important research in many scientific fields. These include the fields of micro-gravity research, Earth sciences and cartography, the study of the Earth's upper atmosphere and Astrophysics. However, it is a well-known fact that rocket science and engineering is hard. It takes a lot of time, resources and labour force to develop any kind of space rocket launch system, even sub-orbital ones. As such, nowadays, access to space is still reduced and expensive.

We have devised a sub-orbital launch system dedicated to very small payloads, that could be built as part of research and educational projects. This launch system would take payloads to outer space in a suborbital trajectory, to be followed by a short period of weightlessness and a safe return to the surface of the Earth. The potential customers for this launch system would be both research centres, education centres and individuals.

The launch system would be made up of three main elements: the rocket, the launch platform and the balloon. The rocket would have a single stage and would be propelled by a solid-propellant engine; it would carry the payload inside a fairing. The launch platform would be the element giving stability to the rocket during the launch. The balloon would be attached to both the platform and the rocket and would lift both elements to a high altitude. The rocket would be ignited once a certain height was achieved, and it would then perform the suborbital flight. During the fall, a parachute would be deployed for recovery. This space launch approach is called a *Rockoon* system, this word being a portmanteau of *rocket* and *balloon*.

The mission level requirements for the proposed *rockoon* are the following:

MIS-01: The rocket must have the lowest possible total take-off mass.

MIS-02: The rocket shall be able to carry a payload of 300 g.

MIS-03: The internal volume of the fairing must be dimensioned so that a CanSat can properly fit inside it.

MIS-04: The launch of the rocket shall happen at a height equal or greater than 30 km.

MIS-05: The rocket shall achieve the apogee at a height equal or greater than 100 km and it shall provide a state of microgravity to the payload for at least four minutes.

MIS-06: Whether the customer demands it, the fairing shall be able to eject the payload once the apogee is reached.

MIS-07: The rocket shall deploy an appropriate parachute at an appropriate height to ensure a safe fall and touch-down.

MIS-08: Once on the ground, it shall be possible to recover the rocket in a reliable and efficient way.

MIS-09: The machining, assembling, testing and operation processes of the launch system shall be safe for everyone involved.

MIS-10: The use of this launch system shall be open to any customer.

MIS-11: It shall be as cheap, reliable and robust as possible.

The balloon would be made out of a fabric from a polymeric material; this fabric containing a lighter-than-air gas (such as helium or hydrogen), thus providing buoyancy to lift the whole launch system to the required height. The launch platform would consist on all structural and electronic components in charge of holding the rocket during the ascent to the targeted launch height, and, after that, to ensure a successful lift off. To completely define, design and develop this launch platform would already be a lot of work; however, we won't tackle this part of the launch system in this document.

Meanwhile, the rocket would also be made out of two main parts: the fairing and the engine. The fairing would be the combination of the structural elements protecting the customer's payload during the flight, plus the avionics and the recovery system ensuring a successful flight, data acquisition and recovery. The fairing would also have to integrate all the mechanical and electronic elements devoted to ejecting the payload, as mentioned in the requirements. The engine would be the propulsive unit powering the rocket. In this document, we will focus on the engine component.

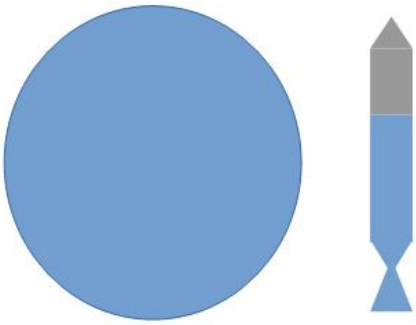

Figure 1.1: Schematic of both the aerostatic balloon (left) and the rocket (right). The rocket fairing is depicted in grey, while the engine is shown in light blue. The rocket would need to be attached to the balloon and supported by a launch platform, which is not depicted here.

The objective of this Bachelor Thesis is then to define, design and develop the rocket engine that would power the envisioned suborbital launch system. According to this approach, the definition consists on specifying the requirements and constraints that the engine must met and stating the main components that it will be made of. The design consists on finding technological solutions to that said requirements and constraints and describing in detail all of its components. Finally, the development consists on validating the theoretical design through tests and experiments, redefining the design whenever necessary, in an iterative way. Development finishes when it is achieved a state of design maturity and technology readiness that allows the beginning of the system's operation as expected. Each of these three phases are a stepping stone towards the next one.

The rocket will be called *Casanova*, as to the Catalan inventor Ramon Casanova i Danés who, in 1917, with scarce resources, developed and patented an advanced pulse jet engine for airplanes

We will characterise the performance of the engine through several *figures of merit*. The thrust is the force, generated by the expelled exhaust gases, that changes the momentum of the rocket. The total impulse can be thought as a measure of the power of the engine, being proportional to both the average value of thrust and the duration of the burn (*burn time*). The specific impulse, I_{sp}, can we thought as a measure of the engine's efficiency, being proportional to the provided total impulse and inversely proportional to the mass of fuel burned.

1.2. Thesis Structure

This document is organised as follows:

In Chapter 2 we make a basic design of the engine starting from scratch. We define the main components of the engine and we establish the basic requirements and constraints that they must fulfil. In order to do that, we design and implement an algorithm that computes the theoretical trajectory of the rocket according to several design parameters. We end up with a set of requirements and constraints that the engine must fulfil.

Chapter 3 represents the foundations for all the subsequent work. We define the basic (functional) design parameters of the engine and we develop an algorithm –that is, a set of steps– that computes the performance of the engine as a function of the design parameters. We implement such algorithm into a computer program to obtain a range of engine design possibilities that fulfil the functional requirements.

In Chapter 4, we address the problems of structural integrity and thermal protection of the engine, which are in fact interrelated. Again, we define a model, develop it into an algorithm and implement it into a computer program. We identify the design parameters and, by using the program, we derive the best solution.

In Chapter 5 we design an experiment that allows us to start the development process by comparatively validating a vital part of our engine design. We define the specific objectives, materials, setup, processes and operation of the experiment. We make technical drawings of the setup components, and we manufacture and assemble them. We execute the experiment and analyse the results.

In Chapter 6 we design and manufacture a prototype of the rocket engine, addressing in the meantime the technological problems of fastening, sealing and the compatibility of the pieces. Detailed drawings and 3D models are made for making the manufacturing of the prototype possible.

Finally, in Chapter 7 we collect all the work that has been done and we state the work that should be done in the future in order to properly develop and completely validate the proposed launch system.

CHAPTER 2. ENGINE CONCEPT DEFINITION

2.1. Basic form factors

The engine chosen for our rocket will use solid propellant for producing the necessary energy for propulsion; the reason being that both liquid and hybrid rocket engines are much more complex and costly to design and develop, requiring specific and heavy turbo machinery, complex piping and a flow control system.

Our solid propellant based engine will be composed of two main functional parts: the combustion chamber or case and the nozzle. The combustion chamber is the container holding the solid propellant during the ascent. After ignition, the propellant would start to be burned and turn into a hot mix of exhaust gaseous products, filling the free volume of the chamber and escaping, at a certain mass flow rate, through the nozzle. The gases inside the chamber will, ideally, achieve an stationary state of temperature and pressure. The nozzle would turn a fraction of the thermal energy from the exhaust products flowing through it into kinetic energy by expelling them at a high speed, thus providing thrust.

The combustion chamber could have many shapes. An spherical combustion chamber would optimise the available volume to the propellant per structural surface unit; thus, the weight would be minimised. However, the machining process of such an spherical shape with a constant thickness would be complex and expensive. Besides, were we using a single spherical chamber, the rocket engine would end up having an extremely large cross-section. On the other hand, a cylindrical chamber could enclose the equivalent propellant amount while not needing any additional outer structure, acting itself as the fuselage of the rocket. Thus, all things considered, this solution would end up saving weight; it would also be a cheaper and simpler shape configuration.

The shape of the nozzle is dictated by the need to accelerate the exhaust products up to a supersonic velocity; thus it would need to have a convergent-divergent profile. It is left to decide whether it would have either a De Laval or rather a conical form factor. De Laval –or bell-shaped– nozzles can be designed and developed to be shorter, lighter and more efficient than conical ones (1). However, a conical form factor is comparatively way cheaper and easier to manufacture than its more efficient counterpart, which is a critical requirement in our project. Therefore, we end up choosing to stick with a conical nozzle design.

2.2. Solid propellants

Many solid propellants have been developed and successfully used over the years for both amateur, commercial, governmental and military purposes on many missiles and solid rocket boosters.

2.2.1. Requirements

Many characteristics of the solid propellants can be pointed out to assess the different options. Our propellant must achieve a reasonable trade-off out of all of them.

- Safety: The largest hazard that a solid propellant poses is the sensitivity for ignition at the work environment during its processing. It would be complex to analyse how that could happen; however, inadvertent ignition could be caused by either excessive heating, friction, static charges, impacts, or inappropriate vibration. For a certain propellant, a temperature of auto-ignition can be established.

- Knowledge: Experimentation and characterisation upon rocket propellants is not our purpose in this project; rather, we prefer to use an already well-known propellant formulation. It should have already been well-characterised (formulation and burn-rate characteristics should be known), developed, processed and experimentally tested with success. The full information from the formulation, characterisation, all of the processing steps, tests and/or flights data, should be readily available and free to obtain through bibliography or the web.

- Simplicity of the processing and manufacturing of the propellant grains

- Cost and availability: The ingredients should be available, ideally, in local stores where direct contact can be established. All of the relevant information on these ingredients should be readily available to us upon acquiring them. The economic costs of buying the ingredients should be as low as possible.

- Burning characteristics and performance: Different propellants will present different burning characteristics; that is, the combustion of the grains will happen at different rates. This is of extreme importance in order to control the steady combustion chamber pressure, which will be one of the main design parameters. The burning characteristics of many propellants can be approximated, according to experimental results, by a power law, characterised by two non-dimensional magnitudes: the burn rate coefficient, a, and the burn rate exponent, n. In those cases, the burn rate of the propellant grains can be approximated by the following expression:

  $$r = a\,P_0^n \tag{2.1}$$

  where P_0 is the pressure in the combustion chamber and r is the burn rate.

  Burn rate exponents should have a value between 0.2 and 0.8. With a value below 0.2, the propellant could self-extinguish due to insufficient chamber pressure buildup, while at values larger than 0.8, the combustion would be unpredictable and uncontrollable. Higher specific impulses are desirable as it implies that a lesser amount of propellant will be needed for achieving the requirement MIS-05. A high temperature of the exhaust gases is often related to greater performance and efficiency of the propellant. However, it is undesirable from an structural design point of view, as we will explore later in this document.

- Predictability and reproducibility: Predictability stands for our ability to predict how the propellant will behave in a certain set of design conditions and inputs. The higher the predictability, the lower the risks, uncertainties and costs of the development

of the engine will be; it depends on both our knowledge of the propellant and the accuracy of our models with respect to reality. Reproducibility stands for our capacity to obtain the same results on successive experiments or tests that replicate the same inputs and conditions; it decreases with increasing complexity of the propellant processing method and increases when more expertise, care and better equipment are employed.

- Mechanical properties: The density of the propellant will have a large impact on the size of the chamber and the structural weight of the engine; as they will experience stresses during the flight, their elastic modulus, yield strength and ductility must also be considered.

Black Powder was one of the first propellants to be used for propelling rockets; in fact, it it the oldest explosive chemical mixture to be known. It is a mixture of Potassium Nitrate, Charcoal and Sulphur. It is highly sensitive to ignition by either friction, prolonged heat, shock and sparks, even at ambient pressure (2). Its performance is really low; it has an specific impulse well below 100 s.

We must look into more appropriate options. In the aerospace industry, Ammonium Perchlorate and Ammonium Nitrate are the most widely used oxidisers. However, in the world of amateur rocketry, there is a whole family of propellants based on Potassium Nitrate (KNO_3), which are denominated *Rocket Candy*.

2.2.2. Potassium Nitrate based propellants

Potassium nitrate is a compound that can be combined with many substances to produce feasible propellants, with a high enough burn rate exponent, a reduced cost and a relatively low performance.

2.2.2.1. Sucrose

A mixture of potassium nitrate (KNO_3), as the oxidizer, and sucrose ($C_{12}H_{22}O_{11}$), which acts as a fuel and binder, has been used successfully for years by amateur rocket experimenters (3). This mixture is called *KNSU*. During the procedure of processing, a mixture of the ingredients must be heated; however, the risk of inadvertent ignition is not high, as the auto-ignition temperature –that is, the temperature above which the propellant ignites and burns in a self-sustaining manner– is significantly higher than the maximum temperature that it achieves during processing. The exhaust products contain some toxic and corrosive gases, such as Carbon Monoxide (CO) and Potassium Hydroxide (KOH), as well as a certain amount of liquid droplets of Potassium Carbonate (K_2CO_3), which reduce the performance.

KNSU has a theoretical specific impulse up to 130 s and a low burn rate, having an exponent n with a value around 0.3. Its combustion temperature is around 1700 K, relatively low as compared to most solid propellants used in the aerospace industry. The solid grains are brittle but also reasonably strong. As well, the grain behaves hygroscopically, which means that it absorbs moisture from the air, reducing its ignitability and performance. The cost of the ingredients for KNSU is relatively low.

2.2.2.2. Sorbitol

KNSB is the name given to a solid propellant formulation made from a mixture of potassium nitrate and sorbitol ($C_6H_{14}O_6$). Just as with KNSU, the risk of inadvertent ignition is relatively low and, in fact, KNSB has shown some problems of ignitability, as it seems to need an extremely high amount of heat transfer in order to begin the combustion (4). Moreover, the chamber pressure profiles obtained on some static burning tests behave differently than expected, having a slow process of pressure rise inside the chamber, to be followed by an equally slow decay. As KNSU, it also produces toxic, hazardous gases as exhaust products, and liquid droplets of potassium carbonate.

Its ideal, theoretical specific impulse is higher than that of KNSU propellant; however, for all we know, it has only achieved a maximum value of 125 s in static tests at sea level conditions. It has a burn rate exponent around 0.23, and a combustion temperature equal to 1600 K. Its elastic modulus, E, has a value of 5.84 GPa, and its ultimate tensile strength, σ_{TS}, is about 7.2 MPa. As KNSU, it is also brittle, hygroscopic and has a relatively low cost.

2.2.2.3. Dextrose

Another propellant is made from a mixture of potassium nitrate with dextrose ($C_6H_{12}O_6$) and it is called *KNDX*. Again, the risk of inadvertent ignition is relatively low, the exhaust products contain toxic gases, there is a certain amount of non-gaseous phase exhaust products. It has shown reproducibility in many static tests (5).

Its ideal specific impulse is around 164 s. However, it has only been measured at sea level conditions at a maximum value of 137 s. KNDX does not present a power law burn rate behaviour, but rather a complex curves that can be approximated by a set of power laws within successive intervals (6). It has a theoretical combustion temperature of 1710 K. Its mechanical properties are similar to those of KNSU and KNSB. It also has a similar hygroscopic behaviour. The ingredients are ~~cost~~ affordable and readily available.

2.2.2.4. Epoxy

RNX is a propellant made from potassium nitrate and epoxy resin, as a fuel and binder. Taking advantage of the great mechanical properties of epoxy, RNX possesses many particularities that make it an interesting choice. A certain amount of iron oxide (Fe_2O_3) must be added to the mixture to increase the burn rate. RNX does not require heating the mixture during any step of the processing (7). Therefore, it is significantly safer to handle and work with than any other potassium nitrate based propellant. Quoting R.Nakka, the rocket propellant experimentalist who has effectively developed RNX, it is ”one of the safest-to-produce, safest-to-handle and safest-to-use rocket propellants available”. As it is obvious, care must still be taken with hazardous exhaust products such as carbon monoxide (CO).

The delivered specific impulse at sea level conditions is typically lower than that of the previously propellants, with a value around 110 s. Its burn rate profile follows a power law and it can achieve a moderate burn rate exponent of at least 0.5. It has a combustion temperature that can get as low as 1500 K in some formulations. It has good mechanical properties: the solid grains are rigid and brittle, with an ultimate tensile strength of 19 MPa. It doesn’t have a hygroscopic behaviour, so it does not absorb moisture from the air. The

cost is slightly higher than that of KNSU, KNSB and KNDX.

2.2.3. Ammonium Nitrate and Ammonium Perchlorate based propellants

Ammonium nitrate is relatively inexpensive. As its melting temperature is much lower than that of potassium nitrate, it can't use sugars such as sucrose or dextrose as fuel. In this case, light metals, such as aluminium and magnesium, could be used in powdered form as fuel instead. A binder would be needed; HTPB (Hydroxyl-Terminated PolyButadiene) is of common use in the aerospace industry. However, much cheaper polymeric resins such as epoxy and polyester could also be used.

Theoretical estimations and experiments from rocket experimentalists assure that specific impulses greater than 200 s are possible (8), (9). However, its theoretical combustion temperature is much higher (more than 3000 K) than that of Sugar propellants (approximately 1500 K). Ammonium nitrate is slightly more dangerous than potassium nitrate, as it is slightly more prone to inadvertent ignition under certain conditions. As well, the processing of the propellant would be more complex than for the sugar propellants.

Ammonium perchlorate is a widely used oxidizer for solid propellant rockets (10). Its formulations often use aluminium powder and a binder such as, for example, HTPB. It can achieve, in the industry, specific impulses much higher than 200 s. Its combustion temperature achieves values similar to those of ammonium nitrate based formulations.

2.2.4. Assessment

Both ammonium nitrate and ammonium perchlorate based propellants are more expensive, more complex and higher performance alternatives to potassium nitrate based propellants. Nevertheless, sugar propellants are, overall, more desirable for our engine.

Within sugar propellants, both KNSU, KNSB and KNDX are very similar, while RNX, stands out as an alternative, due to the additional safety and simplicity of its processing and operation. KNDX however, has a specific impulse just slightly better than both KNSU and KNSB. Therefore, we conclude that the two propellant options that best fit our needs are both KNDX and RNX. Right now, we still can not choose one over the other.

The propellant will be processed into a solid shape called *propellant grain*. Some surfaces of this solid grain can be prevented from igniting by spreading and sticking a layer of non-burning, low-heat conductive material upon the required surface that is called an *inhibitor*.

2.3. Model for the trajectory

In this section, we establish the basic mathematical expressions, scientific principles and assumptions of a model that must allow us to compute the theoretical trajectory of our rocket according to the value of its design parameters.

The capability of a rocket engine to propel a rocket with a certain dry mass is characterised by a figure of merit called Delta-V, ΔV. According to Tsiolkovsky's rocket equation, if we

consider a chemical rocket that uses a solid propellant with a certain specific impulse, I_{sp}, its ΔV will depend mostly on the value of the mass ratio. The mass ratio is simply the initial total mass of the rocket –the dry mass plus the propellant mass– divided to the dry mass of the rocket.

$$\Delta V = V_e \ln\left(\frac{m_0}{m_1}\right) = I_{\mathrm{sp}}\, g_0 \ln\left(\frac{m_0}{m_1}\right) \tag{2.2}$$

being V_e the effective exhaust velocity of the combustion process, m_0 the mass of the propellant plus dry mass of the rocket, m_1 the dry mass of the rocket, I_{sp} the specific impulse of the propellant and g_0 the gravitational acceleration at the surface of the Earth

Now, we consider an object, a particle, with a certain mass, m_0. This object is launched upwards from a certain initial height, h_0, with an initial velocity $V_0 = \Delta V$. For further simplification, we will assume that this object acquires all of its velocity instantaneously. We neglect the effect of the atmospheric drag. Finally, we will consider that this object will only move vertically, without any lateral component. Newton's law of universal gravitation and basic Kinematics expressions allow us to obtain the one-dimensional trajectory equation of the object.

$$F_{\mathrm{g}} = -G\frac{m_0 M}{(R+h_0)^2} \tag{2.3}$$

being F_g the gravitational force, G the universal gravitational constant [$\mathrm{m}^3/(\mathrm{kg\,s}^2)$], M the mass of the Earth and R its radius.

$$a = \frac{dv}{dt} = \frac{d^2x}{dt^2} \tag{2.4}$$

being a, v, x and t the instantaneous, one-dimensional acceleration, velocity, displacement and time, respectively.

$$h(t) = h_0 + \Delta V\, t + \frac{F_g}{2m_0}\, t^2 \tag{2.5}$$

being $h(t)$ the instantaneous height of the rocket as a function of elapsed time since ignition.

We can obtain a more accurate model if we account for the atmospheric drag on the particle. A simplified case is that in which drag has a quadratic dependence with velocity.

$$h(t) = h_0 + \Delta V\, t + \frac{F_g - b(\rho, A, C_d)\, v^2}{2m_0}\, t^2 \tag{2.6}$$

$$v(t) = \Delta V + \frac{F_g - b(\rho, A, C_d)\, v^2}{m_0}\, t \tag{2.7}$$

$$b(\rho, A, C_d) = \frac{1}{2}\,\rho\, A\, C_d \tag{2.8}$$

being b a coefficient that is a function of many variables, ρ the air density, A the cross-sectional reference area of the subject and C_d the drag coefficient.

Unfortunately, this equation does not have an analytical solution. The reason is that there are several variables, mainly ρ and v, that will be constantly changing along the trajectory. Therefore, we will have to compute the trajectory by using a numerical algorithm.

If we consider that atmospheric air is an ideal, dry and homogeneous gas, ρ will only depend on temperature and pressure.

$$\rho = \frac{PM}{R^* T} \tag{2.9}$$

being P the total pressure of the air, M the mean molecular weight of the atmosphere, R^* the universal gas constant and T the total temperature of the air.

Now we can already design an algorithm for numerically computing the one-dimensional trajectory of the object, according to (2.6).

Step 0.1: Set the design parameters. ΔV, m_0 and h_0 are some parameters that will have a great influence. C_d is considered to be equal to 0.4 [reference R.Nakka]. Also, set simulation parameters, such as the size of the time steps, Δt. Initial time, t_0, is set at a value of 0.

Step 0.2: Compute the initial air pressure, temperature and density with the atmospheric model, at the initial height and conditions.

Step 1.1: Update the velocity of the object with (2.7). Update the height of the object with (2.6).

Step 1.2: Update the air pressure, temperature and density for the new height with the atmospheric model.

Step 2: Repeat steps 1.1 and 1.2 successively, until the object completes the trajectory and hits the ground. At each step, the atmospheric properties of the previous step are taken.

Now, we can easily implement the previous algorithm into a computer program. We will use the Matlab environment.

2.4. Atmospheric model

Our algorithm requires an appropriate mathematical atmospheric model to compute both the atmospheric pressure and temperature as a function of height. For this model to be considered appropriate, it should fulfil 3 conditions. For one, it should be up to date with current scientific knowledge and thus accurate with respect to reality. On the other hand, the model should have to work well in our interval of interest: from a height of 30 km to more than 100 km. Finally, it should describe the changes in pressure and temperature through simple mathematical expressions, which can be easily implemented into a computer program. The reason for the latter condition is that it will be simpler to code a set of analytical equations, instead of just using the tables and having to interpolate different values at each step.

We will use a model that is based on the data, assumptions and mathematics presented on U.S. Standard Atmosphere, 1976 (11), which works in a height range from 0 to 1000 km. For the sake of simplicity and usefulness, we have applied some modifications to the

mathematical expressions that are presented in the original U.S. Standard Atmosphere, that reduce its height interval upper limit to about 120 km.

Earth's atmosphere can be divided into several layers, each characterised by a certain temperature and pressure profile, which have been experimentally determined and can be approximated with a single equation that is solely a function of height. In U.S Standard Atmosphere, 1976, two types of height are defined: geometric and geopotential heights. The first one is simply the absolute elevation with respect to mean sea level. Geopotential height, on the other hand, can be thought as an adjusted geometric height for variations in the gravity field of the Earth.

According to U.S Standard Atmosphere, 1976, the layers from sea level up to about 86 km of geometric height, have their mathematical expressions defined as a function of geopotential height instead of geometric height. However, it is desirable for computing a rocket's trajectory that will cross this boundary, 86 km high, to always use geometric height. Therefore, we modified those expressions accordingly.

Again, according to the previous model, above a geometric height of 86 km, pressure computation at a certain height implies computing several equations. Each of those equations is related to a single of the trace constituents of the atmospheric air at that height. However, we have considered more appropriate to define pressure with just an approximate exponential function. This definition has good enough accordance with experimental data up to a height of 120 km.

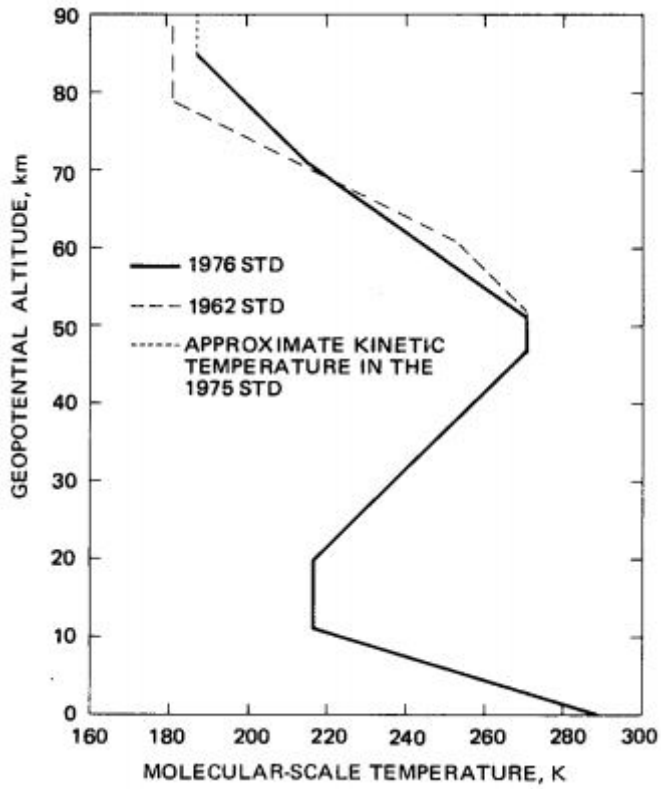

Figure 2.1: Temperature profile up to a geometric height of 90 km, according to different models that rely on experimental and statistical data. Source: reference (11).

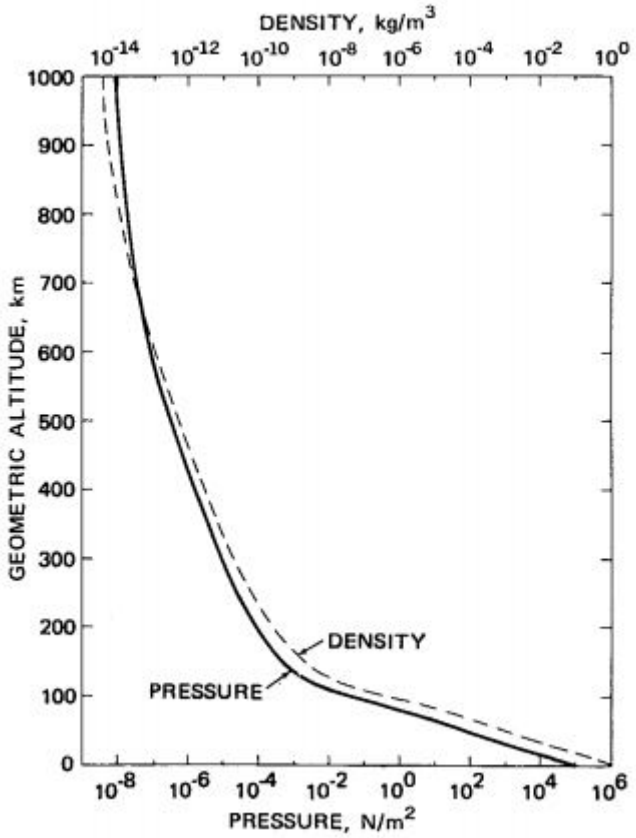

Figure 2.2: Pressure and density profile up to a geometric height of 1000 km, according to the model U.S. Standard Atmosphere, 1976. Source: reference (11).

2.5. Computing

We want to know how much $DeltaV$ our rocket must be provided with to achieve the requirement MIS-05. A simple solution to this problem is to execute the previous algorithm several times. At each iteration, a different value of $DeltaV$ will be used. We can start with a rough $DeltaV$ estimation, and then keep modifying its value by discrete amounts until reaching an approximate solution.

We can do a rough, short estimation of the $DeltaV$ needed by using (2.5). If we consider that $h_0 = 30$ km, then we require $\Delta V \geq 1171$ m/s to achieve an apogee of 100 km. Now, as we are not taking into account the atmospheric drag, it is obvious that the final solution will necessarily require a higher $DeltaV$.

Now, we can already proceed to execute our algorithm. The computer program gives us the velocity and heights at each step. As we expected, the value of initial velocity when accounting for atmospheric drag is higher than the result before: $DeltaV = 1253$ m/s. As we can see, even at a height of 30 km, the atmospheric drag has still a small but sensible effect, forcing us to spend an additional 82 m/s of ΔV to achieve the desired apogee.

However, in a real flight our rocket may not follow a perfect, straight trajectory. It may experience flight instability modes, or there could be a small misalignment with the thrust vector and the longitudinal axis of the rocket. In order to account with a certain margin of uncertainty, it is more appropriate to take a higher value of ΔV. We will consider a value of

ΔV that is just enough to achieve an apogee of 110 km. After another computer simulation, we finally find out the required value: $\Delta V = 1341$ m/s.

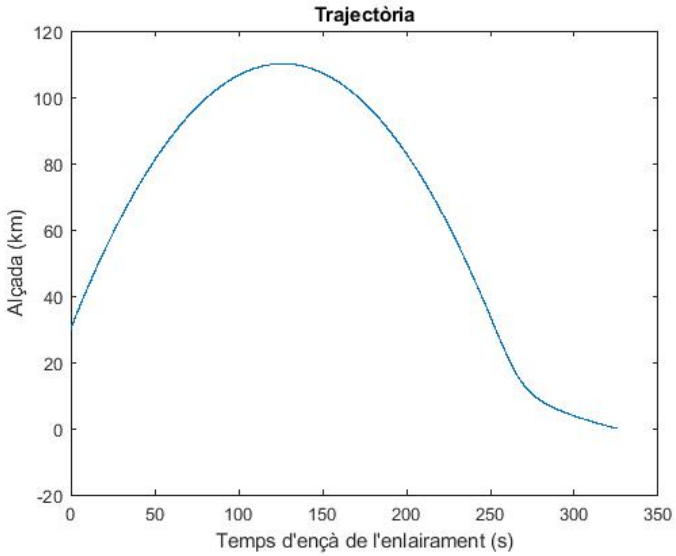

Figure 2.3: Simulated flight profile (height vs time) with our algorithm for a $DeltaV = 1341 m/s$. It takes 118 s to achieve the apogee at 100 km. It takes 311 s to complete the trajectory and hit the ground.

We must state, however, that the real minimum required ΔV will be actually slightly lower. The reason is that, as the rocket won't acquire all of the velocity instantaneously, but rather it will accelerate for a short period, when the engine cutoff happens, it will already be at a certain height, higher than 30 km.

2.6. Further engine definition

With the data that we already have, the minimum mass ratio, MR, of the rocket can be estimated. We consider a value for the gravity acceleration, g_0 equal to 9.81 m/s^2, and a conservative propellant specific impulse, I_{sp}, equal to 110 s, as it is the lowest one between those for KNDX and RNX. Then, we obtain that $MR \geq 3.47$, by using (2.2). The requirement MIS-02 implies a rocket payload, $m_{\text{pld}} = 0.3$ kg, while MIS-01 implies that the initial weight of the rocket, m_0, must be as low as possible. For this preliminary analysis, we will assume a total liftoff mass of the rocket equal to 5 kg. Therefore, the maximum dry mass of our rocket would be equal to 1.14 kg; in this case, the propellant mass would be equal to 3.56 kg, about the 71 % of initial weight. Therefore, the whole weight of the fairing; with all of its subsystems, such as the avionics and the recovery system; plus the weight of the engine should have to fit inside this narrow constraint. We expect the engine to be heavier than the fairing as it must withstand higher stresses during the flight.

We can also make a rough, conservative estimate on the Total Impulse of the engine. We consider, just as an example, a neutral thrust curve with a relatively low thrust of $F = 250$ N. We also assume, for further simplification, that the rocket is a particle with a constant mass $m_0 = 5$ kg, that it does not experience any atmospheric drag and that it is subject

to a constant gravitational deceleration $g_0 = 10$ m/s^2. In that case, according to (2.5), the rocket would accelerate steadily at $a_0 = 40$ m/s^2, which is the equivalent to 4 g's of force. Starting from rest, it would take the rocket a burn time $t_\mathrm{b} = 33'5$ s to achieve the desired ΔV. Finally, for such a steady thrust, the total impulse would simply be: $I_t = F\, t_\mathrm{b} = 8'375$ kN s. Again, that is a conservative value just meant for us to realise the order of magnitude of our rocket motor power. In fact, the real value, which we will estimate in the next chapter, will probably be lower. Just as a comparison, the *Zefiro*–9 solid rocket engine from the third stage of the *Vega* launch system, has a Total Impulse of $30'67$ MN s, many orders of magnitude higher than our engine.

CHAPTER 3. FUNCTIONAL DESIGN

3.1. Engine model

Our rocket engine model is based in the *Ideal Rocket Propulsion Unit*, as explained in (12). We initially use the same assumptions explained in the reference, but we also apply some additional correction factors to make the model more accurate.

3.1.1. Initial assumptions

To begin with, we assume that the propellant grains have an homogeneous composition and no physical defects. We disregard the ignition process of the engine, instead considering that it happens instantaneously. As well, we assume that the propellant grains burn only along the normal direction to their exposed surfaces. The grains will not suffer any stress nor physical deformation during the burn.

Inside the combustion chamber, the exhaust products are both homogeneous in chemical composition and in their physical properties (pressure and temperature). As well, they are at rest and remain in a state of stagnation. These exhaust products are only found in gaseous phase, with no mixed solid or liquid particles. The burn speed of the propellant grain follows a perfect power-law characterised by a coefficient, a, and an exponent, n, as we have already mentioned.

The exhaust products expand instantaneously and occupy the whole available volume inside the combustion chamber. We disregard the stresses on both the chamber and the nozzle, and instead assume that they both retain their initial physical shape. The exhaust products are treated as an ideal gas, and do not exchange any heat or work through the casing walls, neither through the nozzle.

The flow process through the nozzle is also considered to be reversible and, therefore, isentropic. The exhaust products behave as a laminar flow when flowing through the nozzle, without turbulence, and the presence of the boundary layer is ignored, as viscosity is not taken into account. As well, there are no losses due to friction with the nozzle walls. In fact, we consider that the flow is one-dimensional, so that all the flow properties are the same on any cross-section of the nozzle. We assume the expansion of the exhaust products to be smooth and uniform, so that no vibrations are produced. Furthermore, the flow choking condition is achieved exactly at the nozzle throat. Finally, there are no losses associated to shock waves created due to the nozzle being under-expanded, nor, logically, due to boundary layer detachment in the case of an over-expanded nozzle.

3.1.2. Correction factors

Starting from the initial assumptions, we will slightly improve our model by forcing the introduction of some correction factors.

In a conical rocket nozzle the flow is not ejected axially, but rather it has a certain lateral component that is dependant on the value of the divergence angle, α. This fact introduces

a certain loss to the effective exhaust velocity and, thus, momentum. We will introduce a multiplicative *exit momentum correction factor*, λ, that can be estimated with a simple arithmetical expression (13).

$$\lambda = \frac{1}{2}(1+\cos\alpha) \tag{3.1}$$

Therefore, the larger the divergence angle, α is, the higher the associated losses.

The nozzle throat contour must be as smooth as possible to maximise the mass flow of exhaust products. We call the ratio between the real flow rate and the ideal flow rate, the *discharge correction factor*, ζ_c, and we will assume it to be equal to 0.90 (13; 14).

The exhaust products will be slightly viscous and therefore, will form a thin boundary layer close to the nozzle walls. Assuming that the flow will not detach, there will be a decrease on the mean exit exhaust velocity with respect to an ideal case of disregarding the boundary layer. That decrease can be considered to account for a 1% (13). Therefore, we introduce a multiplicative *boundary layer correction factor* for the nozzle exit velocity, ζ_{BL}, equal to 0.99.

We initially assumed a purely gaseous flow. However, the reality is that the exhaust products from both KNDX and RNX propellants do contain both gaseous particles and liquid droplets. The theoretical ratio between the mass of those liquid particles compared to the total mass, β, can be used to correct the flow properties, through arithmetical expressions, to values that would match more closely the real flow (13),

$$k = \frac{(1-\beta)\,c_p + \beta\,c_l}{(1-\beta)\,c_v + \beta\,c_l} \tag{3.2}$$

where c_p is the specific heat at constant pressure of the gas species $[\frac{J}{mol\cdot K}]$, c_v is the specific heat at constant volume of the gas species, and c_l is the specific heat of the liquid species.

3.1.3. Algorithm

This is the numerical algorithm that we will use to compute the engine expected performance as a function of the varying design parameters. We use a notation in which the superscripts on any variable indicate the current simulation step. Meanwhile, the subscripts indicate the location of the variable. Specifically, the subscripts 0, 1, t and 2 refer to the combustion chamber, nozzle inlet, nozzle throat and nozzle outlet regions, respectively. It is an algorithm that, at each iteration, simulates the burning of a small thickness of the propellant grains.

Step 0: Initial conditions on the chamber and nozzle, values for the design parameters and simulation parameters are set.

The initial conditions on the chamber and nozzle are the initial temperature,T_0^0, pressure, P_0^0, and specific volumes, V_0^0. The design parameters are the ones that we have already defined. The main simulation parameter is the step size, ΔX.

Step 1.1: Compute the grain burn rate in the first step, r^1.

As we have already explained, we assume that the burn rate is a function of the chamber pressure in the previous simulation step, P_0^0, and that it follows a power law, according to a certain burn rate coefficient, a, and exponent, n.

$$r^1 = a\,(P_0^0)^n \tag{3.3}$$

Step 1.2: A certain amount of propellant is burned. The exposed surfaces recede each a certain thickness, ΔX. Therefore, a certain volume, ΔV, of propellant is immediately turned into exhaust products. This volume equals to a total mass, $\Delta m = \Delta V\,\rho$, where ρ is the density of the propellant grain. The time duration of this process is then easily computed:

$$\Delta t = \frac{\Delta X}{r} \tag{3.4}$$

The geometric properties of the grain after this surface recession are updated. The free chamber volume, V_{free}^1, in the first step is computed as the remainder of the chamber total volume and the grain volume.

Step 1.3: The mass flow rate of exhaust products production in the first step is computed:

$$\dot{m}_{\text{in}} = \frac{\Delta m}{\Delta t} \tag{3.5}$$

Step 1.4: The mass flow rate of exhaust products escaping through the nozzle in the first step is considered to be equal to 0.

Under the assumptions enunciated in this section, according to (15), we can compute the mass flow rate at any cross section across the nozzle. We must apply the *discharge correction factor*, ζ_{c}, in order to correct for the non-smoothness of the throat.

$$\dot{m}_{\text{out}} = \frac{A_{\text{t}}\,v_{\text{t}}}{V_{\text{t}}} = A_{\text{t}}\,P_1^0\,k\,\sqrt{\frac{[2/(k+1)]^{(k+1)/(k-1)}}{k\,R\,T_1}} \tag{3.6}$$

being A_{t} the area of the nozzle throat cross-section, P_1^0 the initial pressure at the nozzle inlet, k the ratio of specific heats of the propellant formulation and R the gas constant for the exhaust products.

For combustion chambers that are much wider than the nozzle throat, P_1^0 can be assumed to be the same than the pressure at any cross-section across the combustion chamber, again, according to Rocket Propulsion Elements (16).

Step 1.5: The total amount of exhaust products inside the chamber in the first step, m^1,is computed:

$$m^1 = m^0 + (\dot{m}_{\text{in}} + \dot{m}_{\text{out}})\,\Delta t^1 \tag{3.7}$$

being m^0 the initial mass of exhaust products in the combustion chamber, which is equal to 0.

The specific volume of the exhaust products inside the chamber in the first step, V_0^1, is computed as:

$$V_0^1 = \frac{V_{\text{free}}^1}{m^1} \tag{3.8}$$

The chamber pressure in the first step, P_0^1, is computed under the ideal gas assumption as:

$$P_0^1 = R\,\frac{T_0^1}{V_0^1} \tag{3.9}$$

Step 1.6: The thrust developed at the first step is computed.

Under our assumptions, the pressure of the exhaust products at the nozzle outlet, P_2^1, depends upon the outlet area according to the following expression:

$$\frac{A_{\text{t}}}{A_2} = \frac{V_{\text{t}}\,v_2}{V_2\,v_{\text{t}}} = \left(\frac{k+1}{2}\right)^{1/(k-1)} \left(\frac{P_2^1}{P_1}\right)^{1/k} \sqrt{\frac{k+1}{k-1}\left[1-\left(\frac{P_2^1}{P_1}\right)^{(k-1)/k}\right]} \tag{3.10}$$

The velocity of the exhaust products at the nozzle outlet can now be easily computed (17). We apply the exit momentum correction factor, λ, and the boundary layer correction factor, ζ_{BL}:

$$v_2^1 = \lambda\,\zeta_{\text{BL}} \sqrt{\frac{2\,k}{k-1}\,R\,T_1\left[1-\left(\frac{P_2^1}{P_1}\right)^{(k-1)/k}\right]} \tag{3.11}$$

Finally, we can compute the thrust at the first step with the following simplified expression, assuming the external pressure is negligible:

$$F = \dot{m}_{\text{out}}\,v_2^1 + (P_2^1 - P_{\text{atm}}^1)\,A_2 \tag{3.12}$$

Step 2: Steps 1.1 to 1.6 are executed until the whole propellant has been consumed.

Step 3: The chamber pressure decay is computed, now that there is no more propellant, until it gets down to a negligible value. For the sake of simplicity, we assume an exponential decay through time. This would be a problem of effusion (discharge of a gas through a hole into the vacuum), where pressure decreases as:

$$P_0 = P_{0_i}\,\exp -t/\tau \tag{3.13}$$

and

$$\tau \equiv \frac{V}{A_{\text{t}}}\left(\frac{2\,\pi M}{R\,T}\right)^{1/2} \tag{3.14}$$

being M the molar mass of the gases and P_{0_i} the chamber pressure at the moment of engine cutoff.

3.2. Integrated model engine-trajectory

We will use both the engine and the trajectory models to build a new, more complex algorithm that computes, as a function of the engine functional design parameters, not only the engine performance but the whole trajectory of the rocket. This new algorithm will be used for the subsequent work that is presented in this section.

Step 0: Initial conditions, design parameters and simulation parameters are defined. The initial air properties (pressure, temperature and density) are computed with the atmospheric model.

Initial conditions now include both chamber and nozzle conditions (stagnation temperature, pressure and specific volume) and initial rocket height and velocity. Initial velocity is assumed to be equal to 0. The design parameters are the engine functional configuration and the rocket drag coefficient and cross-section area, both used to compute the aerodynamic drag. The main simulation parameter is the step size, ΔX and the time step , Δt. The smaller these two parameters, the more accurate the results, but also the more computationally intensive.

Step 1.1: Steps 1.1 to 1.6 of the previous engine algorithm are executed. The thrust on the first simulation step is obtained.

Step 1.2: Steps 1.1 and 1.2 of the previous trajectory algorithm are executed to update the height of the rocket.

Step 2: Previous steps (1.1 and 1.2) are repeated until the propellant is completely exhausted.

Step 3: Both the step 3 of the engine algorithm and the step 2 of the trajectory algorithm are executed simultaneously. Keep computing both the engine performance, in a regime of exponentially decaying chamber pressure, and the rocket trajectory. Continue until the chamber pressure is reduced to ambient pressure.

Step 4: The step 2 of the trajectory algorithm is executed until the rocket falls to the ground.

We assume that the mass of the rocket is constant throughout time (dry mass). We conservatively consider the gravitational acceleration to be constant at a value of 9.80665 m/s^2.

3.3. Functional requirements and design parameters

We use the word *functional* to refer to everything that is directly related to the performance of the engine, to its thrust, specific impulse and total impulse. In this section we will establish some of the most important requirements and constraints for computing the performance. We will also explicitly define all of the available design parameters; that is, all of those magnitudes that we can choose to be adjusted during the design, while searching for the combination that better fulfils the functional requirements.

3.3.1. Defining functional requirements

According to the requirement MIS-03, the fairing must be designed in order to carry a *CanSat* as a payload. According to the *CanSat* standard, the devices must have a diameter equal to 66 mm and a height of 115 mm. Therefore, the fairing must be accordingly sized. We consider appropriate that both the base of the fairing and the engine have the same external diameter; therefore, the internal diameter of the combustion chamber must be greater than 66 mm.

Our engine will be characterised by a curve representing the time variation of chamber pressure with respect to time. In order to achieve maximum nozzle efficiency, this curve should be neutral and so it should be in a steady state at a constant pressure. This internal pressure will stress both the case and the nozzle walls. The higher these stresses are, the thicker and heavier the case and nozzle will have to be. Besides, the higher the inner pressure is, the longer and heavier the nozzle will need to be in order to expand the exhaust products to the desired exit pressure. Therefore, it is desirable to have a relatively low and neutral chamber pressure profile.

It is estimated that, below a chamber pressure equal to 0.15 MPa (18) below which the flame would most likely self-extinguish and propellant combustion would end. However, for the RNX propellant there is only experimental data of the burn rate performance for pressures greater than 2 MPa. Therefore, it is reasonable to aim for a steady chamber pressure equal to 2 MPa.

The exhaust products inside the chamber will have a high temperature. Therefore, the case and nozzle walls will rapidly heat up, decreasing their strength and experiencing thermal stresses. It will be preferable to use the propellant with the lowest possible combustion temperature and, as well, to reduce the burn time. At the same time, a lower burn time will come with higher values of engine thrust and accelerations imparted to the vehicle. These accelerations will cause further loads to the case and the fairing, can introduce flight instability modes and undesirable vibrations. Therefore, a trade-off must be made between the burn time and the maximum acceleration of the vehicle. For the moment we consider a maximum acceleration constraint equal to 150 m/s^2, which, for the $DeltaV$ computed in the previous section, corresponds to an approximate burn time of 9 s.

There is a minimum practical nozzle throat size, as a small throat increases the sensitivity on smoothness imperfections and defects introduced by the machining process. We define the minimum throat diameter at 7.5 mm. The nozzle should expand the exhaust gases until, ideally, the same pressure as atmospheric air for having maximum nozzle efficiency, corresponding to what is called the *adapted nozzle condition*.

Otherwise, the flow would be under expanded, with a subsequent loss of engine efficiency due to the appearance of oblique shock waves at the outlet. Over expansion could cause normal shockwaves inside the nozzle that would result in a subsonic ejection velocity. However, to expand further the exhaust products requires a longer and heavier nozzle. At the same time, the nozzle outlet cross-section should not have a bigger diameter than that of the rocket in order to not increase the atmospheric drag. According to the atmosphere model, at a height of 30 km the air pressure is equal to 1.7 KPa, so we must do a trade off, constrained by the maximum outlet diameter, between approaching this value as much as possible and keeping a reasonable nozzle weight and size.

Conical nozzles can be typically characterised by three diameters (inlet, throat and outlet)

and two angles: the convergence and divergence angles. Typical divergence semi-angles for rocket nozzles have values between 12° and 18°. For values greater than 18°, the risk of boundary layer detachment becomes critical; meanwhile, for values lower than 12°, the associated increase of nozzle weight usually becomes prohibitive. For the moment, we do not constraint the divergence semi-angle, waiting to assess how much it would affect our weight. For the convergence semi-angle, typical values are around 30°.

Finally, processing large propellant grains may be unpractical, as the cost, hazards and complexity increase with its size and mass. It may be more appropriate to work with smaller amounts of propellant at once, to make several identical grain segments. As an example, the *Solid Rocket Boosters* (SRBs) of the *Space Shuttle* used a total of four propellant segments. Even the case was manufactured out of four identical segments to lower manufacturing difficulties. In our case, we consider that the maximum mass of a single segment should be limited to 1 kg.

We compile here, as a list of requirements, everything that has just been discussed:

FUN-01: The internal diameter of the combustion chamber must be larger than 66 mm.

FUN-02: The internal pressure to time curve should be neutral and the steady value of pressure must be approximately equal to 2 MPa.

FUN-03: The rocket acceleration must not be higher than 150 m/s^2, which corresponds to an engine burn time longer than 9 s.

FUN-04: The diameter of the nozzle throat must be equal or larger than 7.5 mm.

FUN-05: The cross-section of the nozzle outlet must be equal or smaller than that of the rocket. As well, the pressure of the exhaust products at the nozzle outlets must be as close to the atmospheric pressure, 1.7 kPa, as possible.

FUN-06: The divergence semi-angle of the nozzle must be within 12° and 18°. The convergence semi-angle is equal to 30°.

FUN-07: The propellant will be made out of several segments, not heavier than 1 kg each.

Regarding the requirement FUN-01, for the moment we will consider a case internal diameter equal to 76 mm. The reason is that this diameter, being equal to three inches, is a common standard size for extruded metallic tubes made from aluminium and steel, which may be our materials of choice for the case.

Regarding the requirement FUN-05, for now we define a maximum acceptable nozzle outlet pressure equal to 10 kPa. It is possible to make a theoretical analysis of how an under expanded flow would adversely affect the performance of the engine, and to establish a maximum value more accurate. However, in this document we will not go into that much detail.

3.3.2. Functional design parameters

As we have already defined and established both the shape and the internal diameter of the case, the only magnitude left that can be modified as a design parameter is its length. For the nozzle, we will only consider as design parameters the size of the throat and the size of the outlet cross-section.

The shape and sizes of the grain and the choice of inhibited surfaces will also affect the performance of the engine. The geometry of the grain could be made really complex. Furthermore, several propellant segments could be used, each segment being an independently manufactured propellant grain and finally integrated into the engine. Making the propellant into several segments allows to reduce the amount of propellant that is handled and manufactured at a time, thus increasing safety and reducing costs, as the casts and devices for processing and manufacturing the propellant can be smaller.

Again, as an example, the *Solid Rocket Boosters* (SRB) from the *Space Shuttle* had a complex, 3-dimensional longitudinal cuts that allowed to obtain a certain pressure profile. However, we will only consider 2D grain geometries, shapes than can be determined from a single cross-section. 3D geometries are discarded for the complex machining processes that should be used after casting. Meanwhile, the simpler 2D geometries can be machined out of simple cross-section cutting and extruding operations.

Some 2D geometries can be defined by a small number of parameters. Some other geometries, such as Fynocil and Star Shapes, are more complex and require a relatively high number of geometric parameters (19). Again, for the sake of simplicity, we will not consider these complex shapes with many geometric parameters.

We compile the design parameters in the following list:

1. Internal length of the case.
2. Nozzle throat diameter.
3. Nozzle outlet diameter.
4. Shape and sizes of the grain (only 2D, simple shapes), as well as the number of segments.
5. Surfaces of the grain that are inhibited from burning.
6. Propellant formulation and all of its associated properties, which are assumed to be constant.

From now on, we will call any defined combination of the parameters 4, 5 and 6, a *grain functional configuration*. Analogously, we will call any combination of all six parameters, an *engine functional configuration*.

3.4. Engine functional design

3.4.1. Basic grain functional configurations

According to the requirement FUN-03, as our engine should have a relatively long burn time, only the smaller surfaces of the grains should be exposed to burning, while the larger surfaces should be inhibited. An option to achieve this is to use a single, cylindrical grain segment and inhibit the lateral and one of the end surfaces, so that the grain can only burn in a single section. This grain geometry is known as an *End-Burner*. In this configuration, the grain could be bonded to the case with the use of a proper liner and casting technique. It could also be free-standing inside the case, for which it would need an effective inhibitor,

as the hot exhaust products would inevitably seep through the gap between the lateral surface and the case walls. We will call this engine configuration *Option 1*. A simple variation over *Option 1*, which we will call *Option 2*, consists on exposing both end surfaces of the propellant segment. However, both Option 1 and Option 2 are undesirable, as they would both breach the requirement FUN-06.

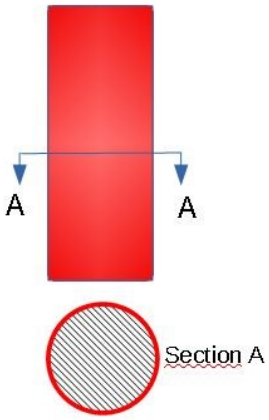

Figure 3.1: Schematic drawing of the grain configuration that we have called *Option 1*. Its inhibited surfaces are depicted in red; its exposed surfaces are depicted in scrapped grey.

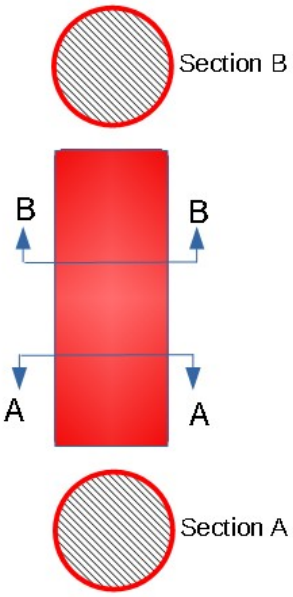

Figure 3.2: Schematic drawing of the grain configuration that we have called *Option 2*.

A simple alternative to both *Option 1* and *Option 2* would be to use, in both previous cases, several cylindrical grain segments instead of just a single one. We call these configurations *Option 3* and *Option 4*, respectively. Within *Option 3* and *Option 4*, there are lots of potentially viable engine functional configurations fulfilling all of the functional design requirements.

However, both *Option 3* and *Option 4* constrain a lot the flow of exhaust products inside the chamber. In both cases, a large part of the exhaust products would have to seep through the gap clearance between the lateral surface of the segments and the case. We can not currently predict what would happen in such a case. Our guess is that the gases would circulate fast through those gaps and turbulence would appear. A way to hold the grains in position would have to be engineered. Boundary layers would form in thin regions next to both the case internal walls and the inhibitors. Besides, these boundary layers would likely be turbulent, precisely due to the high velocities. All of this would cause an increase in the heat transfer to both the casing and the inhibitor, which is obviously undesirable (20). Moreover, we also consider that such a fast flow going around the propellant grains could be a potential source of vibrations. Therefore, both *Option 3* and *4* should also be discarded.

A more promising option consists on using several grain segments, each with a cylindrical, central port. These segments would have all of their surfaces inhibited, including the port surface, except for either a single or both ends. We call them both *Option 5* and *Option 6*,

respectively.

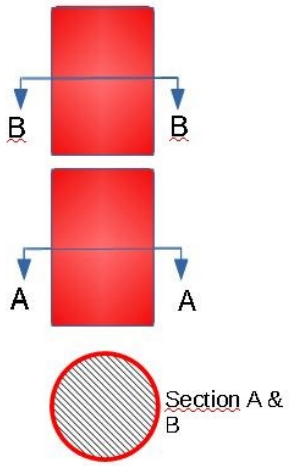

Figure 3.3: Schematic drawing of the grain configuration that we have called *Option 3*. In red, the inhibited surfaces. In scrapped grey, the burning surfaces. Just 2 propellant segments are depicted here; however, any number of segments is possible as a design parameter within this configuration.

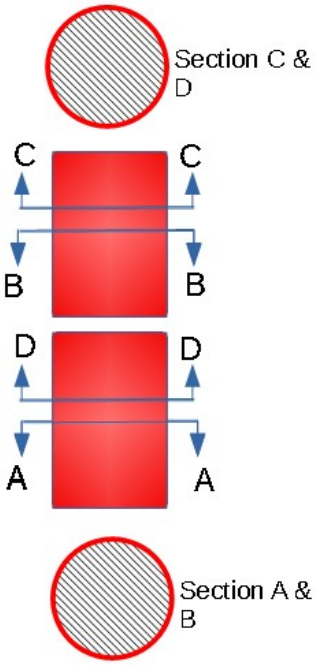

Figure 3.4: Schematic drawing of the grain configuration that we have called *Option 4*.

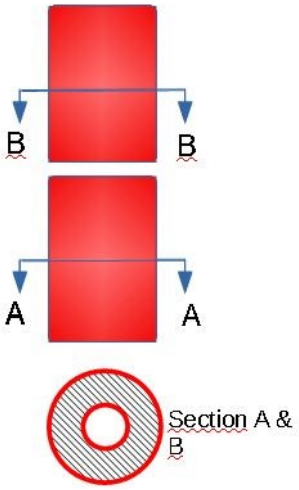

Figure 3.5: Schematic drawing of the grain configuration that we have called *Option 5*. In red, the inhibited surfaces. In scrapped grey, the exposed surfaces. Any number of segments would be theoretically possible.

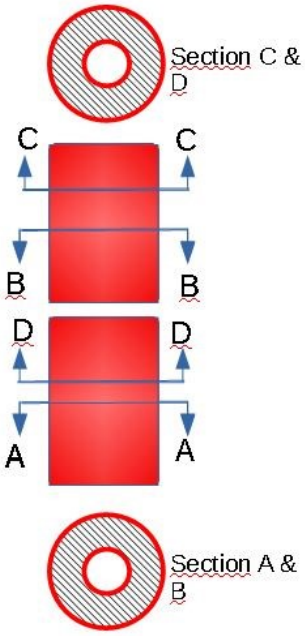

Figure 3.6: Schematic drawing of the grain configuration that we call *Option 6*.

The segments of both *Option 5* and *Option 6* could be either free-standing or bonded to the case. Case-bonding would require the development of a technique to bond the pre-casted grains into the casing using a liner. Free-standing is, however, preferred for simplifying the design, the engine manufacturing process and to increase the robustness of the engine.

From now on, we will use a better nomenclature whenever stating the grain functional configurations. This nomenclature call every possible configuration with a combination of three characters; two being numbers and a single letter, written in the following way: A-B-C. *A* refers to the number of exposed end surfaces of the grain, so it could be either 1 or 2. Therefore, a value *1* in *A* means that we are referring to *Option 5*, whilst a value of *Option 6* means we are talking about *Option 6*. *B* corresponds to the number of grain segments that are used. Finally, *C* could be either the letter *K* or *R*, whether we are considering the propellant formulation KNDX or RNX, respectively.

In a more informal way, we will refer to both previous *Option 5* and *Option 6* as *bypass grain configurations*. Such a geometry, in which the exhaust products go through a central port without burning the propellant, has never been used before, to the best of our knowledge, in solid rocket engines.

3.4.2. Grain configuration constraints

We define the *filling factor* as the ratio between the volume of the propellant grains and the total available volume inside the case. Some separation is needed inside the case between each two consecutive segments; therefore, having a large number of grain segments will degrade the *filling factor*. In the previous chapter we estimated a total propellant mass equal to 3.56 kg. Therefore, in order to fulfil requirement FUN-07, we must use at least four segments.

We define the *port-to-throat area ratio*, as its name suggests, as the ratio between the cross-sectional area of the grain port and the nozzle area. The narrower the port is with respect to the throat, the faster the exhaust products will flow through it. As has been already mentioned, a fast flow of exhaust products across a narrow gap will increase the heat transfer through a turbulent boundary layer. This would cause a phenomenon called *erosive burning*, in which there is a sudden increase in the burn rate. To minimise erosive burning, the *port-to-throat area ratio* should be greater than 4 (21) and, therefore, the port diameter shall be at least twice the nozzle throat diameter.

3.4.3. Method

There exist many sophisticated methods to optimise the grain geometry for a definite set of desired engine design requirements (22) which could be adapted to obtain the engine functional configuration that best fits our requirements. However, we won't follow such a complex approach, but we will rather use a conceptually simpler method, consisting on following several steps. For each step, we will adjust and optimise a single design parameter, until all of the functional requirements are fulfilled. We start with a set of preliminary engine functional configurations for both *Option 5* and *Option 6*. These are the following ones:

	1-4-K	1-5-K	1-6-K	1-4-R	1-5-R	1-6-R
L_c (mm)	450	450	450	450	450	450
d_c (mm)	76	76	76	76	76	76
d_t (mm)	7.5	7.5	7.5	7.5	7.5	7.5
d_o (mm)	75	75	75	75	75	75
L_g (mm)	107.5	107.5	107.5	107.5	107.5	107.5
d_{eg} (mm)	74	74	74	74	74	74
d_{pg} (mm)	15	15	15	15	15	15

Table 3.1: List of the preliminary engine functional configurations based on *Option 5*, named with their correspondent notation. L_c, d_c, d_t, d_o, L_g, d_{eg} and d_{pg} are the casing inner length, casing inner diameter, grain segment length, grain segment external diameter, grain segment port diameter, nozzle throat diameter and nozzle outlet diameter, respectively.

	2-4-K	2-5-K	2-6-K	2-4-R	2-5-R	2-6-R
L_c (mm)	450	450	450	450	450	450
d_c (mm)	76	76	76	76	76	76
d_t (mm)	7.5	7.5	7.5	7.5	7.5	7.5
d_o (mm)	75	75	75	75	75	75
L_g (mm)	107.5	107.5	107.5	107.5	107.5	107.5
d_{eg} (mm)	74	74	74	74	74	74
d_{pg} (mm)	15	15	15	15	15	15

Table 3.2: List of the preliminary engine functional configurations based on *Option 6*.

In these preliminary configurations, the length of the chamber, L_c, and the diameter of the chamber, d_c, have been chosen to have enough volume for the mass of propellant needed, as we estimated it in the previous chapter, while fulfilling the requirement FUN-01. The diameter of the throat, d_t has been set at its minimum value according to the requirement FUN-04. The diameter of the nozzle outlet, d_o, is a bit smaller than L_c, satisfying the requirement FUN-05. The length of the grain segments, L_g, has been set in order to have a separation of 5 mm between successive grain segments. The external diameter of the grain segments, d_{eg}, is slightly smaller than the internal chamber diameter, accounting for 1 mm of clearance with the casing walls. Finally, the grain port diameter, d_{pg}, is double that of the nozzle throat, meeting the nozzle-to-throat area ratio constraint.

These are the steps that will be followed for the engine functional design:

Step 0.1: First, we make a round of simulations of the preliminary engine configurations using the engine algorithm, and analyse the performance results for each.

Step 0.2: Those configurations that yield a chamber pressure, P_0, lower than that established by the requirement FUN-02 will be discarded, as the only solution would be to decrease further the nozzle throat diameter, thus breaching the requirement FUN-04.

Step 1.1: For the remaining configurations, on which P_0 will be greater than the requirement FUN-02, we will do several simulations, each time increasing the nozzle throat by a small amount until the desired P_0 is achieved.

Step 1.2: Those configurations that, at the nozzle outlet, have a pressure higher than that of atmospheric air, 1.7 kPa, will be discarded. The reason is that the only solution would be to further expand the exhaust products by increasing the diameter of the nozzle outlet and breaching the requirement FUN-05.

Step 2: We repeat the previous iterative simulation process with the engine algorithm, modifying the nozzle outlet diameter by a small amount until achieving the desired pressure at the outlet.

Step 3.1: We do another set of simulations for all the remaining configurations, this time with the integrated algorithm engine-trajectory. We iteratively modify the length of the grain segments until a height equal to 110 km is achieved and, thus, the requirement MIS-05 is fulfilled.

Step 3.2: Those configurations that breach the requirement FUN-03, will be discarded. We end up with a set of configurations that fulfil all of the engine functional requirements.

Step 4: Assess whether to modify the current configurations by increasing the number of grain segments.

3.4.4. Simulations

We start by executing the step 0.1 and appropriately organising the results in a table. In step 0.2, we discard the configuration 1-4-R, as its P_0 appears to be lower than 2 MPa.

	1-4-K	1-5-K	1-6-K	1-4-R	1-5-R	1-6-R
d_t (mm)	7.5	7.5	7.5	7.5	7.5	7.5
d_o (mm)	75	75	75	75	75	75
d_p (mm)	15	15	15	15	15	15
L_g (mm)	107.5	85	70	107.5	85	70
P_0 (MPa)	9.02	13.28	18.15	1.81	2.58	3.43
P_2 (kPa)	12.50	18.40	25.10	1.40	1.90	2.50

Table 3.3: Performance results of Step 0.1 for the preliminary engine functional configurations based on *Option 5*.

	2-4-K	2-5-K	2-6-K	2-4-R	2-5-R	2-6-R
d_t (mm)	7.5	7.5	7.5	7.5	7.5	7.5
d_o (mm)	75	75	75	75	75	75
d_p (mm)	15	15	15	15	15	15
L_g (mm)	107.5	85	70	107.5	85	70
P_0 (MPa)	29.39	42.17	56.00	5.38	7.61	10.07
P_2 (kPa)	40.60	58.20	77.30	3.90	5.50	7.30

Table 3.4: Results of step 0.1 for the preliminary engine functional configurations based on *Option 6*.

Continuing with step 1.1, we must now adjust the nozzle diameter of the remaining configurations until achieving a chamber pressure approximately equal to 2 MPa. The results

are presented on tables and, in step 1.2, we notice that all of the current engine functional configurations have under expanded nozzles, which is a problem, as we can not expand them any further without breaching the requirement FUN-05. However, there is a clear difference between those configurations based on the propellant KNDX and those based on RNX, the latter ones being much closer to the desired results. The solution that we take is to discard the propellant KNDX as, on account of its burn rate characteristics, it is not appropriate enough for our engine. Therefore, we are left with just five engine functional configurations.

	1-4-K	1-5-K	1-6-K	1-5-R	1-6-R
d_t (mm)	11.9	13.1	14.2	8	8.8
d_o (mm)	75	75	75	75	75
d_p (mm)	24	27	29	19	18
L_g (mm)	107.5	85	70	85	70
P_0 (MPa)	2.01	2.01	2.00	2.02	2.01
P_2 (kPa)	7.90	9.80	11.80	1.80	2.20

Table 3.5: Results of Step 1.1 for the engine functional configurations based on *Option 5*.

	2-4-K	2-5-K	2-6-K	2-4-R	2-5-R	2-6-R
d_t (mm)	16	17.5	18.7	10	11.1	12.1
d_o (mm)	75	75	75	75	75	75
d_p (mm)	32	35	38	21	23	25
L_g (mm)	107.5	85	70	107.5	85	70
P_0 (MPa)	2.02	2.02	2.01	2.04	2.03	2.00
P_2 (kPa)	15.60	19.20	22.30	3.10	3.90	4.80

Table 3.6: Results of Step 1.1 for the preliminary engine functional configurations based on *Option 6*.

As all of our current engine functional configurations have a nozzle outlet pressure greater than 1.7 kPa, there is no point in executing the step 2. We directly do the simulations corresponding to step 3.1 and modify the grain segments length. In step 3.2, we discard both 2-5-R and 2-6-R options, as their associated maximum acceleration is higher than 150 m/s^2. We are left with just three valid configurations: 1-5-R, 1-6-R and 2-4-R.

	1-5-R	1-6-R	2-4-R	2-5-R	2-6-R
L_c (mm)	500	492	484	495	510
d_t (mm)	8	8.8	10	11.1	12.1
d_o (mm)	75	75	75	75	75
d_p (mm)	19	18	21	23	25
L_g (mm)	95	77	116	94	80
P_0 (MPa)	2.02	2.01	2.04	2.03	2.00
P_2 (kPa)	1.80	2.20	3.10	3.90	4.80
a_m (m/s^2)	86.37	104.81	137.78	168.83	197.20
h_m (km)	110.24	110.62	110.69	110.53	110.41
I_t (kN s)	4.15	4.04	3.93	3.88	3.85
I_{sp} (s)	126.43	125.61	124.46	123.36	122.39

Table 3.7: Results of Step 3.1. This time we not only compute the engine performance, but also the rocket trajectory. a_m, h_m, I_t and I_{sp} stand for the maximum acceleration, height, total impulse and specific impulse, respectively.

In step 4, we analyse configurations that are a modification of 1-6-R, with just more, and shorter, segments added: 1-7-R, 1-8-R, and so on. For each case, we optimise them by repeating the previous steps, from 0.1 to 3.2. We continue analysing new configurations until 1-9-R, which breaches the requirement FUN-03. When comparing these results with those of 3.7, we can see that the results of both configurations 1-8-R and 2-4-R are almost the same. Therefore, we discard 1-8-R in favour of the latter, as 2-4-R has a larger *filling factor*.

	1-7-R	1-8-R	1-9-R
L_c (mm)	502	474	513
d_c (mm)	76	76	76
d_t (mm)	9.4	10	10.6
d_o (mm)	75	75	75
L_g (mm)	67	59	52
d_{eg} (mm)	74	74	74
d_{pg} (mm)	21	22	22
P_0 (MPa)	2.01	2.01	2.02
P_2 (kPa)	2.60	3.00	3.50
a_m (m/s^2)	119.67	135.84	152.96
h_m (km)	110.91	111.29	110.87
I_t (kN s)	3.99	3.97	3.91
I_{sp} (s)	125.02	124.43	123.84
b_{sp} (s)	20.15	17.72	15.62

Table 3.8: Potential engine functional configurations with a greater number of segments. As we increase this magnitude, the maximum acceleration increases, until being higher than 150 m/s^2.

Therefore, we end up with just 4 potential engine functional configurations, all of them based on the propellant formulation *RNX*. However, there is a performance parameter that we have not yet taken much into account: the burn time, b_t. As we have already

mentioned in this chapter, the larger the burn time of the engine, the greater will be the thermal stresses of both the casing and the nozzle. In order to further assess between these 4 remaining configurations and decide on a single one, we must advance in the design and analyse how these thermal stresses affect our engine.

	1-5-R	1-6-R	1-7-R	2-4-R
L_c (mm)	500	492	502	484
d_c (mm)	76	76	76	76
d_t (mm)	8	8.8	9.4	10
d_o (mm)	75	75	75	75
L_g (mm)	95	77	67	116
d_{eg} (mm)	74	74	74	74
d_{pg} (mm)	19	18	21	21
P_0 (MPa)	2.02	2.01	2.01	2.04
P_2 (kPa)	1.80	2.20	2.60	3.10
a_m (m/s^2)	86.37	104.81	119.67	137.78
h_m (km)	110.24	110.62	110.91	110.53
I_t (kN s)	4.15	4.04	3.99	3.93
I_{sp} (s)	126.43	125.61	125.02	124.46
b_t (s)	28.53	23.14	20.15	17.34
m_{prop} (kg)	3.35	3.28	3.26	3.22

Table 3.9: Final table of all the engine functional configurations that fulfil the functional requirements and, therefore, are feasible.

CHAPTER 4. THERMO-STRUCTURAL DESIGN

4.1. Structural model

The structural model will allow us to describe the loads and stresses acting on the case, and how they depend on certain design parameters. As we will see, doing the same for the nozzle would require a different model.

There will be four main sources of loads and stresses: the chamber pressure, the thermal gradient across the walls of the case and nozzle, and the flight derived accelerations and vibrations. In the last chapter we already established a requirement, FUN-03, for constraining the maximum acceleration, so, for the moment, we disregard the effect of accelerations. Vibrations are complex to model and to study; therefore, we will focus on the remaining two sources of stresses.

4.1.1. Assumptions

We assume that the case is made of isotropic materials; that is, it has identical properties on all directions. As well, it does not have any cracks nor defects, and its chemical composition is homogeneous, without impurities.

We assume that the case is a shell, a condition that stands true whether its thickness is about 20 times smaller than the inner diameter, or smaller (23; 24). We consider that the case internal pressure, P_0, and exhaust products temperature, T_0, are constant and axisymmetric. Moreover, the case is in a state of internal forces equilibrium. Its thermal properties and linear expansion coefficient do not depend on temperature.

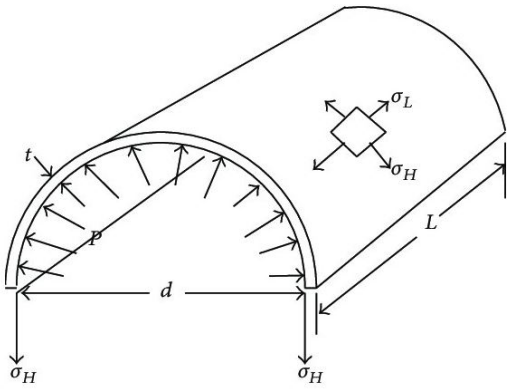

Figure 4.1: Schematic of a thin cylinder under an internal stress, such is the case with our combustion chamber, and the subsequent stresses that it holds. Source: reference (24).

Finally, we will call *equivalent stress*, σ_{eq}, to the scalar sum of all the stresses in the case, which is a worst-case guess on the value of the real stress.

4.1.2. In-flight loads

The significant value of internal pressure inside the combustion chamber, P_0, during the combustion would cause triaxial stresses. Specifically, these stresses would have a tangential (also called hoop or circumferential), σ_θ^c, a longitudinal (also called axial), σ_l^c and a radial, σ_r^c, component. The value of the radial stress can be neglected under the thin cylinder assumption, which stands for our casing. Both remaining stresses can be easily computed by using membrane theory of shells (23), as a function of wall thickness, chamber diameter and pressure value.

$$\sigma_\theta^c = (P_0 - P_e)\frac{d_i^c}{2\,t^c} \tag{4.1}$$

$$\sigma_l^c = (P_0 - P_e)\frac{d_i^c}{4\,t^c} \tag{4.2}$$

where P_e is the atmospheric pressure, d_i^c the internal diameter of the case, and t^c the thickness of the case.

These stress components would cause, respectively, both a circumferential, ε_θ^c, and longitudinal, ε_l^c, strain, resulting in a growth of the casing in both its diameter and length, respectively.

$$\varepsilon_\theta^c = \sigma_\theta^c \frac{(1-\frac{\nu^c}{2})}{2\,E^c} \tag{4.3}$$

$$\varepsilon_l^c = \sigma_l^c \frac{(1-2\,\nu^c)}{E^c} \tag{4.4}$$

being ν^c the Poisson ratio coefficient of the casing, and E^c Young's elastic modulus of the casing.

The other source of stress is the temperature gradient across the walls. When it is heated, the internal case wall expands according to a certain linear coefficient of expansion, λ_L, while the cooler outer surface expands less. This difference of strains generates an internal stress. Specifically, a compressive stress appears on the inner surface and a tensile stress acts on the outer surface (25). We will compute the equivalent stress on the case by adding the value of these three stresses.

$$\sigma_t^c = \frac{2\,\lambda_L\,E^c\,\Delta T}{(1-\nu^c)} \tag{4.5}$$

where λ is the linear coefficient of thermal expansion, E^c is Young's elastic modulus, ΔT the temperature increase across the wall, and ν^c is Poisson ratio coefficient.

4.1.3. Structural requirements

To ensure that the case will be able to bear the stresses, we must define a safety margin. Normally, a *Maximum Expected Operating Pressure* (MEOP) value is established for a

certain rocket engine design. A *Design Pressure* for the structural configuration, equal to 1.20 times the MEOP is then defined. The *Yield Pressure*, which is the value of pressure at which the structure would start to experience yielding, should be, at least, 1.10 times the *Design Pressure* (26). In our case, we consider a safety margin equal to 1.5.

The structural mass of the case should be as low as possible. In the last chapter we found out that a total mass of propellant between 3.35 and 3.22 kg was needed. We consider reasonable to aim for a propellant to structure mass equal to 10:1.

Both structural requirements are here defined:

STR-01: The ratio between the yield strength of the case material and the highest equivalent stress during the burn (worst-case scenario) must be at least equal to 1.5.

STR-02: The mass of the case shall not exceed 335 g.

4.2. Model of transient heat transfer

The heating of the case will not only cause thermal stresses, but it will also reduce its yield strength (27), (28): the highest the temperature of the case, the less likely it will be able to withstand the stresses. Therefore, we must predict the temperature of the case walls at the same time that the stresses are computed. *Finite Element Methods* are usually used to discretize the case and the nozzle into a grid and solve the problem of transient heat transfer (29). However, to compute the temperature as a function of time and a single spatial dimension, across the case walls, we will use a simpler method of Finite Differences.

4.2.1. Assumptions

We assume that the heat transfer is axisymmetric along the chamber. A boundary layer is formed between the hot exhaust products and the walls, where all the heat transfer happens only through convection, while we ignore the contribution of both radiation and conduction. In fact, radiation represents a tangible amount of heat transfer (30), but we neglect it for the sake of simplicity. Inside the walls, heat is transferred by conduction. Some heat flux happens as well from the walls to the outer atmosphere, through radiation.

As with the structural model, we consider isotropic materials and a perfectly cylindrical case with a constant thickness. The temperature of the gases inside the case, T_0, is constant.

4.2.2. Initial conditions

We will discretize the engine case into a mesh of concentric cylinders, each one being a node at a certain temperature, and having a thickness equal to Δr. We will compute temperature distributions at all the nodes for different time steps, each one having a duration equal to Δt. The smaller that both Δr and Δt are, the more accurate the results will likely be (31).

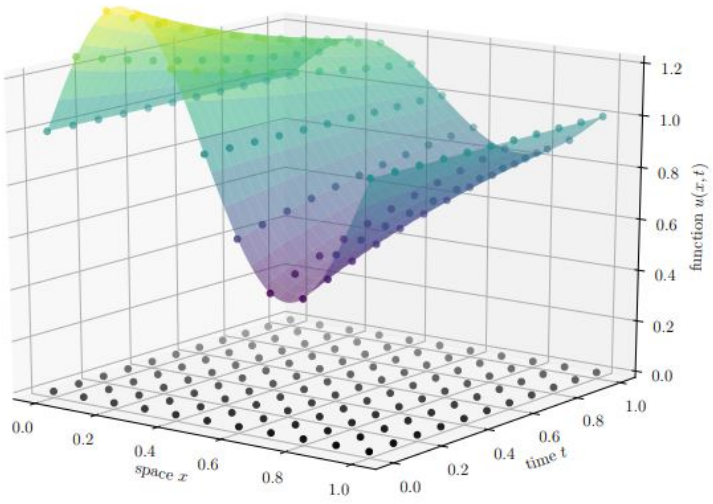

Figure 4.2: Generic graphical representation of how a problem like transient heat transfer is approached with a numerical method of *Finite Differences*. Both time and a single space dimensional are converted into a mesh. A certain function (coloured surface) is then iteratively evaluated at each point of the mesh. Source: reference (31).

At the first time step all of the nodes will be at a uniform distribution at the atmospheric temperature, defining the initial condition. The problem will not have boundary conditions, as the temperature as a function of time in both the first and last points of the space dominion will be computed through two separate formulas that will be presented later.

4.2.3. Mathematical model

The convective heat transfer between the boundary layer of exhaust products and the walls will be characterised by a *film coefficient*: h_g. We will compute it using a semi-empirical expression (32; 33).

$$h_g = 3.025\,10^{-3}\,\frac{\bar{c}}{d_i^{c\,0.2}}\left(\frac{m_{\mathrm{p0}}}{t_i A_i^c}\right)^{0.8}\left[1+\left(\frac{d_i^c}{L_i^c}\right)^{0.7}\right] \tag{4.6}$$

where $\bar{c}$ is the specific heat of the exhaust products, m_{p0} is the initial mass of propellant, t_{b} is the burn time of the engine, d^{c_i} the inner diameter of the case, A^{c_i}: Inner cross section area of the case, and L^{c_i} the inner length of the case.

Now we can easily compute the heat transfer rate, q_{in} as:

$$q_{\mathrm{in}} = h_g\,(T_0 - T_1^n) \tag{4.7}$$

being T_1^n the temperature of the first node of the wall at any given, and n the time step.

We will express the conductive heat transfer that happens inside the walls, q_{cond}, through Fourier's law of heat conduction:

$$\frac{\partial T}{\partial t} = \frac{\kappa}{\rho\,\bar{c}}\frac{\partial^2 T}{\partial x^2} = \alpha\frac{\partial^2 T}{\partial x^2} \tag{4.8}$$

where κ is the thermal conductivity of the material, $\bar{c}$ the specific heat of the material, and α the diffusivity of the material, computed from its properties.

Finally, we must estimate the amount of radiative heat transfer from the walls to the external atmosphere. As it is a function of the temperature to the fourth power, and the atmosphere will be at a lower temperature than the walls, we will neglect its temperature. Then,

$$q_{\text{out}} = \sigma\left[\varepsilon_c\left(T_p^n\right)^4 - \varepsilon_{\text{atm}}\left(T_{\text{atm}}\right)^4\right] \approx \sigma\,\varepsilon_c\left(T_c^n\right)^4 \tag{4.9}$$

where σ is the Stefan-Boltzmann constant, $\varepsilon_c \& \varepsilon_{\text{atm}}$ the emissivities of the casing and the atmosphere, respectively, $T_c^n \& T_{\text{atm}}$ the temperatures of the wall at the n-th time step and the temperature of the atmosphere, respectively.

4.2.4. Discretization

As has already been mentioned, both the walls of the case and the time are discretised, characterised by both a space step size, Δr, and a time step size, Δt.

Therefore, we can imagine this mesh as an $m \times n$ matrix. Each of the m rows of the matrix corresponds to the whole thickness of the case at a single time instant. Each of the n columns represents the time history at any discrete point of the walls. The upper row is filled with the initial condition. As we have no boundary conditions, the first and last columns have no values initially assigned.

Now, we will discretize equation 4.8 through both a forward, centred and backward difference in order to cover all points of the mesh, including the boundaries. We refer to any position on this matrix using the following notation: T_k^c; where c is the current time step and k is the current wall node. Hence,

$$\frac{T_1^{c+1} - T_1^c}{\Delta t} = \alpha\frac{T_2^c - T_1^c}{\Delta r^2} \tag{4.10}$$

$$\frac{T_k^{c+1} - T_k^c}{\Delta t} = \alpha\frac{T_{k+1}^c - 2\,T_k^c + T_{k-1}^c}{\Delta r^2} \tag{4.11}$$

$$\frac{T_n^{c+1} - T_n^c}{\Delta t} = \alpha\frac{T_n^c - T_{n-1}^c}{\Delta r^2} \tag{4.12}$$

4.3. Case configurations

We consider our case as a cylindrical pressure vessel with thin walls. A material of high strength is needed to withstand the mechanical stresses. At the same time, exceptional thermal properties and resistance is needed. A relatively simple design option consists of using a metal case (mechanical properties) together with a cooling mechanism, as we will discuss in this section.

4.3.1. Structural materials

Many materials have been used to manufacture solid rocket engine cases: metals, composite materials consisting of a plastic matrix and a reinforcement and a combination of a metallic structure with external wound filament as a reinforcement (34). We will only consider metallic materials as they have a relatively low cost and great mechanical properties: high strength and ductility. However, this comes at the cost of high densities. The main options are either steel or aluminium; rather than alloys of nickel and titanium, which would be more expensive.

4.3.1.1. Steel

Thousands of different steel alloys exist, each made from iron and a certain combination of alloying elements such as carbon, chromium and manganese, among others (35). These alloys can be classified in many wide categories, such as stainless steels, alloy steels and carbon steels, which are the most widely used in structural components. They have generally high densities, high strengths and good thermal properties such as high melting temperatures and comparatively low thermal conductivity.

Low-carbon steels, have a relatively low strength and hardness, but are ductile and tough (36) and reasonably inexpensive; they are frequently used for structural applications. Medium-carbon steels have a comparatively larger strength and smaller ductility and toughness; they are also used for structures bearing large loads. High-Carbon Steels are the ones with the higher strength and lesser ductility. They are used especially for forming cutting tools. Low-carbon steels are an interesting option for our engine case, thanks to their availability and ductility. This latter property is important from a safety point of view, as a ductile case will yield before breaking, and there is a higher chance that it will leak instead of experiencing a brittle fracture and, therefore, a burst (37). We consider for the case the Low-Carbon Steel AISI 1018, which contains a 0.18% mass weight of carbon (38).

	ρ (kg/m^3)	E (GPa)	σ_y (MPa)	ν	$\%EL$	α (m^2/s)	λ_L (m/(m K))
AISI 1018	7870	200	370	0.29	15	1.36×10^{-5}	12×10^{-6}

Table 4.1: Mechanical and thermal properties of AISI 1018 steel alloy at room temperature. ρ, E, σ_y, ν and $\%EL$ are the material density, modulus of elasticity, yield strength, Poisson ratio and ductility, expressed in percent elongation, respectively. α and λ_L are the thermal properties; the diffusivity and the coefficient of linear expansion at room temperature. Source: reference (38).

4.3.1.2. Aluminium

Aluminium alloys have much lower densities than steels, as well as lower melting temperatures and higher thermal conductivities. The most widely used aluminium alloys for structural applications in the aerospace industry are those of the families 8xxx, 7xxx and 2xxx. However, there are a few interesting alloys in the family 6xxx, such as 6061-T6.

The alloys of family 8xxx, made from aluminium and lithium, have exceptional mechanical properties but are the most expensive ones. The alloys on family 7xxx, such as 7075-T6,

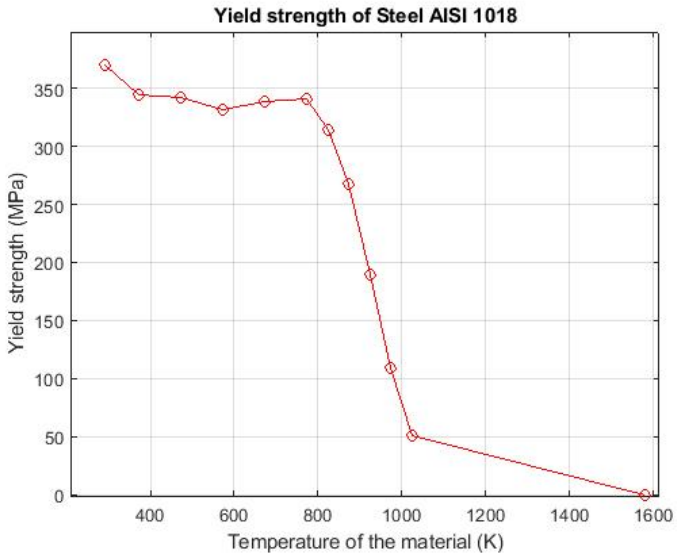

Figure 4.3: Decrease in the yield strength of AISI 1018 as a function of temperature. Plotted from a linear interpolation of the data presented in reference (27).

are combined with zinc and have a high yield strength and a low ductility and thermal diffusivity. Aluminium is combined with copper in the family 2xxx, acquiring a smaller strength and higher ductility and thermal diffusivity than the previously mentioned alloys. The alloy 6061-T6 has a lower strength than the other previous options, but also a high ductility and thermal diffusivity, as well as the lowest cost of all. Therefore, we consider this latter option as the most suitable aluminium alloy for our purposes.

	ρ (kg/m^3)	E (GPa)	σ_y (MPa)	ν	$\%EL$	α (m^2/s)	λ_L (m/(m K))
Al. 6061-T6	2700	68.9	276	0.33	17	6.90×10^{-5}	25.2×10^{-6}

Table 4.2: Mechanical and thermal properties of aluminium alloy 6061-T6 at room temperature. Source: reference (28).

4.3.2. Thermal protection materials

Three methods are used typically in solid rocket engines for providing thermal protection to the cases and the nozzles (39): regenerative cooling, radiation cooling and ablative cooling, also called heat sink cooling. Both the first and the second methods are extremely complex, not practical for small engines, so we only consider the third option.

The ablative cooling method consists on covering the internal surface of the case with a layer of a material with ablative properties. Once this material comes in contact with the hot exhaust products, it decomposes by pyrolysis by an endothermic chemical reaction, leaving a layer of char as residue, which insulates and restricts the heat transfer to the case. The relatively cold gases that are generated from this decomposition form a temporary boundary layer closely tied to the walls that further limits the heat transfer.

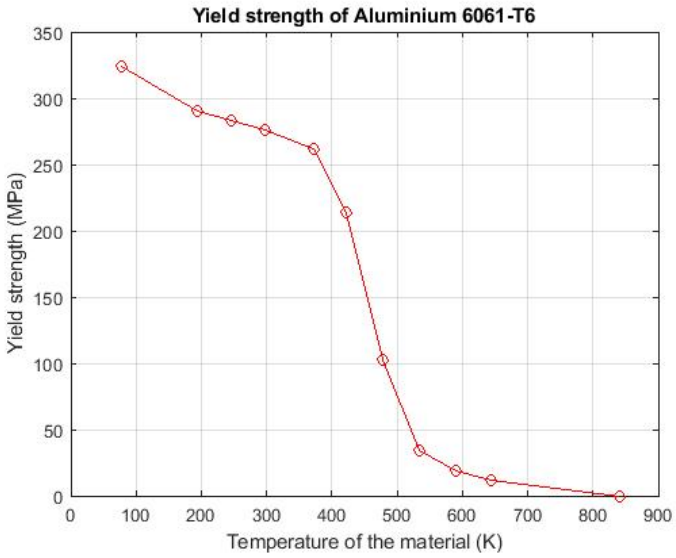

Figure 4.4: Decrease in the yield strength of Aluminium 6061-T6 as a function of temperature. Plotted from a linear interpolation of the data presented in reference (28).

Ablative materials are usually based on composite materials, made up from a polymer-based matrix and reinforcement fibres (40), (41). Thermosetting resins, such as epoxy, have been widely used in the aerospace industry; both epoxy and polyester have a low cost and are potentially feasible options (42). As a starting point, we will consider them as standalone ablatives, without any reinforcement.

	κ (W/m K)	$\bar{c}$ (J/kg K)	ρ (kg/m^3)	α (m^2/s)
Epoxy resin	0.35	1883	1149	1.62×10^{-7}
Polyester resin	0.24	1000	1370	1.75×10^{-7}

Table 4.3: Thermal properties of both candidates to ablative coating for our engine. κ, $\bar{c}$, ρ and α are the thermal conductivity, specific heat, density and diffusivity, respectively. Source: reference (42).

4.4. Coupled thermo-structural model

The thermo-structural model combines the three main concepts that we have discussed in this chapter and will allow us to make a proper design of the rocket engine case:

1. The mechanical properties of the case material are not constant, but rather they change with temperature.
2. During the combustion, the case walls are heated. The resultant temperature distribution can be simulated with a model of transient heat transfer.
3. The case experiences three different stresses due to both the internal pressure and the heating. The equivalent stress is computed as the addition of those.

4.4.1. Design parameters

In this list the design parameters to be determined are stated orderly:

1. Material of the case and the ablative coating.
2. Thickness of the case. The larger it is, the smaller the hoop and longitudinal stresses will be.
3. Thickness of the coating. The thicker it is, the larger the thermal protection provided; the ablative coating will regress and decompose at a certain *erosion rate*.
4. Burn time of the engine. The longer the burn is, the larger the heat transfer that must be endured.

Regarding the burn time parameter, we consider a possible interval between 17 s and 28 s, as the final engine functional configurations of the last chapter were within this values.

The geometry of the chamber, the thermodynamic properties of the exhaust products and the chamber pressure have a huge effect on the heat transfer and the structural integrity of the case. However, as these variables have already been addressed on the previous chapter, they are treated as conditions of the problem, instead of design parameters.

4.4.2. Algorithm

Step 0: The design parameters, simulation parameters and initial conditions of the problem are established.

The main simulation parameters are the thickness step size, Δx, and the time step size, Δt.

Step 1.1: Both the convective heat flux into the walls and the radiative heat flux out of the walls on the second time step are computed.

First and foremost, the heat transfer coefficient on the boundary layer must be computed. The analytical equation for convective heat transfer that has been presented, back in this chapter, is applied. A constant emissivity is considered for the walls material.

Step 1.2: The temperature distribution on the walls on the second time step is computed.

The discretised equations for one-dimensional transient heat transfer, that have been presented in this chapter, are used.

Step 1.3: The arithmetical mean of the wall temperature on the second time step is computed.

Step 1.4: The yield strength of the wall material on the second time step is computed.

The curves presented in 4.3 and 4.4 are used for this purpose.

Step 1.5: The stresses acting on the walls on the second time step are computed. The equivalent stress is obtained by adding them.

Step 1.6: It is addressed whether or not the resultant stress does fulfil the requirement STR-01.

Step 2: Steps 1.1 to 1.6 are repeated until the propellant is exhausted.

Once the simulation ends, we will address the *minimum safety margin*, which will be the smallest ratio obtained between the yield strength of the material and the equivalent stress. The *minimum safety margin* will allow us to address the performance of a certain structural configuration, and whether or not the requirement STR-01 is fulfilled. As in the previous chapter, this algorithm has been implemented into a Matlab program.

4.5. Case design

We will now evaluate the different casing configurations using the thermo-structural algorithm and determine which option is the more appropriate.

4.5.1. Method

As has been mentioned in this chapter, there are four design parameters to be determined. We call *Option 1*, those structural configurations that have an aluminium case and an internal layer of epoxy resin. *Option 2* is used to refer to those configurations with an aluminium case and a coating of polyester resin. *Option 3* and *Option 4* are those configurations consisting on a steel case and an epoxy and polyester resin coating, respectively.

Within each one of those configurations there are still three design parameters left. Using the previous algorithm, we will fix two of the parameters and compute the *minimum safety margin* for several values of the third parameter. Then, we will explore the parameter space by changing one design parameter while the remaining two are kept fixed. We will repeat the process a third time to be able to address all the possibilities.

This data will be displayed in a 2D plot for an easier analysis. The vertical axis of this plot will be the coating thickness, whilst the horizontal axis will correspond to the *minimum safety margin*. The variation of the remaining two design parameters will be displayed as a stack of colour-coded curves.

4.5.2. Simulations and results

For *Option 1*, the results are the expected ones. From the 2D plot, it can be deduced that, the larger the burn time is, the thicker the coating must be. As well, the thicker the case is, the thinner the coating can be.

According to the requirement STR-02, we not only have to take into account the performance of a certain structural configuration, but also its weight.

For now, a burn time of 28 s is considered (worst-case scenario). A potential design could consist on an aluminium case with a thickness equal to 1.5 mm and an epoxy coating equal to 2.2 mm; we call this design *S1*. Another design option would be to use the same materials, but reduce the case thickness and thicken the coating; we call it *S2*. Another design would consist on having a steel case, 1 mm thick, and a thin epoxy resin coating; it is called *S3*. Finally, the thickness of the steel case could be further reduced and instead thicken the coating; that design option is named *S4*.

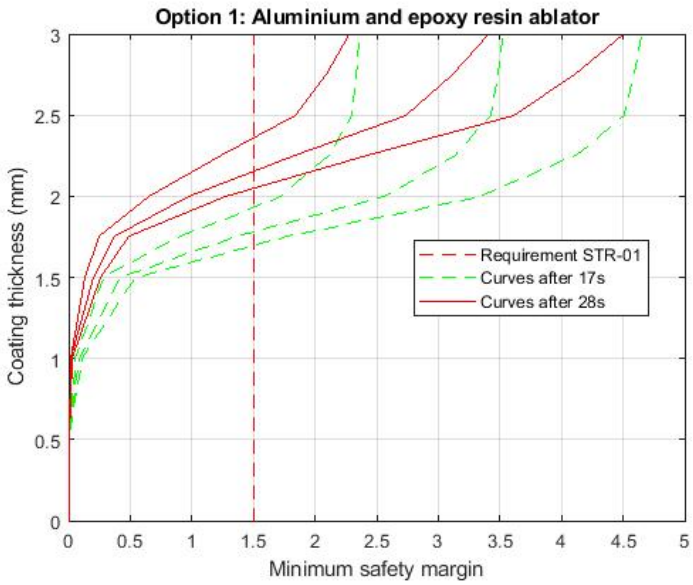

Figure 4.5: Performance results for *Option 1*. At the right of the vertical, red, dashed line, there are the feasible structural configurations. The red, solid curves correspond to a burn time equal to 28 s, whilst the green, dashed curves correspond to a burn time of 17 s. Each one of the red, solid curves is associated with a case thickness equal to 1 mm, 1.5 mm and 2 mm, respectively, and the same for the green, dashed curves.

We conclude that *Option 2* is less effective than the previous one. For the moment, it is discarded.

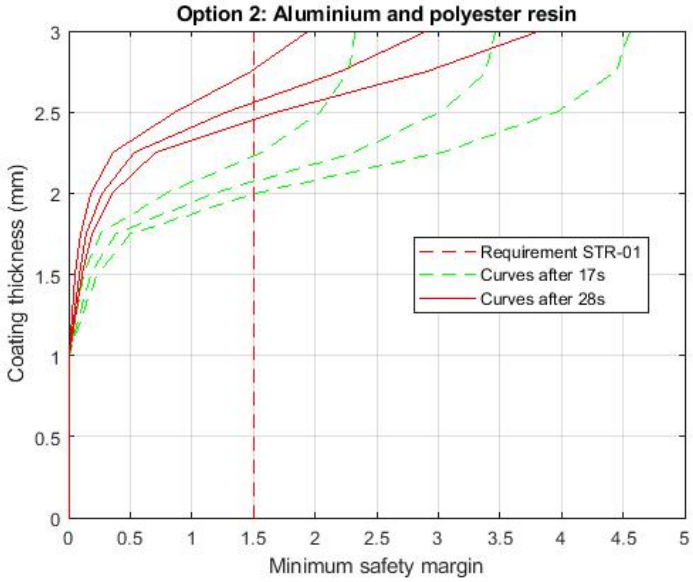

Figure 4.6: Performance results for *Option 2*.

Option 3 is very effective, as it is made from steel, and just small thicknesses of the coating are required.

Figure 4.7: Performance results for *Option 3*.

Option 4, with a polyester coating, has a worse performance than the previous one. It is also discarded.

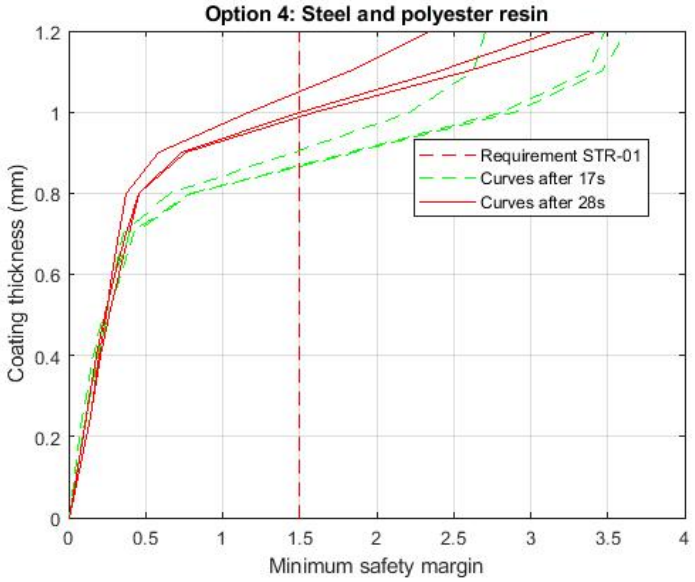

Figure 4.8: Performance results for *Option 4*.

Again, using the algorithm, for each of these four design options, we compute both the maximum temperatures and the total weight. The results are compiled in Table 5.2.

	S1 (Al+E)	S2 (Al+E)	S3 (St+E)	S4 (St+E)
t_c (mm)	1.5	1	1	0.6
t_a^{17} (mm)	1.8	2	0.7	0.8
t_a^{28} (mm)	2.2	2.4	0.8	0.95
$\zeta_{\min}^{17}$	1.62	1.73	1.61	1.51
$\zeta_{\min}^{28}$	1.63	1.61	1.66	1.59
$T^{17}c_{\max}$ (ºC)	193	157	643	573
$T^{28}c_{\max}$ (ºC)	193	164	642	560
m^{17} (g)	366	297	504	327
m^{28} (g)	393	324	511	337

Table 4.4: t_c is the thickness of the case. t_a^{17} and t_a^{28} are ablator thicknesses for a burn time of 17s and 28s, respectively. $\zeta_{\min}^{17}$ and $\zeta_{\min}^{28}$ are the minimum safety margin for a burn time of 17s and 28s, respectively. $T^{17}c_{\max}$ and $T^{28}c_{\max}$ are the maximum average temperatures achieved by the case for a burn time of 17s and 28s, respectively.

The design options that fulfil the requirement STR-02 are *S2* and *S4*; therefore, *S1* and *S3* are discarded. The difference in mass of both remaining configurations is small. *S4* would leave an internal diameter on the combustion chamber equal to 74 mm in the worst case. Meanwhile *S2*, with a thicker coating, would leave an internal diameter as small as 71.2 mm in the worst case, implying a lower filling factor. However, the thinner the layer of epoxy resin, the higher the possibilities that it is totally consumed before the burn time ends. Furthermore, it is desirable to keep the case as cool as possible, as happens with *S2*, to protect the avionics and the payload on the fairing.

However, the cost of obtaining our steel is higher than the aluminium and, therefore, our final choice for structural configuration is *S2*. As can be deduced from 5.2, a lower burn time allows to significantly reduce the thickness of the coating and, therefore, to increase the *filling factor* of the propellant. For that reason, we choose finally the functional configuration *2-4-R*, from 3.9.

4.6. Considerations for the nozzle design

The nozzle throat is where the heat transfer will be the highest in the engine; according to an estimation, it can double the amount of heat transfer inside the case (30). The pressure at the throat will be significantly high, and will probably place stresses on the material.

The nozzle could be made out of a single piece of a high-strength and high-heat-resistance material, or either we made out of the combination of several materials in several locations inside it (43). High alloy steels or other high-strength metals could be used for the nozzle, although graphite is, for the moment, a preferable option due to its lower density. In any case, metals and graphite could be used together; the first ones providing strength and stiffness, whilst the graphite would bring exceptional thermal resistance.

Due to the modelling complexity and the lack of time to work on it, we will not address the design of the nozzle any further in this document.

4.7. Combined design and rocket performance

Our combustion chamber internal diameter has been reduced to 72 mm by introducing the layer of ablative insulator. Therefore, we must adapt our engine functional configuration *2-4-R* to the new internal volume. Due to the thickness of the coating, the external diameter of the grains has to be smaller than it was described in 3.9. As a consequence, the combustion chamber has to be lengthened and the nozzle throat reduced. These changes imply that the burn time will probably increase. Therefore, we must work with the simulators that have been presented, in both this chapter and the previous one, until finding a combination of functional and structural configuration parameters that fulfil all of the functional and structural requirements. We end up finding such solution.

	L_c	d_c	d_t	d_o	L_g	d_{eg}	d_{pg}	t_c	t_a
Engine design parameters(mm)	512	76(72)	9.7	75	123	72	21	1	2

Table 4.5: L_c and d_c are the case internal length and diameter, respectively. dt and d_o are the nozzle throat and outer diameters, respectively. L_g, d_{eg} and d_{pg} are, in this order, the propellant grain length, external diameter and port diameter. Finally, t_c and t_a are the thickness of the case and the ablative insulator, respectively.

Just as a remainder, the propellant formulation in this design would be the so called RNX. It would have a mass equal to 3.22 kg, split into four identical grain segments. The mass of the case and the ablative insulator would be equal to 0.297 kg. The performance values of the engine in this design are detailed in the following table.

	F_{av}(N)	P_0 (MPa)	P_2 (kPa)	I_{sp} (s)	I_t (kN s)	ζ_{min}
Engine performances	215	2.05	2.80	124.75	3.94	1.50

Table 4.6: F_{av} is the, approximate, mean thrust developed by the engine. P_0 and P_2 are the pressure at the combustion chamber and at outlet of the nozzle, respectively. I_{sp} and It are, in this order, the specific impulse and the total impulse. Finally, ζ_{min} is the minimum structural safety margin.

Using our simulator, we plot the trajectory of the rocket, assuming a dry mass equal to 1.5 kg (Figure 4.9). The engine would burn during 18.39 s. The rocket would then achieve a maximum velocity approximately equal to 1200 m/s, at a height of 38.67 km. The rocket would get to an apogee height of 110 km after 141 s of flight. The payload inside the fairing would experience microgravity for 4.2 minutes, thus fulfilling the requirement MIS-05, until the atmospheric drag would start to slow down the rocket This would happen 4.5 minutes after ignition, at a height of 20 km.

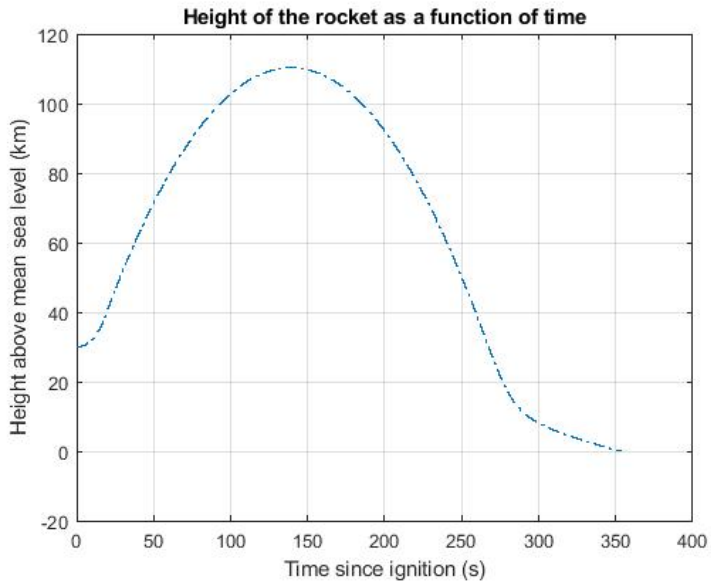

Figure 4.9: Trajectory of the rocket for the previous engine design parameters. A dry mass equal to 1.5 kg has been assumed.

CHAPTER 5. EXPERIMENT

5.1. Introduction

The experiment that is described in this chapter is based on a standardized test method (44) and a previous experiment made by a rocket experimentalist (45).

5.1.1. Context

As has been explained in previous chapters, our rocket engine case would have a relatively long burn time, thus being exposed to the hot exhaust products. The structural integrity of the case will rely on a thin layer of a polymeric, ablative material. This experiment can be thought as the first step in the actual development of the rocket engine, during which theoretical concepts and models are validated and replaced by real technological elements and tests.

5.1.2. Objectives

Five main objectives are pursued with this experiment:

1. To further validate the simulator that has been developed in the last chapter and, subsequently, the thermo-structural design.
2. To compare the relative effectiveness of the ablative materials that have been considered and to check its consistency with the results of the simulations.
3. To evaluate the workability of these these materials and to assess many variables that are difficult or impossible to address from a purely theoretical approach, such as the adherence properties, the viscosity, the applicability on a metallic surface, etc.
4. To estimate the erosion speed of the ablative materials.
5. To evaluate the reproducibility of the casing configurations; that is, our technical ability to achieve a similar performance with different specimens manufactured with the same procedure.

5.2. Experiment design

5.2.1. Concept

Four different specimen configurations will be tested:

1. A bare plate of aluminium 6061-T6.
2. A bare plate of low-carbon alloy steel AISI 1018.
3. A combination of an aluminium plate and a layer of epoxy resin.

4. A combination of an aluminium plate and a layer of polyester resin.

For each configuration, five identical specimens will be made. The thicknesses of the ablative materials will be properly measured and registered before beginning the experiment. All the specimens will be subjected to an assumed identical, controlled heating process during a short period of time, t_s. The transient temperature increase of each aluminium plate will be registered. After each specimen has been tested, the final thickness of the ablative material will be measured.

As the amount of heat transfer provided by the source will be initially unknown, the film coefficient of the convective heat transfer will have to be estimated. This will be accomplished out of the data obtained from the bare aluminium and steel plates (specimen configurations 1 and 2). From this estimated film coefficient, it will be possible to establish the experimental conditions in the thermo-structural algorithm and, therefore, to simulate the experiment with the program developed in the last chapter.

Our first objective will be achieved by comparing the experimental results of the specimen configurations 3 and 4 with the simulated results of the program, once the film coefficient has been estimated. The second goal will be accomplished by comparing the mean average performance of each specimen configuration. The third objective will be attained by qualitatively assessing the manufacturing process of the specimens. Our next goal will be achieved from the two previous thickness measurements. Our final objective will be accomplished by comparing the results of each five specimens within each configuration.

5.2.2. Components and requirements

Several functional parts are needed for this experiment. First and foremost, a controllable, steady heating source is required. A blowtorch is considered to be appropriate for this purpose. When ignited, this torch will likely have a short, transient period of flame buildup and stabilisation until achieving the desirable steady state.

This would be a source of inaccuracy of the results, so a mechanical assembly will be used for minimising these effects, as well as for fixing the specimen with respect to the heating source. The thickness of the specimens shall be similar to those considered in the previous chapter. All aluminium plates will be 1 mm thick, whilst the layers of epoxy and polyester will both have a thickness equal to 2 mm.

Devices for both measuring the thickness of the specimens and to record the transient heating of the specimens are also needed. A micrometer and a type K thermocouple will be used. That thermocouple is relatively inexpensive and has a wide temperature range: from -270°C to 1260 °C. It's accuracy will go from ± 1.1°C to ± 2.2°C, depending on the grade of the wire. The thermocouple will be attached to the rear of the specimens and connected to a data acquisition device, which will register and store the data samples at a certain rate.

A t_s equal to 10 s is chosen as it is a time, though smaller, of the same order of magnitude of the expected burn time of the engine. The data acquisition device shall have a sampling rate as low as the hardware allows in order to have a large amount of data points.

5.2.3. Assembly design

The assembly will be made out of five main functional pieces, that hereby are orderly described:

Piece number 1: Its function is to support the specimen during the test.

Piece number 2: It indicates where the torch tip must stand during the test.

Piece number 3: It physically holds the specimen against piece number 1, acting as a vice.

Piece number 4: It fixes the position of the previous pieces, acting as a support for the whole assembly.

Piece number 5: It is temporarily placed between the pieces numbers 1 and 2, blocking most of the heat during the flame buildup and stabilisation of the source. It is afterwards removed during the test.

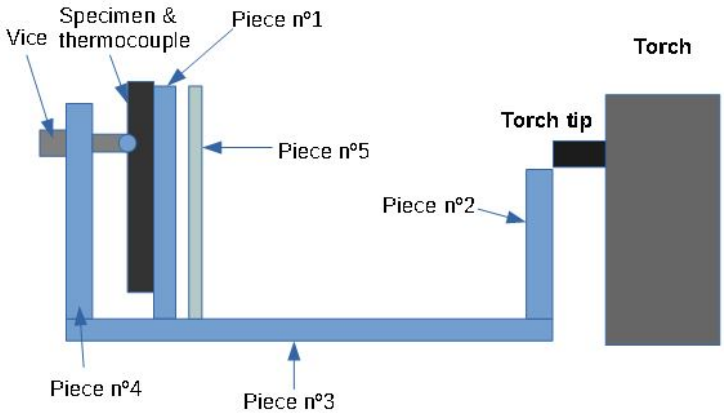

Figure 5.1: Draft of the experiment assembly. It includes both the torch, the specimen, the thermocouple and the vice for easier understanding.

5.2.4. Procedure

The experimental procedure for each specimen will follow these steps:

1. The initial thickness of the specimen is measured.
2. The specimen and the thermocouple are arranged and fixed in the assembly. Piece number 5 and the torch are positioned and the data acquisition device is turned on.
3. The torch is turned on.
4. Once the flame has stabilised, piece number 5 is removed and a chronometer starts a countdown equal to t_s.
5. Once the countdown is over, piece number 5 is positioned again and the torch is turned off.
6. Once it has cooled enough, the specimen is removed and the remaining thickness is measured.

5.2.5. Data analysis concept

The raw data acquired by the data acquisition device will be plotted into 2D graphs, showing the evolution of temperature at the back of the specimen as a function of time. As has already been mentioned, the film coefficient will have to be estimated from the data of the bare aluminium and steel plates. This will be done by solving the problem of transient heat transfer in reverse with respect to how it was done in the previous chapter. The algorithm to be used is the following:

Step 0: An initial guess of the value of the convective heat transfer coefficient, h_{g}, is defined.

Step 1.1: The temperature distribution on the specimen as a function of time is simulated for the initial guess of film coefficient.

The simulated time of heating shall be equal to the experimental one.

Step 1.2: The accuracy of the result is evaluated.

If the final temperature obtained is lower than the experimental one, the value of the convective heat transfer coefficient is increased by a certain discrete amount, Δh_{g}. On the other hand, whether the simulated final temperature is instead higher, this value is decreased.

Step 2: Steps 1.1 and 1.2 are repeated until a sufficiently accurate result is obtained.

Once h_g has been obtained, the specimen configurations 3 and 4 will be simulated using the algorithm on the previous chapter. Both the simulated and the experimental results will be compared to check their consistency.

Many causes may induce that these results diverge:

1. Our thermo-structural model and algorithm do not take into account many variables that may affect the experimental results: unsteady heating source, non-uniform thickness of the ablative materials, slight deviations in the placement and orientation of the torch, etc.
2. Our knowledge on the actual thermal properties of the materials may not be perfect.
3. The estimation of the film coefficient may be inaccurate with respect to reality.
4. In our simulations we assume that the heat flux is over all the wall, while in the experiment is just over a spot. This will cause a radial heat transfer along the wall that is not taken into account in the numerical simulations.

5.3. Preparation

5.3.1. Assembly manufacturing

An appropriate technical drawing was made for each single piece of the assembly. These drawings were then sent to the company *Criver Metàl·liques Industrials SL*. All five pieces were made out of steel, except for piece number 3, which was made with iron; they were

manufactured by laser cutting. Pieces number 1 and number 2 were joined with piece number 3 by means of both soldering and L-shaped brackets.

The propane torch that was to be used for the heating had a fixed nozzle. Measurements were made: the nozzle was elevated 160 ± 1 mm and was tilted, with an elevation angle to $8.5 \pm 1°$. Therefore, a support platform made of wood was designed and machined to make the nozzle of the torch point exactly towards the centre of the specimens. Moreover, piece number 3 was threaded in its four corners in order to be supported by threads. By changing the lengths of these threads, it was possible to easily tilt the whole assembly in almost any direction, allowing it to adjust to any torch tip inclination.

As well, an special joint was machined for piece number 2 in order to adjust its distance with respect to piece number 1.

Figure 5.2: Finished experiment assembly. All of the pieces and components, including the torch and the thermocouple, can be appreciated.

5.3.2. Specimens preparation

We decided to manufacture seven specimens of each configuration in order to have some backup for the five that were to be tested. First of all, the mass of epoxy resin that was needed was estimated. For a density equal to the value in 4.3, we needed 58 g of it. The epoxy that we used was made out of a mixture of resin and hardener with ratio 8:3. Therefore, we needed approximately 36 g of resin and 22 g of hardener. The same was repeated with polyester resin; in that case, the ratio of resin to hardener was 30:3.

We weighted the components and carefully mixed them inside two containers until achieving a homogeneous texture and colour; in both cases, the obtained fluid was a viscous and translucent mixture. The surface of the aluminium plates was roughened with sandpaper, and the resins were applied on them with a painter spatula, looking out to obtaining a uniform thickness. We experienced a problem with polyester resin: it hardened in less than 10 minutes after being mixed, thus making it difficult to apply it appropriately to all seven specimens.

After that, the specimens were stored for the curing process. The polyester took just about 40 minutes to be fully hardened, while epoxy took more than 24 hours. After curing, the polyester layers had a sticky and slightly soft constitution, and easily detached from the

aluminium plate. Meanwhile, the epoxy achieved a good bonding and was harder.

5.4. Results

The experiment was conducted on two different sessions.

5.4.1. Execution

A measurement of the temperature of the torch flame was made with a type K thermocouple and the data logger. A value between 900°C and 1000°C was found in the hottest region of the flame. A simple *manual of the experiment* was written, with the intention that it was a guideline of what had to be done to conduct the work as efficiently as possible. The manual, written in Catalan, can be reviewed at C.

The assembly was mounted in its wooden platform; its tilt was adjusted to match that of the torch tip. Then, both elements were placed inside a testing chamber. The sampling frequency of the data logger was set at its minimum value of 1 Hz, and it was connected to the thermocouple. The thermocouple was tightly held against the back of the specimen thanks to the vice. For protection, we were wearing thermal resistant gloves and a face mask. Three people had to be, at the same time, involved in the execution of the experiment for doing it efficiently: one was in charge of turning on and off the torch, another one was in charge of removing the piece numbder 5 from the assembly and, finally, someone else had to turn on the data logger and make the countdown with a chronometer.

The first few experiments were an essay for validating the experimental method and steps and getting ourselves some practice in their execution. We decided that, for all the tests, piece number 5 would be removed once the thermocouple reading achieved 60°C; that way it was ensured that all specimens possessed the same initial conditions. Once we were ready, we started recording the results.

On the first session, we tested the specimen configurations number 1 and number 2. In the second session, we tested the remaining configurations number 3 and number 4. Both the epoxy and polyester specimens burned when coming in contact with the flame. The first polyester specimen, called *P1*, started to burn before the piece number 5 was removed and, thus, its results were considered non-valid.

A handheld thermographic camera was used to record some of the tests, which allowed us to obtain some additional data, such as readings of the temperature on the front of the specimens. The images and documents generated by the thermographic camera can be found in C.

5.4.2. Data arrangement and preliminary analysis

The raw data obtained by the data logger was stored in an spreadsheet. For the first session of tests, only the data points corresponding to the first ten seconds of the heating (11 data points) were considered. A plot of temperature-time was then done for the five aluminium specimens and another one for the five steel specimens.

We soon realised that there had been an instrumental error with all the tests. The plotted curves should have been continuous, showing a, more or less, linear increase of temperature, to be followed by a decay after ten seconds. However, the curves were not continuous, but presented each a few *step data points*: two successive measurements in which the temperature was exactly the same. We speculated that this experimental anomaly was due to an error of the data logger and the chosen sampling frequency (1 Hz), which was the minimum possible value. However, we observed that, if all the *step data points* were deleted (the successive data points with identical temperatures were eliminated), the obtained curves were continuous. As well, in these cases, the eleventh sample often coincided with the peak of temperature. It seemed as if the data logger was adding non-existent data points between two real successive measurements. Therefore, we modified the plots to only show the first 11 real samples, deleting the anomalous data points. Raw data, including all points, was nonetheless securely stored for possible future uses did the necessity appear.

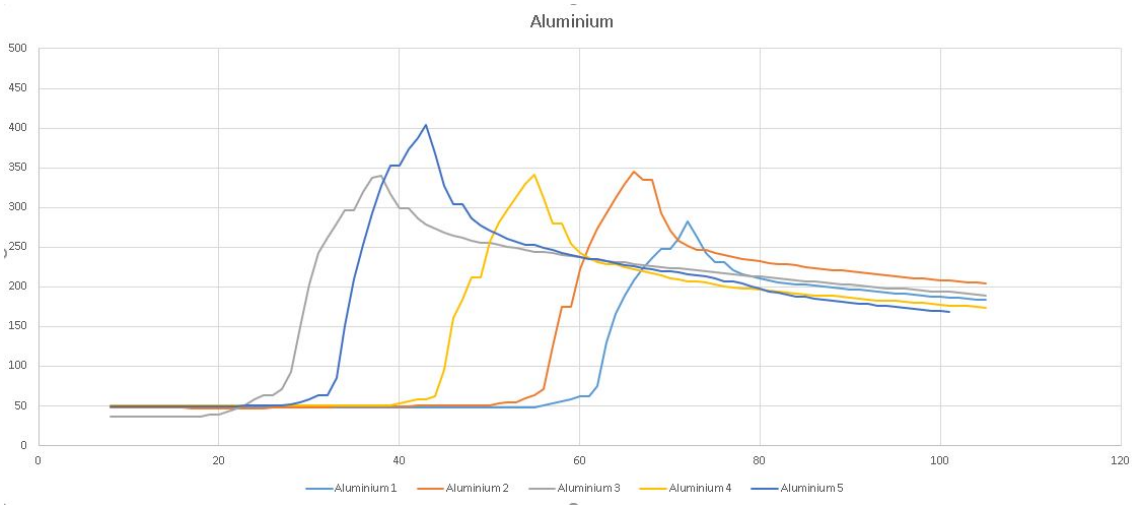

Figure 5.3: Temperature-time plots of specimen configuration number 1 obtained from the raw data; the *step data points* can be appreciated.

The aluminium specimens should have heated more than the steel ones, as our aluminium had a greater diffusivity. However, we found out that the aluminium plates had reached a temperature slightly lower than that of steel. We figured out that this could be due to the fact that, in the experimental conditions, temperature diffusion does not only occur across the thickness of the plates, but also radially across the width of the specimen; while in our simulator, heat diffusion only happened in a single space dimension.

For the specimen configurations 3 and 4, the step data points also appeared. Again, we decided to consider just the first 11 real samples.

	T_{sp_1} (°C)	T_{sp_2} (°C)	T_{sp_3} (°C)	T_{sp_4} (°C)	T_{sp_5} (°C)
Conf. n 1	281.7	345	337	341.1	403.8
Conf. n 2	353.9	352.8	245.4	431.3	452.3
Conf. n 3	152.3	134.4	122.3	96.3	90.9
Conf. n 4	94.2	79.5	83.4	197.2	138

Table 5.1: Final temperature of all the specimens after the test.

There is a significant variability of results between each five specimens with the same configuration, which indicates that the experiment conditions changed for each individual test. This can be explained by the large number of variables that were not totally controlled: the temperature of the flame, its orientation and distance to the specimen, the time duration of the test, the heat conduction from piece number 1 to the specimen, etc. In the case of the configurations 3 and 4, the ablative coating burned on contact with the flame, inevitably affecting the heat transfer.

5.4.3. Estimating the film coefficient

First of all, we made an initial guess for the film coefficient on the same order of magnitude than that expected inside the rocket engine *Casanova*: $h_g = 100$ W/m^2 K. We assumed the flame to have a temperature in the contact region with the specimen equal to $T_{flame} = 1273$ K, which was the highest measurement that we got from direct measurement of the flame.

We executed the thermo-structural program simulator by entering as inputs all the experimental conditions, including a uniform temperature distribution at 333 K (60°C) as initial condition, plus the initial guess of the film coefficient.

For the aluminium plates, the experimental average final temperature from the thermocouple was equal to 614.7 K (341.7°C). With our simulation, we obtained a value equal to 610.3 K (337.3°C), close to the experimental result. Then we iterated the value of the film coefficient until obtaining an accurate enough approximation, as has been explained in this chapter. For $h_{g,Al} = 102$ W/m^2 K, the final temperature was equal to 614.9 K; we had found the film coefficient for the aluminium plates.

For the steel plates, the same procedure was repeated. This time, we found that the corresponding film coefficient was much larger: $h_{g,St} = 203$ W/m^2 K. As has been explained before, this is likely due to the difference in diffusivity of steel and aluminium. As the specimens would be using an aluminium plate, we considered appropriate to define $h_{g,Al}$ as the film coefficient for the subsequent simulations.

5.4.4. Analysing the results

We measured the total thickness of all the specimens previous to the tests. Unfortunately, we forgot to make the measurement for one of the epoxy specimens and also for a polyester specimen. Therefore, we only had four measurements for each specimen configuration.

	$t_{sp1}(mm)$	$t_{sp2}(mm)$	$t_{sp3}(mm)$	$t_{sp4}(mm)$	$t_{sp5}(mm)$
Conf. n 3	-	0.93	1.26	1.37	1.61
Conf. n 4	1,66	1.41	1.31	1.54	-

Table 5.2: Thickness of the ablative material for each of the final specimens. Note that two of the specimens have not been measured.

We assumed the same film coefficient that we have obtained previously. We divided the thicknesses of both the coating and the metallic plate into a grid of 11 data points each. We then proceeded to re-run the simulation with the inputs for our experiments. This time, the final temperature was equal to 423.8 K (150.8°C). This value was just about 32 K off from the experimental results.

We then proceeded to make the simulation with the epoxy specimens. We introduced the corresponding coating thickness, which was the average value, and the same input data as before. This time, we expected a final temperature equal to 392.2 K from the experimental results (119.2°C); the simulation gave us a value of 413.2 K (140.2°C), just 21 K larger.

Finally, we evaluated the dependency of the final temperature achieved on the thickness of the coating. As it is obvious, we were expecting an inversely proportional relation, which would partially explain the variability of results. From the previous data, we plotted all the 4 polyester-aluminium and 4 epoxy-aluminium specimens in a final temperature-thickness plot. For the epoxy specimens, we found a pretty good regression line that was descendant and not far from the 4 points. However, the 4 points corresponding to the polyester specimens had no clear correlation. We attributed this to the fact that it was difficult to measure the real thickness of the polyester specimens due to their sticky and slightly soft properties, and to the many additional variables that affected these specimens.

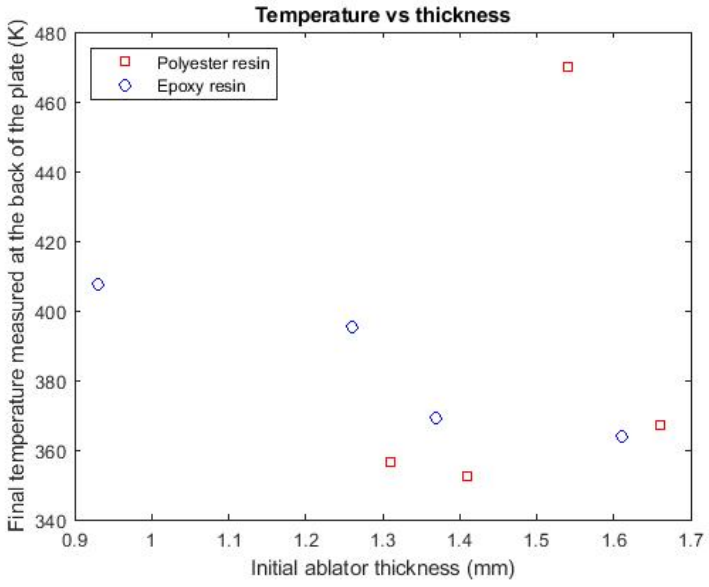

Figure 5.4: Dependency of the ablator thickness on the final temperature achieved by the plate.

CHAPTER 6. MECHANICAL PROTOTYPE

6.1. Mechanical design

Continuing with the development of the engine, we started to work on the manufacturing and assembly of a full scale prototype, including its three main engine components: the case, the bulkhead and the nozzle. These three components will be manufactured separately and joined together afterwards.

However, we must comment that this prototype is actually slightly smaller than the rocket engine that we designed at the end of 4, having an internal case diameter equal to 73 mm and a length of 395 mm. The reason is that we acquired materials long before having finished the design and, thus, we made a rough estimation of the size it should have. The bulkhead and the nozzle, meanwhile, were manufactured after finishing the design and the experiment and, thus, include several of the design parameters of the final engine design.

6.1.1. Fastening and sealing

Both the bulkhead and the nozzle will be fitted with the case tube. The mechanical joining must fulfil two requirements:

MECH-1: It must remain hermetically sealed during the combustion, preventing undesirable pressure losses on the chamber.

MECH-2: It must withstand the mechanical and thermal stresses inside the combustion chamber.

The simplest and cheapest solution for achieving MECH-1 is to use O-Rings. In order to better seal the combustion chamber and to have redundancy, we decided to use two successive Nitrile Butadiene Rubber (NBR) O-Rings for both the nozzle and the bulkhead. Their external diameter, d_1, was chosen as 68 mm, whilst their cross-sectional diameter, d_2, was defined at 2 mm. The design tables that were used in the sizing of the O-Rings can be analysed in **??**.

Regarding MECH-2, we initially considered to use a threaded fit. However, the reduced thickness of the case (1 mm) would make it impractical and we finally decided to use screws. The size and number of screws was made equal to that of a rocket engine design (46) with a larger chamber pressure than ours (8 MPa), as a worst-case estimation. We used standardised DIN7991 screws, made of steel, due to their countersunk head which, we estimated, would minimise the protruding from the case. Twelve M3 and nine M4 screws were used for fastening the nozzle and the bulkhead, respectively.

6.1.2. Component tolerances

We decided to use a clearance fit (47), meaning that the nozzle and bulkhead attachment shaft were to be slightly smaller than the case internal diameter. We chose a sliding fit to

be able to manually assemble the engine, without having to apply much force. The sliding fit had an associated tolerance coded as *H7g6*; by checking an ISO standard tolerance calculator (48), we determined a maximum and minimum clearance diameter to 59 μm and 10 μm, respectively. This allowed for a reduced machining tolerance equal to, at most, 24 μm.

Type of Fit	Description	Hole Basis	Shaft Basis
Clearance Fits	Loose Running	H11/c11	C11/h11
	Free Running	H9/d9	D9/h9
	Close Running	H8/f8	F8/h8
	Sliding	H7/g6	G7/h6
	Locational Clearance	H7/h6	-
Transition Fits	Similar	H7/k6	K7/h6
	Fixed	H7/n6	N7/h6
Interference Fits	Press	H7/p6	P7/h6
	Driving	H7/s6	S7/h6
	Forced	H7/u6	U7/h6

Figure 6.1: Standardized types of fits and associated tolerances. Source: reference (47

As we already had acquired the case tube, we measured with precision its internal diameter, obtaining a value of 73.17 mm. We sized both the nozzle and the bulkhead attachment shafts to a diameter of 73.13 mm, having a 40 μm clearance with the case. With this information, detailed technical drawings were made, which can be found at B. We sent the drawings to the machining company *PLACON SRL*.

6.2. Manufacturing the components

The aluminium tube that was to be used for the casing was manufactured by extrusion as part of a larger tube, and cut afterwards; then, the clearance holes for the screws were made. Both the nozzle and the bulkhead were bodies of revolution and so, they were manufactured in a lathe machine by the workers of *PLACON SRL*; their correspondent threaded holes were machined afterwards.

Once we had acquired all three components, we immediately tested the fitting with the case. The fit was a bit tighter than expected: a significant amount of manual force was required.

6.3. Assembling the pieces

The main challenge was to cleanly fit the nozzle and the tap with the O-Rings while avoiding to accidentally damage them. First of all, we weighted all the pieces, including the O-Rings and the screws. Then, we lubricated the bulkhead external surface with alcohol and tested the fit with the tube. However, as has been mentioned, the fit was too tight. Therefore, we decided to reduce and adjust the external diameter of both the bulkhead and the nozzle.

Figure 6.2: The three main engine components just before the assembly. The O-Rings and screws can be appreciated.

	Tube	Nozzle	Bulkhead	O-Rings(x4)	M3 screws(x12)	M4 screws(x9)
m (g)	228.1	336.6	136.8	3.4	5.4	7.8

Table 6.1: Measured masses of the prototype pieces.

Once more, the workers at *PLACON SRL* assisted us with this operation. The bulkhead was carefully placed into the chuck, the rotation started and the diameter was reduced with a turning tool. We found out that, for a reduction of 100 μm for both the bulkhead and the nozzle, the fit was perfect.

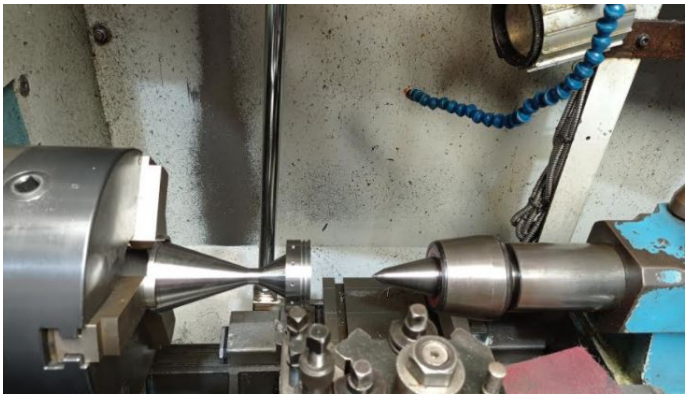

Figure 6.3: The nozzle in the lathe chuck, prior to adjusting its diameter.

Then, we greased again the bulkhead and placed the O-Rings inside their slot. Slowly and carefully, we pushed the piece manually, keeping care into not slicing the O-Rings. That time, it worked perfectly. The same operation was done by the nozzle.

Then, the fastening screws were installed, one by one. We realised that there had been a mistake with one of the threaded holes in the nozzle; it was too big for the M3 screws. We decided to try to solve this by making it wider to an M4 threaded hole, and use an M4 screw for it instead.

Figure 6.4: Final look of the rocket engine *Casanova* prototype.

Various options were considered for painting the external surface of the case. However, due to a lack of time, we were not able to do it before finishing this document.

Figure 6.5: SolidWorks model of the completed *Casanova* rocket. Source of the background: NASA.

CHAPTER 7. CONCLUSIONS

In this document, we have demonstrated the feasibility of the rocket engine powering the launch system defined in the introduction, and we have done so both theoretically and –partly– experimentally. The rocket engine has been designed; with the current design iteration, all of the mission, functional and structural requirements are met.

Our most salient conclusions are:

1. We have proven by means of simulations that a rocket launched from 30 km of height, having a total mass of about 4.8 kg and using RNX as propellant, would reach an apogee of 110 km, thus entering into space. The dimensions of the rocket and the properties of the solid propellant grain have been determined by means of numerical simulations.
2. We have simulated the heat transfer on the casing walls and determined, by means of real experiments, the behaviour of several combinations of ablative and casing materials. These experiments show that an aluminium casing of 1 mm in thickness covered with 2 mm of epoxy would fulfil the requirements for thermal protection.
3. The blueprints of the casing and nozzle have been made. A near real-scale model based on these blueprints has been built and integrated.

A detailed list of more concrete conclusions is as follows:

1. It has been determined that a cylindrical combustion chamber must be used. It shall have a length of 512mm, an internal diameter of 76 mm and a thickness of 1mm.
2. The case would be covered with a layer of epoxy resin 2 mm thick. The combined case and ablative coating would have a mass of approximately 0.3 kg.
3. The propellant formulation *RNX* would be used.
4. The propellant would be processed and casted into four solid segments, each having a length of 123 mm, an external diameter equal to 72 mm and an internal port diameter of 21 mm. Both their external and internal (port) surfaces would be inhibited, while their end surfaces would burn. We have called this grain configuration *bypass*. The total amount of propellant would weigh 3.22 kg.
5. The nozzle would be conical; with a convergence and divergence diameters equal to 30^o and 18^o, respectively. It would have a throat and outlet diameters equal to 9.7 and 75 mm, respectively.
6. The engine would develop, at a height of 30 km, an almost steady thrust of 215 N during 18 s, meaning a total impulse equal to 3.94 kN s. Its specific impulse would be around 125 s. The internal chamber pressure would be equal to 2.05 MPa; the nozzle would expand the exhaust products until a pressure of 2.8 KPa.
7. Such an engine would be able to provide a Delta-V of 1.2 km/s to a rocket with a dry mass of 1.5 kg (including case, nozzle, bulkhead, fairing, avionics and a 0.3 kg payload) launching from a platform at a height of 30 km.
8. The rocket would provide 4.2 minutes of micro-gravity to the payload.

9. In order to achieve these results, several models and algorithms have been used to build simulation programs in Matlab. Specifically, we have developed, validated and used for design purposes: a rocket engine performance and trajectory simulator, including an atmospheric model and a transient heat transfer and mechanical stresses simulator.

As well, experiments on the thermo-structural design yield the following conclusions:

1. The thermo-structural simulator has been validated, as the experimental and simulated results were similar and consistent.
2. It was experimentally proved that both epoxy and polyester resin have a similar thermal performance.
3. The epoxy resin was a much better option as compared to polyester due to a better workability, adherence properties and a tougher and more resistant constitution. Therefore, we have chosen it as thermal protection of the casing.
4. Unfortunately, it was not possible to estimate the erosion speed of the ablative materials due to not having the appropriate measurement tools.
5. There was a large variability in the experimental results due, in part, to thickness differences. The average of each specimen configuration was similar to the simulated results.

There is still a large amount of work to be done beyond what has been presented here. Specifically:

1. Perform a proper analysis and design of the nozzle.
2. Analyse and design the ignition system of the engine.
3. Make additional and improved thermal tests building off from the conclusions of the experiment. Increase the number of specimens, try to combine epoxy with a hardener, address the anomaly of the *step data points*, use more appropriate instrumentation, etc.
4. Engineer an appropriate method for applying the epoxy upon aluminium with a uniform thickness.
5. Design and build a prototype engine for conducting static tests.
6. Research and determine the legal protocols to be followed for conducting a static test.

BIBLIOGRAPHY

[1] George P. Sutton Oscar Biblarz. *Rocket Propulsion Elements, 9th Edition, p. '76'*. 2017.

[2] Capt. Bertrand R. Brinley. *Rocket Manual for Amateurs, p. '71'*. 1960.

[3] R. Nakka. Potassium Nitrate/Sucrose Propellant (KNSU). URL: http://www.nakka-rocketry.net/sucrose.html.

[4] R. Nakka. KNSB Propellant. URL: http://www.nakka-rocketry.net/sorb.html.

[5] R. Nakka. Kappa-DX rocket motor Static Test KDX-002 Test Report. URL: http://www.nakka-rocketry.net/kdx002f.html.

[6] R. Nakka. KN - Dextrose (KNDX) Propellant. URL: http://www.nakka-rocketry.net/dex.html.

[7] R. Nakka. RNX Composite Propellant. URL: http://www.nakka-rocketry.net/rnx_int.html.

[8] D. Claude. Development of a Metalized Ammonium Nitrate-based Propellant. URL: http://www.nakka-rocketry.net/anprop.html.

[9] R. Nakka. Experiments with Ammonium Nitrate / Aluminum based Propellant Formulations. URL: http://www.nakka-rocketry.net/anexp.html.

[10] George P. Sutton Oscar Biblarz. *Rocket Propulsion Elements, 9th Edition, p. '515'*. 2017.

[11] NASA. U.s. standard atmosphere, 1976. 1976.

[12] Oscar Biblarz George P. Sutton. *Rocket Propulsion Elements, 9th Edition, p. '45'*. 2017.

[13] George P. Sutton Oscar Biblarz. *Rocket Propulsion Elements, 9th Edition, Section 3.5. Real Nozzles*. 2017.

[14] R. Nakka. Solid Rocket Motor Theory – Corrections for Actual Rocket Motors. URL: http://www.nakka-rocketry.net/th_corr.html.

[15] George P. Sutton Oscar Biblarz. *Rocket Propulsion Elements, 9th Edition, p. '59'*. 2017.

[16] George P. Sutton Oscar Biblarz. *Rocket Propulsion Elements, 9th Edition, p. '57'*. 2017.

[17] George P. Sutton Oscar Biblarz. *Rocket Propulsion Elements, 9th Edition, p. '52'*. 2017.

[18] George P. Sutton Oscar Biblarz. *Rocket Propulsion Elements, 9th Edition, Section 14.3. Extinction or Thrust Termination*. 2017.

[19] Arnon Lesage. Solid propellant grain geometry, a model for the evolution of star shaped interfaces. 2010.

[20] George P. Sutton Oscar Biblarz. *Rocket Propulsion Elements, 9th Edition, p. '453'*. 2017.

[21] George P. Sutton Oscar Biblarz. *Rocket Propulsion Elements, 9th Edition, p. '453'*. 2017.

[22] Alireza Mostofizadeh Saeed Mesgari, Mehrdad Bazazzadeh. Finocyl grain design using the genetic algorithm in combination with adaptive basis function construction. 2018.

[23] George P. Sutton Oscar Biblarz. *Rocket Propulsion Elements, 9th Edition, p. '558'*. 2017.

[24] Miltiades Elliotis. A finite element approach for the elastic-plastic behavior of a steel pipe used to transport natural gas. 2013.

[25] George P. Sutton Oscar Biblarz. *Rocket Propulsion Elements, 9th Edition, p. '298'*. 2017.

[26] George P. Sutton Oscar Biblarz. *Rocket Propulsion Elements, 9th Edition, p. '297'*. 2017.

[27] Zulhanif H. Supriadi M. Salimor M. Badaruddin, H. Wardono. Experimental investigation of mechanical properties of cold-drawn aisi 1018 steel at high-temperature steady-state conditions, j. mater. res. technol., vol. 9, no. 2, pp. '1893-1904'. 2013.

[28] Matweb. Aluminum 6061-T6; 6061-T651. URL: http://www.matweb.com/search/datasheet_print.aspx?matguid=1b8c06d0ca7c456694c7777d9e10be5b.

[29] Pawel Ocron Jan Taler. Finite element method in steady-state and transient heat conduction. 2013.

[30] George P. Sutton Oscar Biblarz. *Rocket Propulsion Elements, 9th Edition, p. '288'*. 2017.

[31] Juan Pedro Mellado. Lecture Series in Numerical Methods: Finite Difference Methods for Partial Differential Equations.

[32] Theodore Baumeister III Eugene A. Avallone. *Marks' Standard Handbook for Mechanical Engineers, Tenth Edition, Section 4.4 Transmission of Heat by Conduction and Convection*. 1996.

[33] R. Nakka. Technical Notepad 4 – Convective Heat Transfer Coefficient Calculation. URL: http://www.nakka-rocketry.net/techs3.html.

[34] George P. Sutton Oscar Biblarz. *Rocket Propulsion Elements, 9th Edition, Section 15.1 Rocket Motor Case*. 2017.

[35] Encyclopedia Britannica. Types of Steel. URL: https://www.britannica.com/technology/steel/Testing-of-properties.

[36] David G. Rethwisch William D. Callister, Jr. *Materials Science and Engineering: An Introduction, 8th Edition, Section 11.2 Ferrous Alloys*. 2010.

[37] David G. Rethwisch William D. Callister, Jr. *Materials Science and Engineering: An Introduction, 8th Edition, Section 8.4 Brittle Fracture*. 2010.

[38] Matweb. AISI 1018 Steel, cold drawn. URL: http://www.matweb.com/search/datasheet_print.aspx?matguid=3a9cc570fbb24d119f08db22a53e2421.

[39] George P. Sutton Oscar Biblarz. *"Rocket Propulsion Elements", 9th Edition, p. '312'*. 2017.

[40] J. Maria; Torre L. Natali, M; Kenny. "science and technology of polymeric ablative materials for thermal protection systems and propulsion devices: a review", progress in materials science, vol. 84, pp. '192-275'. 2016.

[41] George P. Sutton Oscar Biblarz. *"Rocket Propulsion Elements", 9th Edition, p. '292'*. 2017.

[42] R Nakka. Thermal Ablative Experimentation. URL: http://www.nakka-rocketry.net/ablatex1.html.

[43] George P. Sutton Oscar Biblarz. *"Rocket Propulsion Elements", 9th Edition, Section 15.2. Nozzles*. 2017.

[44] ASTM International. Standard Test Method for Oxyacetylene Ablation Testing of Thermal Insulation Materials.

[45] R. Nakka. Thermal Ablative Experimentation. URL: http://www.nakka-rocketry.net/ablatex1.html.

[46] R. Nakka. Kappa Solid Rocket Motor. URL: http://www.nakka-rocketry.net/kappa.html.

[47] Andreas Velling. Limits Fits. URL: https://fractory.com/limits-and-fits/.

[48] Amesweb Advanced Mechanical Engineering Solutions. LIMITS, FITS AND TOLERANCES CALCULATOR (ISO SYSTEM). URL: https://amesweb.info/fits-tolerances/tolerance-calculator.aspx.

APPENDICES

APPENDIX A. CODE

Here can be reviewed the code for the two main Matlab programs that have been developed in this work: the rocket engine performance and trajectory simulator and the transient heat transfer and mechanical stresses simulator.

A.1. Chapter 3: Ideal Rocket Trajectory.m

```
% close all
% clear all
% clc
% format long;
% %% Ideal rocket trajectory -- Coma Busquets, Aleix

% %% Step 0 - Initial conditions, design & simulation parameters
& %%constants are established
% % Constants
% R_prima = 8.3143; % Constant universal dels gasos. J/(kg*mol*K)
% g_0 = 9.80665; % Acceleració de la gravetat a la superfície de la Terra [m/s^2]
% r_air = 287.15; % Constant de gas per a l'aire [m^2/(s^2*K)]
% gamma = 1.4; % Ratio de les calors específiques de l'aire.
% % Simulation parameters
% delta_x = 1*10^(-6); % Mida del gruix cremat a cada iteració. m
% delta_P_2 = 100; % Variable que farem servir per aproximar el
% valor de la pressió a la sortida de la tobera, P2.
% delta_t_decay = 0.01; % Mida dels 'time steps' durant el pas 2.2
% de l'algoritme [s]
% delta_t_trajectory = 0.01; % Mida dels 'time steps' durant el
% pas 3 de l'algoritme [s]
% % Design parameters
% m_dry = 1.5; % Massa en sec del coet: massa en sec del motor +
% massa del carenat (fairing) [kg]
% D = 78*10^(-3); % Diàmetre de la secció normal del coet. Gruix
% de les parets d'1 mm [m]
% A = D^2/4*pi; % Àrea de la secció normal del coet [m^2]
% C_d = 0.4; % Coeficient de fregament aerodinàmic
% h_0 = 30000; % Alçada inicial [m] Ha de ser més gran de '0'
% Vel_0 = 0; % Velocitat inicial [m/s]
% chamber = [512*10^(-3),72*10^(-3)]; % chamber(1): Longitud de la
% cambra, suposant que és un cilindre simple. m
%                                     % chamber(2): Diàmetre
% interior de la cambra. m
% nozzle = [9.7*10^(-3),75*10^(-3),30,18]; % nozzle(1): Diàmetre
% de la gola. m
%                                           % nozzle(2): Diàmetre
% de la sortida. m
%                                           % nozzle(3):
```

```
% Convergència. º
%                                          % nozzle(4):
% Divergència. º
% propellant_id = 3; % 1: KNSB; 2: KNDX; 3: RNX
% [T_c,rho,k,M,c_star] =
% get_propellant_properties(propellant_id); % Temperatura de
% combustió, densitat del gra de propel·lent, etc.
% sizes = [4,123*10^(-3),72*10^(-3),21*10^(-3),0]; % sizes(1): Nº
% de segments.
%                                          % sizes(2): Longitud
% dels segments. Assumim que són tots iguals. m
%                                          % sizes(3): 1er
% diàmetre: diàmetre exterior dels segments. m
%                                          % sizes(4): 2on
% diàmetre. Si no s'escau, posar '0'. m
%                                          % sizes(5): 3er
% diàmetre. Si no s'escau, posar '0'. m
% surfaces = [0,1,1,0,0]; % surfaces(1): Superfície externa. '1'
% si crema; '0' si està inhibida.
%                          % surfaces(2): 1er 'end'.
%                          % surfaces(3): 2on 'end'.
%                          % surfaces(4): 1era superfície interior,
% si s'escau.
%                          % surfaces(5): 2ona superfície interior,
% si s'escau.
% area_ratio = nozzle(1)^2/nozzle(2)^2; % Proporció de l'àrea de
% la gola i de la tobera i de la sortida.
% % Correction factors
% lambda = 0.5*(1+cos(nozzle(4)*pi/180)); % Factor de correcció de
% la quantitat de moviment a la sortida de la tovera.
% 0.5*(1+cos(nozzle(4)*pi/180))
% discharge = 0.90; % Factor de correcció del flux màssic a través
% de la tovera.
% b_layer = 0.99; % Factor de correcció per les de velocitat a la
% sortida de la tovera per la capa límit del flux.
% eta_noz = 1; % Factor de correcció arbitrari per les pèrdues
% diverses de la tovera.
% % Initial conditions
% [T_atm_0,P_atm_0,rho_atm_0] = get_atmospheric_properties(h_0);
% Obtenim les propietats atmosfèriques a l'alçada inicial
% T_0_0 = T_atm_0; % [K]
% P_0_0 = P_atm_0; % [Pa]
% v_0_0 = 1/rho_atm_0; % Volum específic de gas (aire) abans de
% l'inici de la combustió [m^3/kg]
% V_free_0 = pi/4*chamber(2)^2*chamber(1) - pi/4*(sizes(3)^2 -
% sizes(4)^2 + sizes(5)^2)*sizes(2)*sizes(1); % Volum lliure
% inicial a la cambra de combustió (volum de la cambra - volum
% inicial del gra de propel·lent
```

```
% m_prop_0 = pi/4*(sizes(3)^2 - sizes(4)^2 +
% sizes(5)^2)*sizes(2)*sizes(1)*rho; % Massa de propel·lent
% inicial
% m_total_0 = m_dry + m_prop_0; % Massa total del coet (massa en
% sec + massa del propel·lent) [kg]
% F_g_0 = m_total_0*g_0; % Força gravitatòria que actua
% inicialment sobre el coet [kg*m/s^2=N]
% b_0 = C_d*A*rho_atm_0/2; % Factor multiplicatiu inicial del
% fregament aerodinàmic [kg/m]
% if(Vel_0>=0)
%     F_d_0 = -b_0*Vel_0^2; % Força de fregament aerodinàmic
% inicial
% else
%     F_d_0 = b_0*Vel_0^2; % Força de fregament aerodinàmic
% inicial
% end
% acc_0 = (F_d_0+F_g_0)/m_total_0; % Acceleració inicial. No hi ha
% thrust [m/s^2]
% % Obtenció i organització de dades
% I_int = 0; % Variable que ens servirà per calcular l'Impuls
% Total i l'Impuls Específic del motor.
% [a,n] = get_burn_properties(propellant_id,P_0_0); % Coeficient i
% exponent de pressió del propel·lent
% [size] = get_size_vectors(sizes,surfaces,delta_x); % Nombre de
% passos de simulació que haurem de fer fins que s'esgoti el
% propel·lent
% T_0 = zeros(1,int32(size)); % Vector de temperatures a dins la
% cambra de combustió [K]
% P_0 = zeros(1,int32(size)); % Vector de pressions a dins la
% cambra de combustió [Pa]
% v_0 = zeros(1,int32(size)); % Vector de volums específics a dins
% la cambra de combustió [m^3/kg]
% V_free = zeros(1,int32(size)); % Vector de volums lliures a dins
% la cambra de combustió [m^3]
% m_prop = zeros(1,int32(size)); % Vector de massa de propel·lent
% restant [kg]
% m_total = zeros(1,int32(size)); % Vector de massa total del coet
% [kg]
% m_dot_in = zeros(1,int32(size)); % Vector de flux màssic que es
% genera de gasos de combustió [kg/s]
% m_dot_out = zeros(1,int32(size)); % Vector de flux màssic que
% s'evacua per la tovera de gasos de combustió [kg/s]
% m_dot_diff = zeros(1,int32(size)); % Vector de diferència de
% fluxos màssics [kg/s]
% m_exhaust = zeros(1,int32(size)); % Vector de massa de gasos de
% combustió que hi ha a dins la cambra de combustió [kg]
% P_2 = zeros(1,int32(size)); % Vector de pressió a la sortida de
% la tovera, després de l'expansió [Pa]
```

```
% Vel_2 = zeros(1,int32(size)); % Vector de velocitat dels gasos
% de combustió a la tovera, després de l'expansió [m/s]
% F = zeros(1,int32(size)); % Vector de l'impuls del motor [N]
% t = zeros(1,int32(size)); % Vector de temps transcorregut d'ençà
% de l'inici de la combustió [s]
% T_atm = zeros(1,int32(size)); % Vector de la temperatura de
% l'aire atmosfèric [K]
% P_atm = zeros(1,int32(size)); % Vector de la pressió de l'aire
% atmosfèric [Pa]
% rho_atm = zeros(1,int32(size)); % Vector de la densitat de
% l'aire atmosfèric [kg/m^3]
% h = zeros(1,int32(size)); % Vector de l'alçada del coet [m]
% vel = zeros(1,int32(size)); % Vector de la velocitat del coet
% [m/s]
% mach = zeros(1,int32(size)); % Vector del nombre de Mach del
% coet
% q = zeros(1,int32(size)); % Vector de la pressió dinàmica que
% experimenta el coet
% acc = zeros(1,int32(size)); % Vector de l'acceleració del coet
% F_d = zeros(1,int32(size)); % Vector de la força de fregament
% aerodinàmic que actua sobre el coet [N]
% F_g = zeros(1,int32(size)); % Vector de la força gravitatòria
% que actua sobre el coet [N]
% T_0(1,1) = T_0_0;
% P_0(1,1) = P_0_0;
% v_0(1,1) = v_0_0;
% V_free(1,1) = V_free_0;
% m_prop(1,1) = m_prop_0;
% m_total(1,1) = m_total_0;
% m_dot_in(1,1) = 0;
% m_dot_out(1,1) = 0;
% m_dot_diff(1,1) = m_dot_in(1,1) - m_dot_out(1,1);
% m_exhaust(1,1) = 0;
% P_2(1,1) = P_0_0;
% Vel_2(1,1) = 0;
% F(1,1) = 0;
% t(1,1) = 0;
% I_int = I_int + F(1,1)*t(1,1);
% T_atm(1,1) = T_atm_0;
% P_atm(1,1) = P_atm_0;
% rho_atm(1,1) = rho_atm_0;
% h(1,1) = h_0;
% vel(1,1) = Vel_0;
% mach(1,1) = vel(1,1)/sqrt(gamma*r_air*T_atm(1,1));
% q(1,1) = rho_atm(1,1)*vel(1,1)^2/2;
% acc(1,1) = acc_0;
% F_d(1,1) = F_d_0;
% F_g(1,1) = F_g_0;
```

```
% %% Step 1.1 - Execute first step of combustion
% %
% r = zeros(1,int32(size)); % Vector de la velocitat de crema del
% propel·lent, determinada segons una Llei de Potència
% r(1,1) = (a*(P_0(1,1)*10^(-6))^n)*10^(-3);
% %
% sizes(2) = sizes(2) - (surfaces(2)+surfaces(3))*delta_x;
% Actualització de les
% sizes(3) = sizes(3) - 2*surfaces(1)*delta_x; % mides dels grans
% de propel·lent
% sizes(4) = sizes(4) + 2*surfaces(4)*delta_x; % després del
% primer pas de combustió [m]
% sizes(5) = sizes(5) - 2*surfaces(5)*delta_x;
% V_free(1,2) = pi/4*chamber(2)^2*chamber(1) - pi/4*(sizes(3)^2 -
% sizes(4)^2 + sizes(5)^2)*sizes(2)*sizes(1); % Actualització del
% volum lliure a la cambra de combustió [m^3]
% m_prop(1,2) = pi/4*(sizes(3)^2 - sizes(4)^2 +
% sizes(5)^2)*sizes(2)*sizes(1)*rho; % Actualització de la massa
% de propel·lent restant [kg]
% m_total(1,2) = m_dry + m_prop(1,2); % Actualització de la massa
% total del coet [kg]
% delta_m = m_prop(1,1) - m_prop(1,2); % Massa de propel·lent
% cremada en el primer pas de combustió [kg]
% delta_t = delta_x/r(1,1); % Temps transcorregut durant el primer
% pas de combustió [s]
% t(1,2) = t(1,1) + delta_t; % Actualització del vector temps [s]
% %
% m_dot_in(1,2) = delta_m/delta_t; % Actualització del flux màssic
% de gasos de combustió que es formen [kg/s]
% %
% m_dot_out(1,2) =
% pi/4*nozzle(1)^2*(R_prima/M*T_0(1,1))^(-0.5)*k^(0.5)*(2/(k+1))^
% (k+1)/(2*(k-1)))*(P_0(1,1)-P_0_0)*discharge; % Actualització del
% flux màssic de gasos de combustió que s'evacuen [kg/s]
% m_dot_diff(1,2) =
%m_dot_in(1,2) - m_dot_out(1,2);
% Actualització de la diferència de fluxos màssics [kg/s]
% %
% m_exhaust(1,2) = m_exhaust(1,1) + (m_dot_in(1,2) -
% m_dot_out(1,2))*delta_t; % Actualització de la massa de gasos de
% combustió a dins la cambra [kg]
% v_0(1,2) = V_free(1,2)/m_exhaust(1,2); % Actualització de volum
% específic a dins la cambra [m^3/kg]
% T_0(1,2) = T_c; % Actualització de temperatura a dins la cambra
%[K]
% P_0(1,2) = (R_prima/M)*T_0(1,2)/v_0(1,2); % Actualització de
% pressió a dins la cambra [Pa]
% %
```

```
% P_2_guess = 0; % Estimació inicial de pressió a la sortida de la
% tovera, assumint una expansió infinita [Pa]
% P_2_expression =
% ((k+1)/2)^(1/(k-1))*(P_2_guess/P_0(1,2))^(1/k)*sqrt((k+1)/(k-1)*
% (1-(P_2_guess/P_0(1,2))^((k-1)/k)));
% while(area_ratio>P_2_expression) % Bucle iteratiu per a
% aproximar la pressió dels gasos a la sortida de la tovera
%     P_2_guess = P_2_guess + delta_P_2;
%     P_2_expression =
% ((k+1)/2)^(1/(k-1))*(P_2_guess/P_0(1,2))^(1/k)*sqrt((k+1)/(k-1)*
% (1-(P_2_guess/P_0(1,2))^((k-1)/k)));
% end
% P_2(1,2) = P_2_guess; % Actualització de la pressió dels gasos
% de combustió a la sortida de la tovera [Pa]
% Vel_2(1,2) = sqrt((2*k/(k-1))*(R_prima/M)*T_0(1,2)*(1-(P_2(1,2)/
% P_0(1,2))^((k-1)/2)))*lambda*b_layer; % Actualització de la
% velocitat dels gasos a la sortida de la tovera [m/s]
% F(1,2) = (m_dot_out(1,2)*Vel_2(1,2) +
% (P_2(1,2)-P_atm(1,1))*pi/4*nozzle(2)^2)*eta_noz; % Actualització
% de l'impuls del motor [N]
% I_int = I_int + F(1,2)*(t(1,2)-t(1,1));
% %% Step 1.2 - Execute first step of trajectory

% F_g(1,2) = m_total(1,2)*g_0; % Actualització de la força
% gravitatòria que actua sobre el coet [N]
% acc(1,2) = (F(1,2) + F_d(1,1) - F_g(1,2))/m_total(1,2);
% Actualització de l'acceleració del coet [m/s^2]
% vel(1,2) = vel(1,1) + acc(1,2)*(t(1,2)-t(1,1)); % Actualització
% de la velocitat del coet [m/s]
% mach(1,2) = vel(1,2)/sqrt(gamma*r_air*T_atm(1,2));
% Actualització del nombre de Mach del coet
% q(1,2) = rho_atm(1,1)*vel(1,2)^2/2; % Actualització de la
% pressió dinàmica del coet [Pa]
% height = h(1,1) + vel(1,1)*(t(1,2)-t(1,1)) +
% acc(1,2)*(t(1,2)-t(1,1))^2; % Actualització de l'alçada del coet
% [m]
% if(height>=0) % Condicional per tal que l'alçada no sigui menor
% de 0
%     h(1,2) = height;
% else
%     h(1,2) = 0;
% end
% %
% [T_atm(1,2),P_atm(1,2),rho_atm(1,2)] =
% get_atmospheric_properties(h_0); % Actualització de les
% propietats atmosfèriques
% b(1,2) = C_d*A*rho_atm(1,2)/2; % Actualització del factor
% multiplicatiu del fregament aerodinàmic
```

```
% if(vel(1,2)>=0) % Condicional per establir el 'signe' del
% fregament aerodinàmic en funció de la direcció del coet (pujant
% o baixant)
%     F_d(1,2) = -b(1,2)*vel(1,2)^2; % Actualització del fregament
% aerodinàmic [N]
% else
%     F_d(1,2) = b(1,2)*vel(1,2)^2;
% end

% %% Step 2.1 - Computation until the propellant is exhausted

% c = 3; % Comptador que anirem augmentant fins a haver cremat tot
% el propel·lent
% while(m_prop(1,c-1)>0)
%     [a,n] = get_burn_properties(propellant_id,P_0(1,c-1));
%     r(1,c-1) = (a*(P_0(1,c-1)*10^(-6))^n)*10^(-3);
%     %
%     sizes(2) = sizes(2) - (surfaces(2)+surfaces(3))*delta_x;
%     sizes(3) = sizes(3) - 2*surfaces(1)*delta_x;
%     sizes(4) = sizes(4) + 2*surfaces(4)*delta_x;
%     sizes(5) = sizes(5) - 2*surfaces(5)*delta_x;
%     %
%     V_free(1,c) = pi/4*chamber(2)^2*chamber(1) -
% pi/4*(sizes(3)^2 - sizes(4)^2 + sizes(5)^2)*sizes(2)*sizes(1);
%     m_prop(1,c) = pi/4*(sizes(3)^2 - sizes(4)^2 +
% sizes(5)^2)*sizes(2)*sizes(1)*rho;
%     m_total(1,c) = m_prop(1,c) + m_dry;
%     delta_m = m_prop(1,c-1) - m_prop(1,c);
%     delta_t = delta_x/r(1,c-1);
%     t(1,c) = t(1,c-1) + delta_t;
%     %
%     m_dot_in(1,c) = delta_m/delta_t;
%     %
%     m_dot_out(1,c) =
% pi/4*nozzle(1)^2*(R_prima/M*T_0(1,c-1))^(-0.5)*k^(0.5)*(2/(k+1))
% ^((k+1)/(2*(k-1)))*(P_0(1,c-1)-P_atm(1,c-1))*discharge;
%     m_dot_diff(1,c) = m_dot_in(1,c) - m_dot_out(1,c);
%     %
%     m_exhaust(1,c) = m_exhaust(1,c-1) + (m_dot_in(1,c) -
% m_dot_out(1,c))*delta_t;
%     v_0(1,c) = V_free(1,c)/m_exhaust(1,c);
%     T_0(1,c) = T_c;
%     P_0(1,c) = (R_prima/M)*T_0(1,c)/v_0(1,c);
%     %
%     P_2_guess = 0;
%     P_2_expression =
% ((k+1)/2)^(1/(k-1))*(P_2_guess/P_0(1,c))^(1/k)*sqrt((k+1)/(k-1)*
% (1-(P_2_guess/P_0(1,c))^((k-1)/k)));
```

```
%     while(area_ratio>P_2_expression)
%         P_2_guess = P_2_guess + delta_P_2;
%         P_2_expression =
% ((k+1)/2)^(1/(k-1))*(P_2_guess/P_0(1,c))^(1/k)*sqrt((k+1)/(k-1)*
% (1-(P_2_guess/P_0(1,c))^((k-1)/k)));
%   end
%     P_2(1,c) = P_2_guess;
%     Vel_2(1,c) =
% sqrt((2*k/(k-1))*(R_prima/M)*T_0(1,c)*(1-(P_2(1,c)/P_0(1,c))^
%((k -1)/2)))*lambda*b_layer;
%     F(1,c) = (m_dot_out(1,c)*Vel_2(1,c) +
% (P_2(1,c)-P_atm(1,c-1))*pi/4*nozzle(2)^2)*eta_noz;
%     I_int = I_int + F(1,c)*(t(1,c)-t(1,c-1));
%     % %
%     F_g(1,c) = m_total(1,c)*g_0;
%     acc(1,c) = (F(1,c) + F_d(1,c-1) - F_g(1,c))/m_total(1,c);
%     vel(1,c) = vel(1,c-1) + acc(1,c)*(t(1,c)-t(1,c-1));
%     mach(1,c) = vel(1,c)/sqrt(gamma*r_air*T_atm(1,c-1));
%     q(1,c) = rho_atm(1,c-1)*vel(1,c)^2/2;
%     height = h(1,c-1) + vel(1,c-1)*(t(1,c)-t(1,c-1)) +
% acc(1,c)*(t(1,c)-t(1,c-1))^2;
%     if(height>=0)
%         h(1,c) = height;
%     else
%         h(1,c) = 0;
%     end
%     %
%     [T_atm(1,c),P_atm(1,c),rho_atm(1,c)] =
% get_atmospheric_properties(h(1,c));
%     b(1,c) = C_d*A*rho_atm(1,c)/2;
%     if(vel(1,c)>=0)
%         F_d(1,c) = -b(1,c)*vel(1,c)^2;
%     else
%         F_d(1,c) = b(1,c)*vel(1,c)^2;
%     end

%     c=c+1;
% end

% %% Step 2.2 - Computation until no thrust
% % Un cop ja hem cremat tot el propel·lent, encara queden gasos
% de combustió
% % a dins la cambra i, durant uns instants, encara produeix un
% cert impuls.
% % Per simplificar, considerem que la pressió a la cambra es
% redueix de
% % manera exponencial durant aquest període transitori.
```

```
% A_t = pi/4*nozzle(1)^2; % Àrea de la gola de la tovera [m^2]
% V_c = pi/4*chamber(2)^2*chamber(1); % Volum interior de la
% cambra de combustió [m^3]
% Const = -R_prima/M*T_c*A_t/(V_c*c_star); % Factor que determina
% la velocitat de reducció de pressió a dins la cambra
% while(P_0(1,c-1)>P_atm(1,c-1))
%     m_total(1,c) = m_dry;
%     %
%     t(c) = t(c-1) + delta_t_decay;
%     m_dot_out(1,c) =
% pi/4*nozzle(1)^2*(R_prima/M*T_0(1,c-1))^(-0.5)*k^(0.5)*(2/(k+1))
% ^((k+1)/(2*(k-1)))*(P_0(1,c-1)-P_atm(1,c-1))*discharge;
%     T_0(c) = T_c;
%     P_0(c) = P_0(int32(size)+1)*exp(Const*(t(c)-t(int32(size)+1)
% )); % Actualització de la pressió a la cambra [Pa]
%     P_2_guess = 0;
%     P_2_expression =
% ((k+1)/2)^(1/(k-1))*(P_2_guess/P_0(1,c))^(1/k)*sqrt((k+1)/(k-1)*
% (1-(P_2_guess/P_0(1,c))^((k-1)/k)));
%     while(area_ratio>P_2_expression)
%         P_2_guess = P_2_guess + delta_P_2;
%         P_2_expression =
% ((k+1)/2)^(1/(k-1))*(P_2_guess/P_0(1,c))^(1/k)*sqrt((k+1)/(k-1)*
% (1-(P_2_guess/P_0(1,c))^((k-1)/k)));
%     end
%     P_2(1,c) = P_2_guess;
%     Vel_2(1,c) =
% sqrt((2*k/(k-1))*(R_prima/M)*T_0(1,c)*(1-(P_2(1,c)/P_0(1,c))^((k
% -1)/2)))*lambda*b_layer;
%     F(1,c) = (m_dot_out(1,c)*Vel_2(1,c) +
% (P_2(1,c)-P_atm(1,c-1))*pi/4*nozzle(2)^2)*eta_noz;
%     I_int = I_int + F(1,c)*(t(1,c)-t(1,c-1));
%     % %
%     F_g(1,c) = m_total(1,c)*g_0;
%     acc(1,c) = (F(1,c) + F_d(1,c-1) - F_g(1,c))/m_total(1,c);
%     vel(1,c) = vel(1,c-1) + acc(1,c)*(t(1,c)-t(1,c-1));
%     mach(1,c) = vel(1,c)/sqrt(gamma*r_air*T_atm(1,c-1));
%     q(1,c) = rho_atm(1,c-1)*vel(1,c)^2/2;
%     height = h(1,c-1) + vel(1,c-1)*(t(1,c)-t(1,c-1)) +
% acc(1,c)*(t(1,c)-t(1,c-1))^2;
%     if(height>=0)
%         h(1,c) = height;
%     else
%         h(1,c) = 0;
%     end
%     %
%     [T_atm(1,c),P_atm(1,c),rho_atm(1,c)] =
% get_atmospheric_properties(h(1,c));
```

```
%     b(1,c) = C_d*A*rho_atm(1,c)/2;
%     if(vel(1,c)>=0)
%         F_d(1,c) = -b(1,c)*vel(1,c)^2;
%     else
%         F_d(1,c) = b(1,c)*vel(1,c)^2;
%     end

%     c = c + 1;
% end
% I_total = I_int;
% Isp = I_total/(m_prop_0*g_0);

% %% Step 3 - Computation of the trajectory assuming constant
% rocket mass
% % Un cop s'ha esgotat el propel·lent i la pressió a dins la
% cambra s'ha igualat amb la pressió exterior,
% % considerem que el coet és una partícula de massa constant que
% segueix una
% % trajectòria sota la influència de 2 forces: gravitatòria i
% fregament
% % aerodinàmic

% while(h(c-1)>=0)
%     m_total(1,c) = m_dry;
%     t(1,c) = t(1,c-1) + delta_t_trajectory;

%     acc(1,c) = (F_d(1,c-1)+F_g(1,c-1))/m_total(1,c);
%     vel(1,c) = vel(1,c-1) + acc(1,c)*(t(c)-t(c-1));
%     mach(1,c) = vel(1,c)/sqrt(gamma*r_air*T_atm(1,c-1));
%     q(1,c) = rho_atm(1,c-1)*vel(1,c)^2/2;
%     h(1,c) = h(1,c-1) + vel(1,c-1)*(t(1,c)-t(1,c-1)) +
% acc(1,c)*(t(1,c)-t(1,c-1))^2;

%     [T_atm(1,c),P_atm(1,c),rho_atm(1,c)] =
% get_atmospheric_properties(h(1,c));

%     b(1,c) = C_d*A*rho_atm(1,c)/2;
%     if(vel(1,c)>=0)
%         F_d(1,c) = -b(1,c)*vel(1,c)^2;
%     else
%         F_d(1,c) = b(1,c)*vel(1,c)^2;
%     end
%     F_g(1,c) = -m_total(1,c)*g_0;

%     c = c + 1;
% end

% %% Plotting and results presentation
```

```
% figure(1)
% plot(t(1,1:length(P_0)),P_0(1,:)./10^6,'*');
% title("Pressió a dins la cambra de combustió");
% xlabel("Temps d'ençà de la ignició del motor (s)");
% ylabel("Pressió (MPa)");
% %
% figure(2)
% plot(t(1,1:length(F)),F(1,:));
% title("Impuls generat pel motor");
% xlabel("Temps d'ençà de la ignició del motor (s)");
% ylabel("Impuls (N)");
% %
% % figure(3)
% % plot(t(1,1:length(P_2)),P_2(1,:)./10^3);
% % title("Pressió dels gasos de rebuig a la sortida de la
% tobera");
% % xlabel("Temps d'ençà de la ignició del motor (s)");
% % ylabel("Pressió (kPa)");
% %
% % figure(4)
% % plot(t(1,1:length(Vel_2)),Vel_2(1,:));
% % title("Velocitat dels gasos de rebuig a la sortida de la
% tobera");
% % xlabel("Temps d'ençà de la ignició del motor (s)");
% % ylabel("Velocitat (m/s)");
% %
% figure(5)
% plot(t(1,:),h(1,:)./10^3,'-.');
% grid on
% title("Height of the rocket as a function of time");
% xlabel("Time since ignition (s)");
% ylabel("Height above mean sea level (km)");
% %
% % figure(6)
% % plot(t(1,:),vel(1,:));
% % title("Velocitat del coet durant el vol");
% % xlabel("Temps d'ençà de la ignició del motor (s)");
% % ylabel("Velocitat (m/s)");
% %
% % figure(7)
% % plot(t(1,:),mach(1,:));
% % title("Nombre de Mach del coet durant el vol");
% % xlabel("Temps d'ençà de la ignició del motor (s)");
% % ylabel("Nombre de Mach");
```

A.2. Chapter 4: Thermo structural algorithm 1 layer.m

```
% close all
% clear all
% clc
% format long;
% %% Heat transfer algorithm -- Coma Busquets, Aleix

% %% Step 0 - Initial conditions, design & simulation parameters &
% constants are established
% % Constants
% sigma_ct = 5.67*10^(-8); % Constant d'Stefan Boltzmann
% [J/s-m^2-K^4].
% C = 3.025*10^(-3);
% % Simulation parameters
% delta_t = 10^(-5); % En s. Ha de ser múltiple de t_final.
% delta_r = 0.5*10^(-3); % Gruix dels cercles concèntrics [m].
% case_throat = 1; % If 0, case; otherwise, throat.
% if(case_throat==0)
%     A = 1;
% else
%     A = 2;
% end
% % Design parameters
% material_c = 2; % 1: Aluminum 6061-T6; 2: AISI 1018; 4: Graphite
% [E_c,nu_c,rho_c,lambda_c,yield_str_c_0,K_c,C_c,alpha_c,epsilon_c
% ] = get_materials_properties(material_c);
% wall_thick = 5*10^(-3); % Gruix total de la paret [m].
% t_final = 1.5; % Durada total de la simulació [s].
% n = int32(wall_thick/delta_r + 1); % Nombre de nodes al llarg de
% la paret.
% m = int32(t_final/delta_t + 1); % Nombre d'instants de temps al
% llarg de la simulació.
% propellant_id = 3; % 1: KNSB; 2: KNDX; 3: RNX
% [Temp_0,rho,k,M,c_star,C_p] =
% get_propellant_thermodynamic_properties(propellant_id);
% chamber = [484*10^(-3),76*10^(-3)]; % chamber(1): Longitud de la
% cambra, suposant que és un cilindre simple. m
%                                     % chamber(2): Diàmetre
% interior de la cambra. m
% A_c_i = pi/4*chamber(2)^2; % Diàmetre de la secció quadrada
% interior de la cambra [m^2].
% nozzle = [10*10^(-3),75*10^(-3),30,18]; % nozzle(1): Diàmetre de
% la gola. m
%                                         % nozzle(2): Diàmetre
% de la sortida. m
%                                         % nozzle(3): Semi-angle
% de convergència. º
```

```
%                                          % nozzle(4): Semi-angle
% de divergència. º
% sizes = [7,64*10^(-3),74*10^(-3),21*10^(-3),0]; % sizes(1): Nº
% de segments.
%                                          % sizes(2): Longitud
% dels segments. Assumim que són tots iguals. m
%                                          % sizes(3): 1er
% diàmetre: diàmetre exterior dels segments. m
%                                          % sizes(4): 2on
%diàmetre. Si no s'escau, posar '0'. m
%                                          % sizes(5): 3er
% diàmetre. Si no s'escau, posar '0'. m
% m_prop_0 = pi/4*(sizes(3)^2 - sizes(4)^2 +
% sizes(5)^2)*sizes(2)*sizes(1)*rho;
% h = 0; % Alçada sobre el nivell del mar [m]
% [T_e,P_e,rho_e] = get_atmospheric_properties(h);
% P_0 = 2*10^6; % Pressió a la cambra de combustió [K]
% % Design constraints
% safety_factor_c = 1.5;
% structural_integrity = zeros(1,m);
% structural_integrity(1,2) = 1; % 1: La paret aguanta; 0: La
% paret soporta una quantitat d'esforç inacceptable.
% condition = true; % true: condició de disseny es compleix en tot
% moment; false: condició de disseny se supera en algun moment.
% % Initial conditions
% T_int = 293; % Temperatura de la part interna de la paret a
% l'inici.
% T_out = 293; % Temperatura de la part externa de la paret a
% l'inici.
% distribution_type_c = 1; % Distribució de temperatura entre tots
% els nodes de la paret. 1: lineal
% T_c = set_distribution_temperature(distribution_type_c,T_int,T_o
% ut,n,m);
% % Obtenció i organització de dades
% h_g = A*C*(C_p/chamber(2)^0.2)*(m_prop_0/(t_final*pi/4*chamber(2
% )^2))^0.8*(1+(chamber(2)/chamber(1))^0.7); % Coeficient de
% convecció [W/m^2-K]
% T_0 = zeros(1,m);
% T_0(1,1) = T_int;
% T_0(1,2:m) = 1568;
% T_av = zeros(1,m);
% T_av(1,1) = sum(T_c(1,:))/n;
% q_in = zeros(1,m);
% q_in(1,1) = h_g(1,1)*(T_0(1,1) - T_c(1,1)); % Transferència
% inicial d'escalfor de la cambra a la primera capa de la paret
% [J/s-m^2].
% q_out = zeros(1,m);
% q_out(1,1) = sigma_ct*epsilon_c*(T_c(1,n(1))-T_e)^4;
```

```
% Transferència inicial d'escalfor de la cambra a la primera capa
% de la paret [J/s-mˆ2].
% yield_str_c = zeros(1,m);
% yield_str_c(1,1) = yield_str_c_0;
% sigma_theta_c = zeros(1,m);
% sigma_theta_c(1,1) = 0;
% sigma_l_c = zeros(1,m);
% sigma_l_c(1,1) = 0;
% sigma_t_c = zeros(1,m);
% sigma_t_c(1,1) = 0;
% sigma_eq_c = zeros(1,m);
% sigma_eq_c(1,1) = 0;
% sigma_fraction = zeros(1,m);
% sigma_fraction(1,1) = 0;
% %% Step 1.1 - Compute the convective heat transfer to the walls
% and the radiative heat transfer out of the walls at the second
% time step

% c = 2;
% [Temp_0,rho,k,M,c_star,C_p] =
% get_propellant_thermodynamic_properties(propellant_id);
% q_in(1,c) = h_g*(T_0(1,c)-T_c(c-1,1)); % Transferència
% d'escalfor convectiva al segon pas de simulació.
% q_out(1,c) = sigma_ct*epsilon_c*(T_c(c-1,n)-T_e)ˆ4;

% %% Step 1.2 - Compute the temperature distribution on the walls
% on the second time step

% T_c(c,1) = T_c(c-1,1) + q_in(1,c)/(rho_c*C_c)*(delta_t/delta_r)
% + alpha_c*(delta_t/delta_rˆ2)*(T_c(c-1,2)-T_c(c-1,1));
% for(k=2:1:(n-1)) % 'k' és el node actual a la paret.
%     T_c(c,k) = T_c(c-1,k) +
% alpha_c*(delta_t/delta_rˆ2)*(T_c(c-1,k+1)-2*T_c(c-1,k)+T_c(c-1,k
%-1));
% end
% T_c(c,n) = T_c(c-1,n) +
% alpha_c*(delta_t/delta_rˆ2)*(T_c(c-1,n-1)-T_c(c-1,n)) -
% q_out(1,c)/(C_c*rho_c);

% %% Step 1.3 - Compute the arithmetical mean of the wall
% temperature on the second time step

% T_av(1,c) = sum(T_c(c,:))/n;

% %% Step 1.4 - Derive the yield strength value of the case
% % if(material_c==1 || material_c==2)
% %     sigma_yield_c =
% get_yield_strength(T_av(1,c),material_c,m);
```

```
% % else
% %     sigma_yield_c = 276*10^6;
% % end
% yield_str_c(1,c) = get_yield_strength(T_av(1,c),material_c,m);
% %% Step 1.5 - Compute the equivalent stress acting on the walls
% on the second time step

% sigma_theta_c(1,c) = P_0*chamber(2)/(2*wall_thick); % Esforç
% circumferencial/tangencial/'hoop' [Pa] actuant sobre el 'case'.
% Considerem pressió externa negligible.
% sigma_l_c(1,c) = P_0*chamber(2)/(4*wall_thick); % Esforç
% longitudinal [Pa] actuant sobre el 'case'.
% sigma_t_c(1,c) = 2*lambda_c*E_c*(T_c(c,n)-T_c(c,1))/(1-nu_c);
% Esforç tèrmic [Pa] actuant sobre el 'case'.

% sigma_eq_c(1,c) = abs(sigma_theta_c(1,c)) + abs(sigma_l_c(1,c))
% + abs(sigma_t_c(1,c));
% %% Step 1.6 - Assess whether or not the resultant stress does
% breach the design constraints
% % Our sole design constraint is the safety factor.
% sigma_fraction(1,c) = yield_str_c(1,c)/sigma_eq_c(1,c);
% if(sigma_eq_c(1,c)>=yield_str_c(1,c)/safety_factor_c)
%     structural_integrity(1,c) = 0;
%     condition = false;
% else
%     structural_integrity(1,c) = 1;
% end

% %% Step 2 - Repeat steps 1.1 to 1.6 until the simulation ends
% %
% c = 3;
% while(c<=m)
%     q_in(1,c) = h_g*(T_0(1,c)-T_c(c-1,1)); % Transferència
% d'escalfor convectiva al segon pas de simulació.
%     q_out(1,c) = sigma_ct*epsilon_c*T_c(c-1,n)^4;
%     %
%     T_c(c,1) = T_c(c-1,1) +
% q_in(1,c)/(rho_c*C_c)*(delta_t/delta_r) +
% alpha_c*(delta_t/delta_r^2)*(T_c(c-1,2)-T_c(c-1,1));
%     for(k=2:1:(n-1)) % 'k' és el node actual a la paret.
%         T_c(c,k) = T_c(c-1,k) +
% alpha_c*(delta_t/delta_r^2)*(T_c(c-1,k+1)-2*T_c(c-1,k)+T_c(c-1,k
% -1));
%     end
%     T_c(c,n) = T_c(c-1,n) +
% alpha_c*(delta_t/delta_r^2)*(T_c(c-1,n-1)-T_c(c-1,n)) -
% q_out(1,c)/(C_c*rho_c);
%     %
```

```
%     T_av(1,c) = sum(T_c(c,:))/n;
%     %
% %     if(material_c==1 || material_c==2)
% %         sigma_yield_c =
% get_yield_strength(T_av(1,c),material_c,m);
% %     else
% %         sigma_yield_c = 276*10^6;
% %     end
%     yield_str_c(1,c) =
% get_yield_strength(T_av(1,c),material_c,m);
%     %
%     sigma_theta_c(1,c) = P_0*chamber(2)/(2*wall_thick); % Esforç
% circumferencial/tangencial/'hoop' [Pa] actuant sobre el 'case'.
% Considerem pressió externa negligible.
%     sigma_l_c(1,c) = P_0*chamber(2)/(4*wall_thick); % Esforç
% longitudinal [Pa] actuant sobre el 'case'.
%     sigma_t_c(1,c) =
% 2*lambda_c*E_c*(T_c(c,n)-T_c(c,1))/(1-nu_c); % Esforç tèrmic
% [Pa] actuant sobre el 'case'.
%     sigma_eq_c(1,c) = abs(sigma_theta_c(1,c)) +
% abs(sigma_l_c(1,c)) + abs(sigma_t_c(1,c));
%     %
%     sigma_fraction(1,c) = yield_str_c(1,c)/sigma_eq_c(1,c);
%     if(sigma_eq_c(1,c)>=yield_str_c(1,c)/safety_factor_c)
%         structural_integrity(1,c) = 0;
%         condition = false;
%     else
%         structural_integrity(1,c) = 1;
%     end

%     c = c + 1;
% end

% if(condition==false)
%     disp('Design constraint has been breached sometime during
% the simulation.');
% else
%     disp('Design constraint has been met with the current
% design!');
% end

% % plot_delta_t = 1; % En s. Separació temporal entre línies
% successives.
% % plot_delta_matrix = plot_delta_t/delta_t;
% % X = 0:1:(n-1);
% %
% % Y = T_c(1,:);
% % figure(1)
```

```
% % plot(X,Y,':.k');
% % title('Time-varying T distribution');
% % xlabel('Concentric layers of the case');
% % ylabel('T(K)');
% % hold on
% % for(c = int32(plot_delta_matrix+1):int32(plot_delta_matrix):m)
% %     Y = T_c(c,:);
% %     plot(X,Y,':.k');
% % end
% % hold off

% disp(min(sigma_fraction(1,2:m)))
```

APPENDIX B. TECHNICAL DRAWINGS

B.1. Chapter 5: Experiment assembly

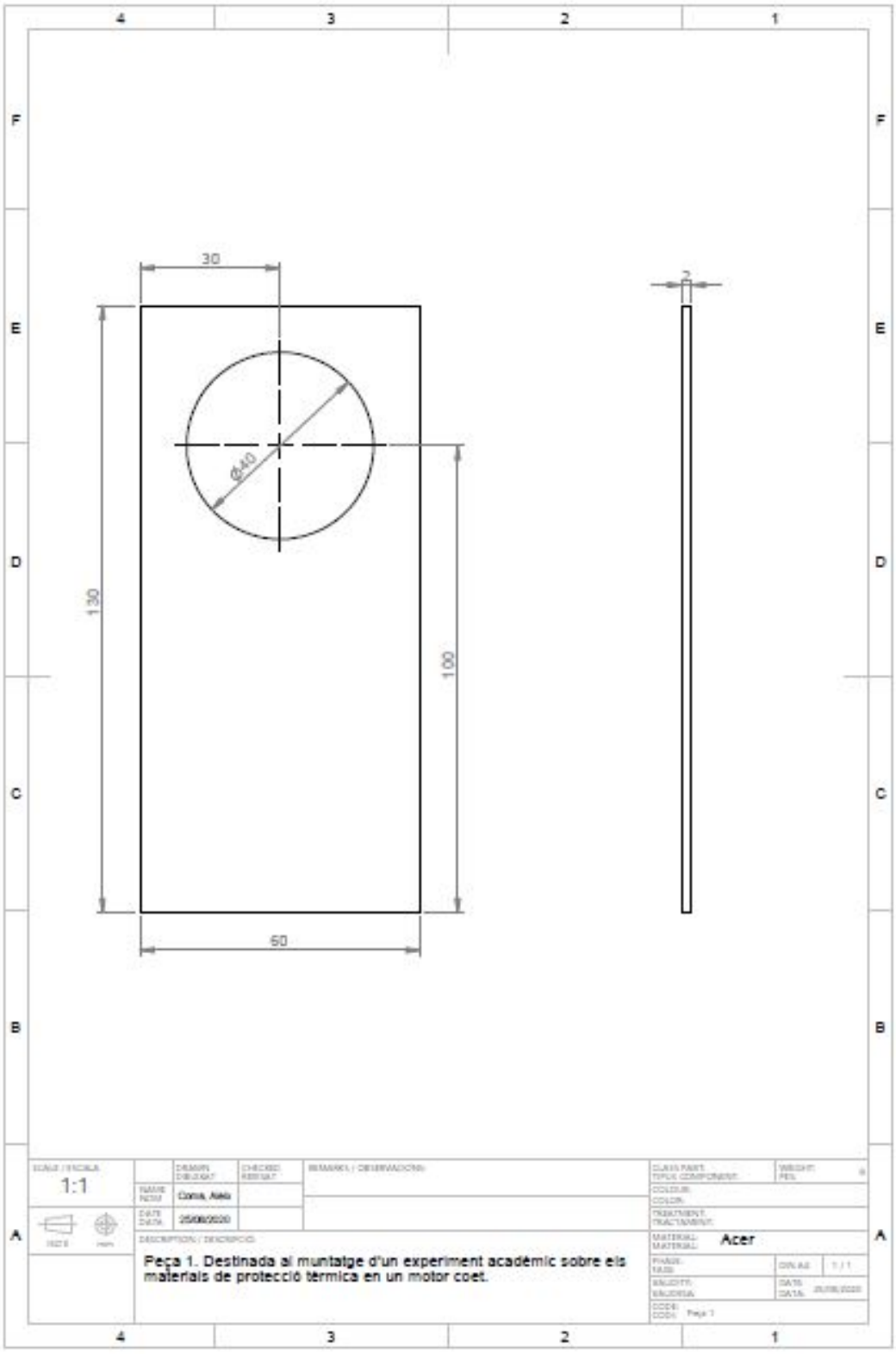

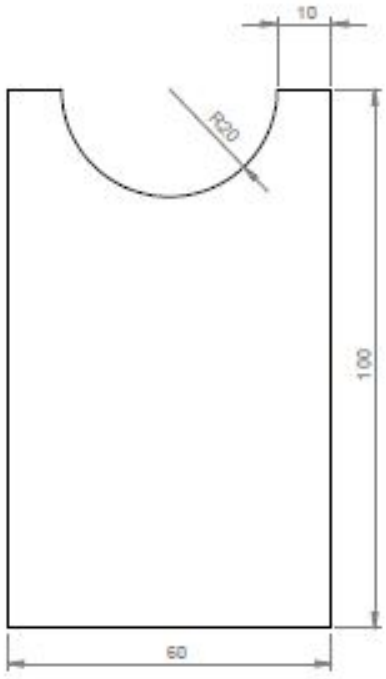

ESCALA / ESCALA: 1:1	DIBUIXAT / DRAWN:	COMPROVAT / CHECKED:	REMARKS / OBSERVACIONS:	CLASSE PART / TIPUS COMPONENT:	WEIGHT / PES: g
	NOM / NAME: Coma, Aleix			COLOUR:	
	DATA / DATE: 25/09/2020			TRACTAMENT / TRATAMIENT:	
	DESCRIPCIÓ / DESCRIPCIÓ: Peça 2. Destinada al muntatge d'un experiment acadèmic sobre els materials de protecció tèrmica en un motor coet.			MATERIAL / MATERIAL: Acer	
				FASE / FASE:	DIN A4 1 / 1
				SOL·LICITUD / SOLICITUD:	DATE / DATA: 25/09/2020
				CODI / CODE: Peça 2	

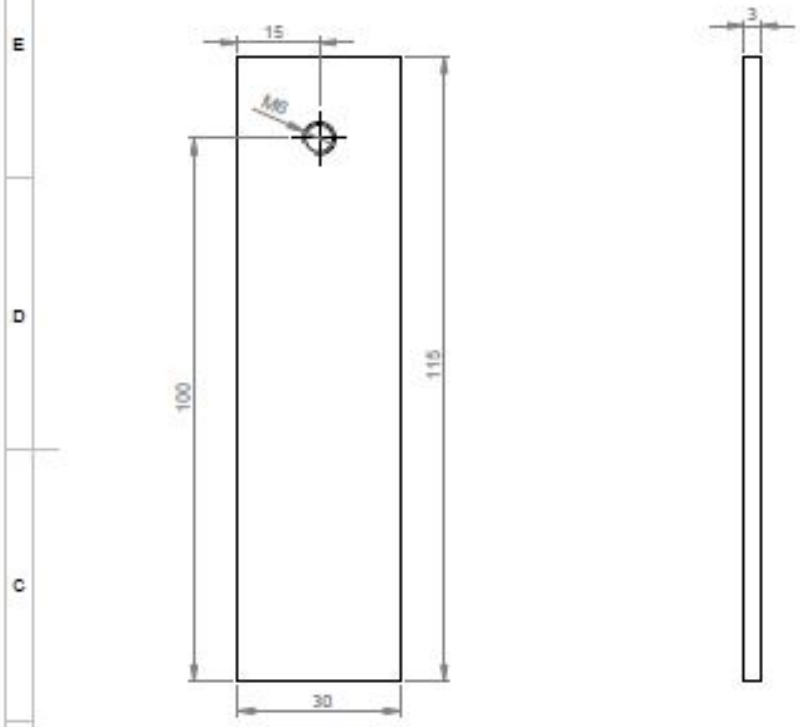

ESCALA / ESCALA: 1:1		DIBUIXAT	CHECKED	REMARKS / OBSERVACIONS:	CLASS PART. TIPUS COMPONENT:	WEIGHT: PES:
	NAME NOM:	Coma, Alex			COLOUR: COLOR:	
ISO 8	DATE DATA:	05/06/2020			TREATMENT: TRACTAMENT:	
	DESCRIPTION / DESCRIPCIÓ:				MATERIAL: MATERIAL:	Ferro
	Peça 3. Destinada al muntatge d'un experiment acadèmic sobre els materials de protecció tèrmica en un motor coet.				FINISH: MIDA:	DIN A3 1 / 1
					BAIXOTTI: BAIXOTSA:	DATE: DATA: 05/06/2020
					CODE: CODI: Peça 3	

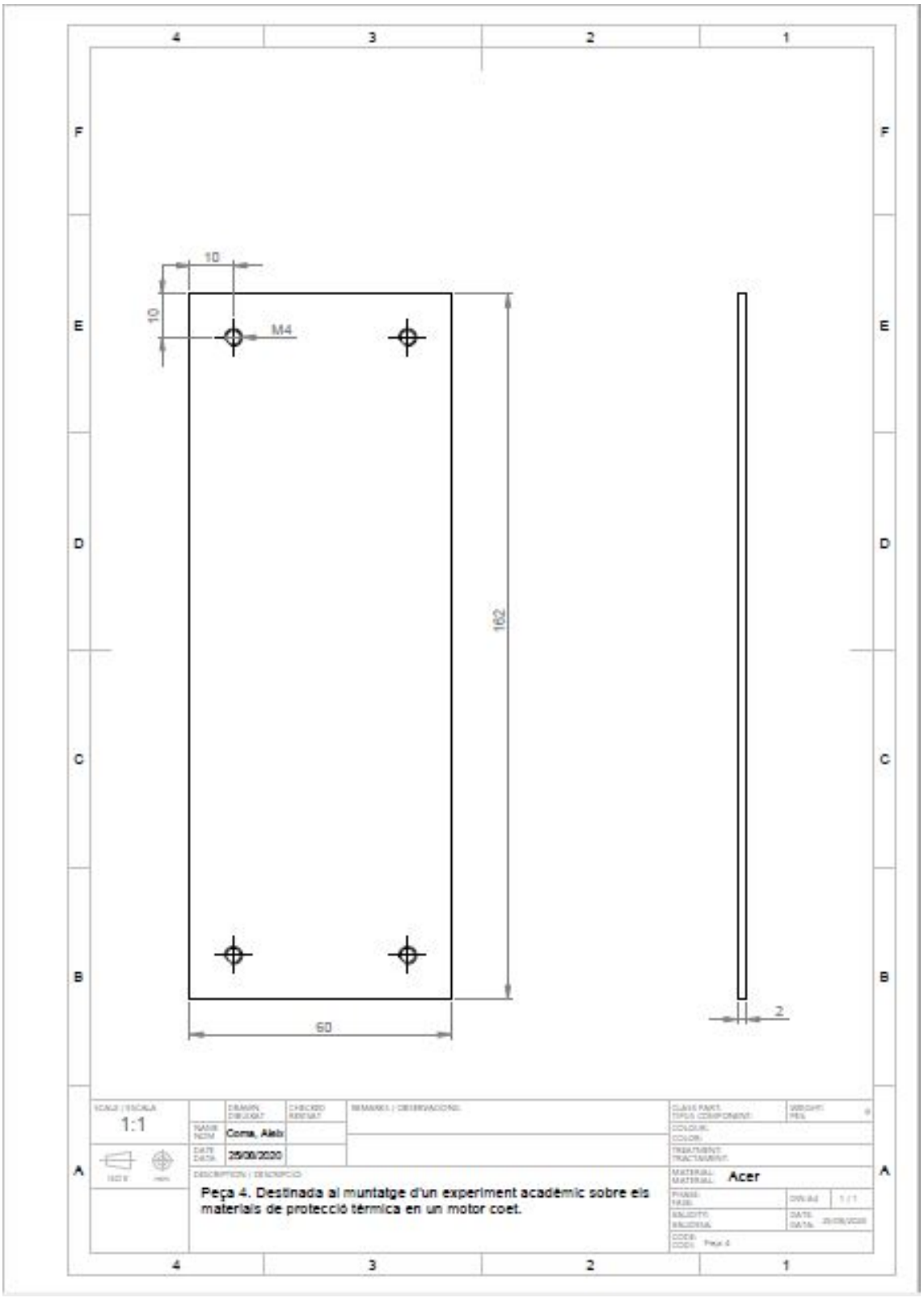

ESCALA / ESCALA: 1:1		DIBUIXAT:	COMPROVAT:	REMARQUES / OBSERVACIONS:	CLASSE PART: TIPUS COMPONENT:	MIDES/PES:
	NOM:	Coma, Aleix			COLOR:	
	DATA:	25/06/2020			TRACTAMENT:	
	DESCRIPCIÓ / DESCRIPCIÓ:				MATERIAL:	Acer
	Peça 4. Destinada al muntatge d'un experiment acadèmic sobre els materials de protecció tèrmica en un motor coet.				FASE:	DIN A4 1:1
					SOL·LICITUD:	DATA: 25/06/2020
					CODI:	Peça 4

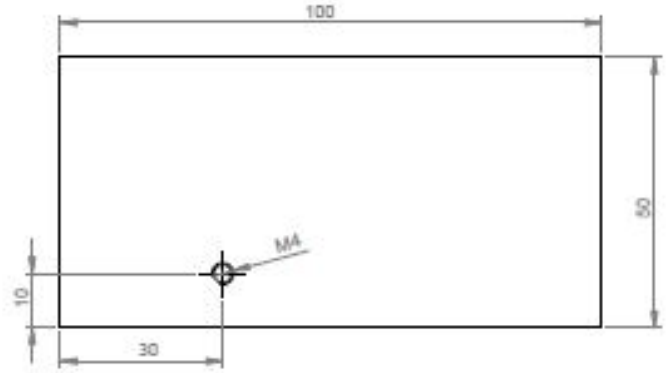

ESCALA / ESCALA: 1:1		DIBUIXAT:	COMENTARIS / OBSERVACIONS:	CLASSE PART:	PES:
ISO E		NOM: Coma, Aleix		COLOR:	
		DATA: 25/09/2020		TRACTAMENT:	
		DESCRIPCIÓ / DESCRIPCIO:		MATERIAL: Acer	
		Peça 5. Destinada al muntatge d'un experiment acadèmic sobre els materials de protecció tèrmica en un motor coet.		FASE:	DIN A4 1:1
				VALIDESA:	DATA: 25/09/2020
				CODI: Peça 5	

B.2. Chapter 6: Mechanical prototype

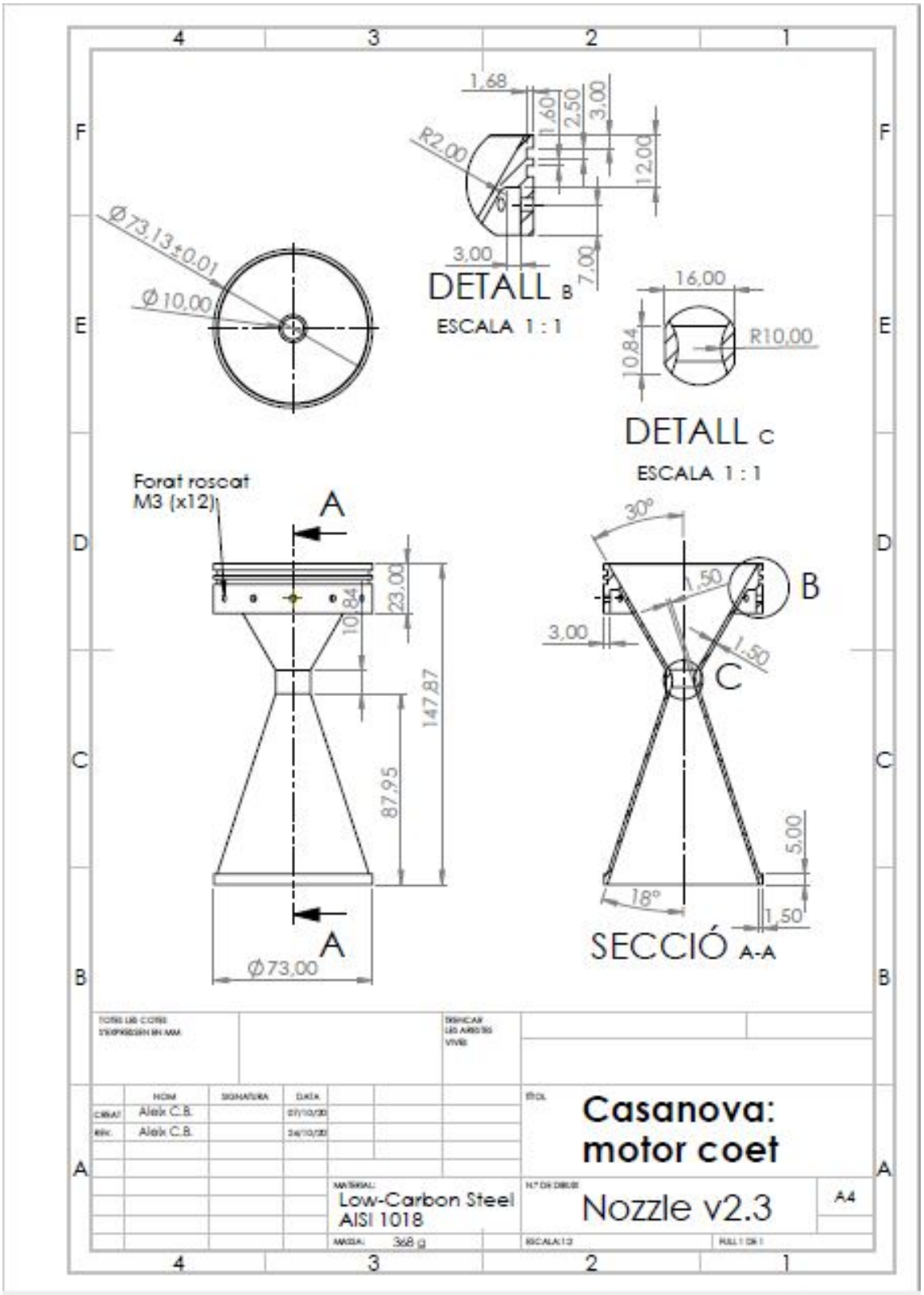

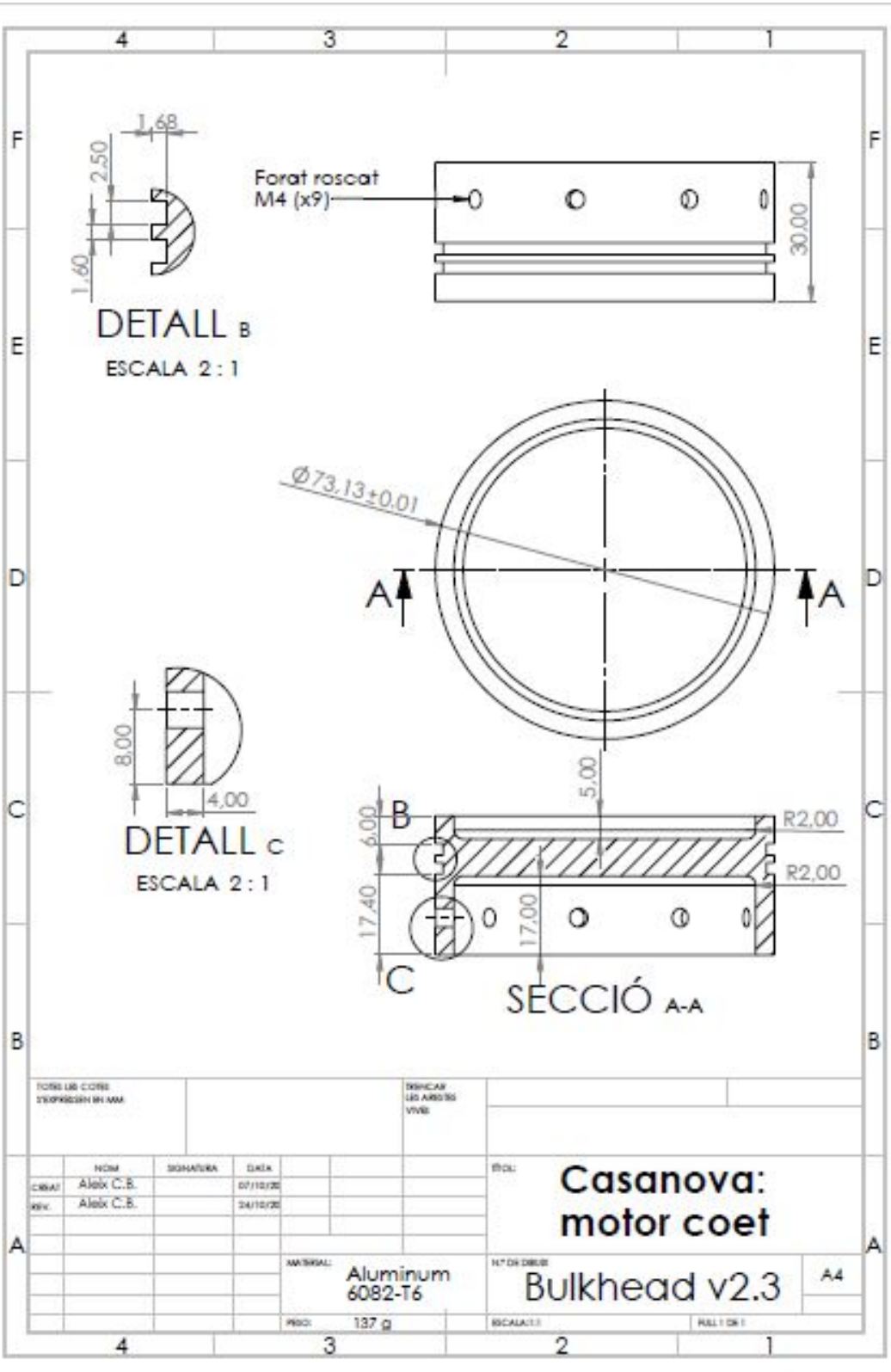
1,68
2,50
1,60
DETALL B
ESCALA 2 : 1
Forat roscat
M4 (x9)
30,00
Ø73,13±0,01
A
A
8,00
4,00
DETALL C
ESCALA 2 : 1
5,00
B
6,00
17,40
C
17,00
R2,00
R2,00
SECCIÓ A-A
Casanova:
motor coet
Aluminum
6082-T6
Bulkhead v2.3
A4
137 g

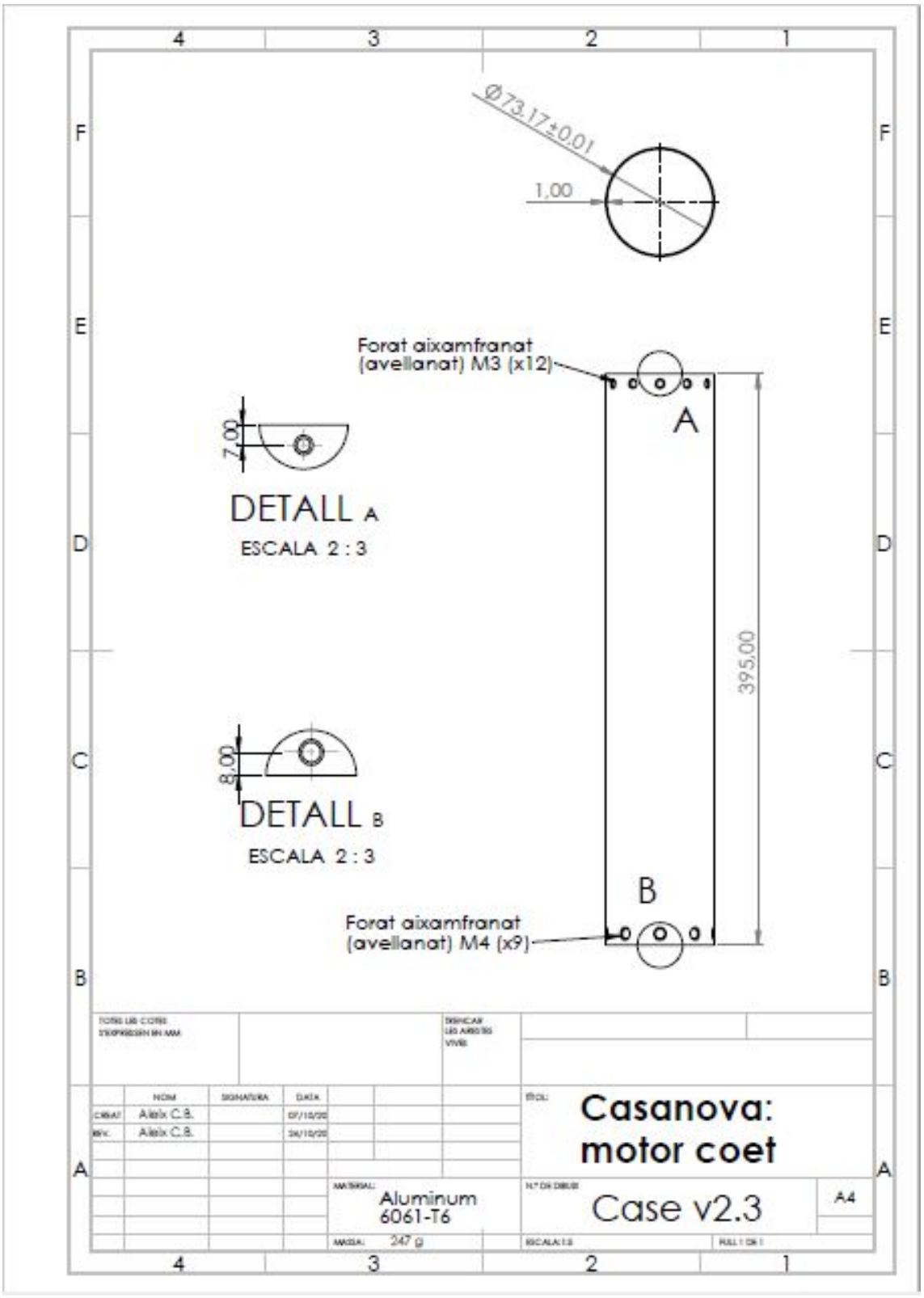
Ø73,17±0,01
1,00
Forat aixamfranat
(avellanat) M3 (x12)
A
7,00
DETALL A
ESCALA 2 : 3
395,00
8,00
DETALL B
ESCALA 2 : 3
B
Forat aixamfranat
(avellanat) M4 (x9)
Casanova:
motor coet
Aluminum
6061-T6
Case v2.3
A4
247 g

APPENDIX C. MANUAL OF THE EXPERIMENT, PLOTS AND IMAGES

Manual de l'experiment (13/10)

Passos previs

1. Completar el muntatge.
2. Comprovar que la posició i orientació de la torxa i el muntatge són correctes. Sinó, ajustar mitjançant les fulloles i els cargols de suport.
3. Decidir el mètode de fixació del termoparell al revers de les plaques. Provar-lo.
4. Decidir freqüència del datalogger; 10 Hz sembla una bona opció.
5. Fer prova de temperatura de flama per a provar el funcionament del termoparell i de la torxa. Els resultats han de ser similars als de la darrera vegada.
6. Decidir quin aparell farem servir com a cronòmetre i comprovar que funciona.
7. Col·locar correctament la torxa i el muntatge a la zona de proves.
8. Col·locar el termoparell al revers de la placa. Fixar la placa al lloc amb la mordassa. Col·locar l'escut.
9. Fer una "simulació" a temps real però sense flama del que caldrà fer a continuació, per decidir quantes persones i qui haurà de fer cada pas.
10. Analitzar quins són els perills de les proves (flama i altes temperatures dels materials), i com hem d'anar protegits i actuar per a minimitzar-los. Decidir quan temps ens hem d'esperar entre la successió de 2 proves. Decidir si fem 1 "simulació" amb foc però sense enregistrar dades.

Experiment

1. Col·locar placa i escut, muntatge i torxa al lloc.
2. Engegar el datalogger.
3. Engegar la torxa.
4. Retirar l'escut i, al'instant, posar en marxa el cronòmetre.
5. Esperar 10 segons.
6. Tornar a col·locar l'escut i, al'instant, apagar la flama. Apagar el cronòmetre.
7. Esperar un cert temps, per tal que la temperatura dels materials es redueixi.
8. Retirar la placa i l'escut. Guardar la placa.
9. Assegurar-se que tot ha funcionat: temps, flama, datalogger ha enregistrat les dades, etc.
10. Col·locar la següent placa i l'escut, i dur a terme tots els passos anteriors, de l'1 al 9, de nou.
11. Fer almenys una prova amb la càmera termogràfica. Cal decidir com es fa.

Posterior

1. Assegurar-se que disposem de totes les dades. Introduir targeta del datalogger a l'ordinador per visualitzar-les.
2. Fer un anàlisi preliminar de dades: si són "racionals" i similars a les esperades.
3. Recollir totes les plaques que s'han fet servir, el muntatge i tot el material.

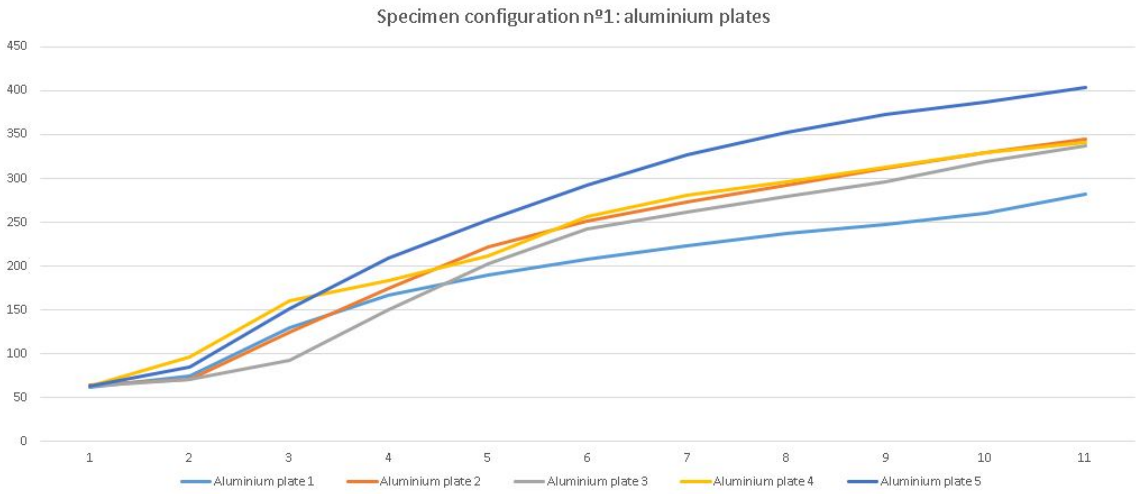

Figure C.1: Results for the testing of the five specimens of configuration n^{o}1. In the vertical axis, temperature at the rear of the plate in °C. In the horizontal axis, the n^o of data point, separated one second from each other.

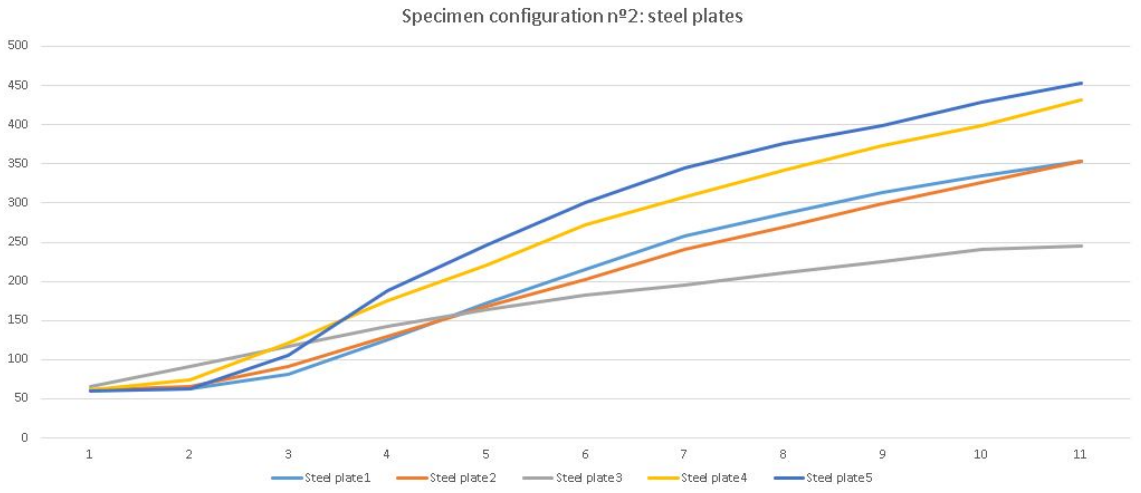

Figure C.2: Results for the testing of the five specimens of configuration n^{o}2.

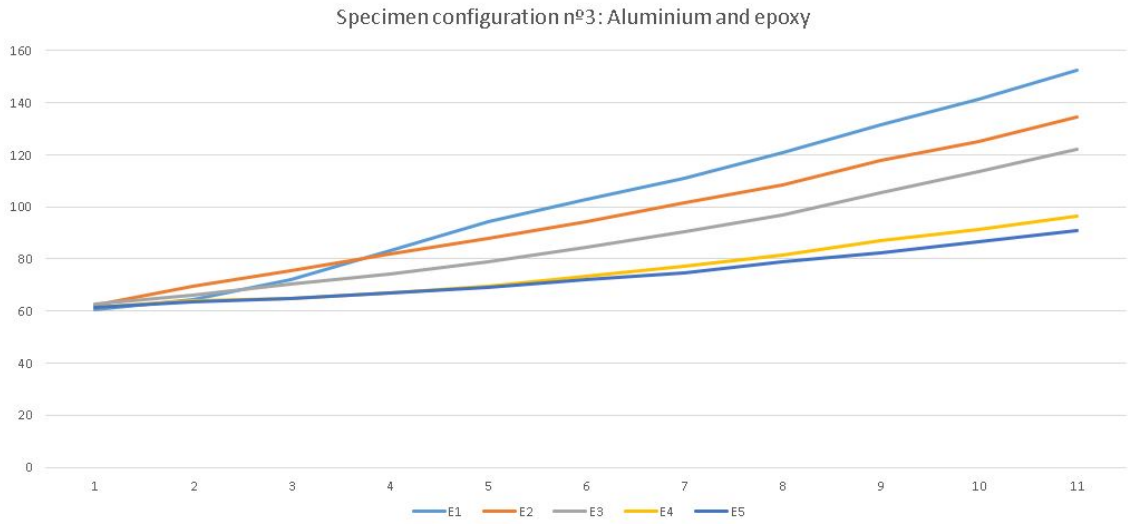

Figure C.3: Results for the testing of the five specimens of configuration n^{o}3.

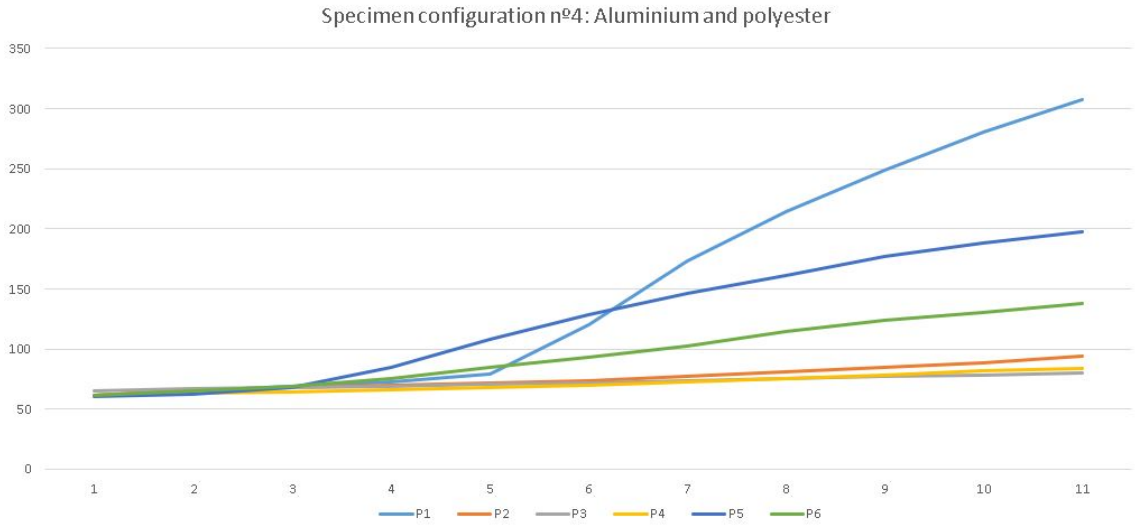

Figure C.4: Results for the testing of the five specimens of configuration n^{o}4.

Figure C.5: Preparation of the specimens.

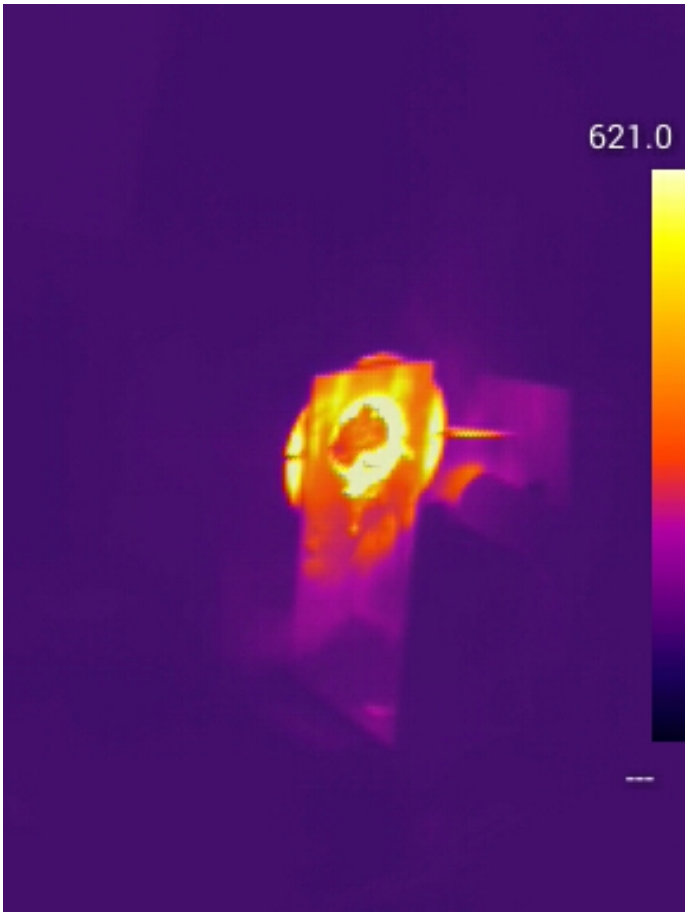

Figure C.6: Highest temperature registered by the thermographic camera, with the last specimen of configuration 4.

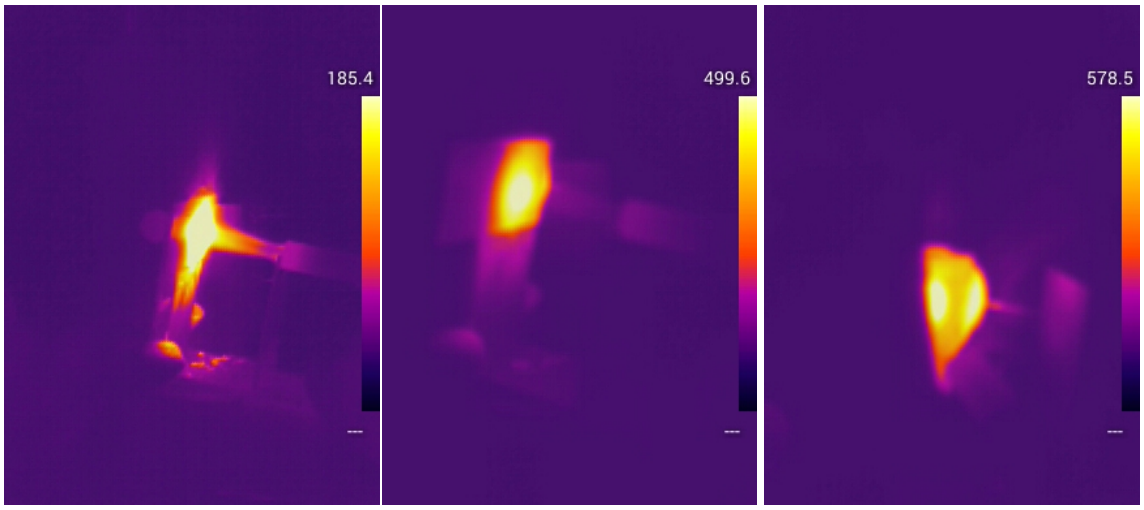

Figure C.7: Succession of three images of the thermographic camera for the same specimen, showing the rise in temperature.